Journal of Investigative Dermatology

The Role of Fibroblast Growth Factor Binding Protein 1 in Skin Carcinogenesis and Inflammation

Journal:	*Journal of Investigative Dermatology*
Manuscript ID	JID-2016-1055.R1
Article Type:	Original Article
Date Submitted by the Author:	04-Jun-2017
Complete List of Authors:	Schmidt, Marcel; Georgetown University, Lombardi Comprehensive Cancer Center Garman, Khalid; Georgetown University, Lombardi Comprehensive Cancer Center Lee, Yong; Georgetown University, Lombardi Comprehensive Cancer Center; Purdue University System, Department of Chemistry Zuo, Chong; Georgetown University, Lombardi Comprehensive Cancer Center; Washington University in Saint Louis School of Medicine, Department of Medicine Beck, Patrick; Georgetown University, Lombardi Comprehensive Cancer Center; Thomas Jefferson High School for Science and Technology, Chemistry Tan, Mingjun; Georgetown University, Lombardi Comprehensive Cancer Center Aguilar_Pimentel, Juan; German Research Center for Environmental Health GmbH, German Mouse Clinic, Institute of Experimental Genetics, Helmholtz Zentrum München Ollert, Markus; Luxembourg Institute of Health, Department of Infection and Immunity; University of Southern Denmark, Odense, Denmark, Department of Dermatology and Allergy Center, Odense Research Center for Anaphylaxis, Odense University Hospital Schmidt-Weber, Carsten; Technische Universität & Helmholtz Center Munich, ZAUM Center for Allergy and Environment Gailus-Durner, Valerie; German Research Center for Environmental Health GmbH, German Mouse Clinic, Institute of Experimental Genetics, Helmholtz Zentrum München Fuchs, Helmut; German Research Center for Environmental Health GmbH, German Mouse Clinic, Institute of Experimental Genetics, Helmholtz Zentrum München Hrabe de Angelis, Martin; German Research Center for Environmental Health GmbH, German Mouse Clinic, Institute of Experimental Genetics, Helmholtz Zentrum München; Technische Universität München, Experimental Genetics, Center of Life and Food Sciences Weihenstephan; German Center for Diabetes Research , (DZD) Tassi, Elena; Georgetown University, Lombardi Comprehensive Cancer Center Riegel, Anna; Georgetown University, Lombardi Comprehensive Cancer Center

	Wellstein, Anton; Georgetown University, Lombardi Comprehensive Cancer Center
Keywords:	Carcinogenesis, Wound healing, FGF, Angiogenesis, Inflammation

The Role of Fibroblast Growth Factor Binding Protein 1 in Skin Carcinogenesis and Inflammation

Marcel Oliver Schmidt[1*], Khalid Ammar Garman[1], Yong Gu Lee[1,2], Chong Zuo[1,3], Patrick James Beck[1,4], Mingjun Tan[1], Juan Antonio Aguilar-Pimentel[5], Markus Ollert[6], Carsten Schmidt-Weber[7], Helmut Fuchs[5], Valerie Gailus-Durner[5], Martin Hrabe de Angelis[5,8,9], German Mouse Clinic Consortium[§], Elena Tassi[1], Anna Tate Riegel[1], Anton Wellstein[1*]

[1]Lombardi Comprehensive Cancer Center, Georgetown University, Washington, DC 20057, USA,

[2]Purdue University System, Department of Chemistry
West Lafayette, IN, USA

[3]Washington University in Saint Louis School of Medicine, Department of Medicine
Saint Louis, MO, USA

[4]Thomas Jefferson High School for Science and Technology, Chemistry
Alexandria, VA, USA
703-750-8300

[5]German Mouse Clinic, Institute of Experimental Genetics, Helmholtz Zentrum München, German Research Center for Environmental Health, Ingolstädter Landstraße 1, 85764 Neuherberg, Germany

[6]Department of Infection and Immunity, Luxembourg Institute of Health, Esch-sur-Alzette, Luxembourg, and Department of Dermatology and Allergy Center, Odense Research Center for Anaphylaxis, University of Southern Denmark, Odense, Denmark

[7]Center of Allergy & Environment (ZAUM), Technische Universität München (TUM) and Helmholtz Zentrum, Biedersteiner Str. 29, 80802 Munich, Germany, and Member of the German Center for Lung Research (DZL), Aulweg 130, 35392 Gießen, Germany

[8]Chair of Experimental Genetics, Center of Life and Food Sciences Weihenstephan, Technische Universität München, Germany

[9]German Center for Diabetes Research (DZD), Ingolstädter Landstraße 1, 85764 Neuherberg, Germany

[§] A full list of consortium members appears at the end of the paper.

The work for this manuscript was done in Washington, DC, USA and Munich, Bavaria, Germany

***correspondence to**

Marcel O. Schmidt; e-mail: mos6@georgetown.edu, Phone: +1 (202) 687-4771, fax; +1 (202) 687-4821, Lombardi Comprehensive Cancer Center, Georgetown University, Washington, DC 20057, USA,

or

Anton Wellstein; e-mail: anton.wellstein@georgetown.edu, Phone: +1 (202) 687-3672, fax; +1 (202) 687-4821, Lombardi Comprehensive Cancer Center, Georgetown University, Washington, DC 20057, USA,

Short title: FGFBP1 in Carcinogenesis and Inflammation

Keywords: Carcinogenesis, Wound healing, FGF, Angiogenesis, Inflammation

Abbreviations: DMBA, 7,12-dimethylbenz[a]anthracene; FGFBP, Fibroblast Growth Factor Binding Protein; KO, knockout; qRT-PCR, quantitative real-time PCR; TEWL, Transepidermal water loss; TPA, 12-O-tetradecanoyl-phorbol-13- acetate; WT, wildtype

Abstract

Fibroblast growth factor-binding protein 1 (FGFBP1, FGF-BP) is a secreted chaperone that mobilizes paracrine-acting FGFs, stored in the extracellular matrix, and presents them to their cognate receptors. FGFBP1 enhances FGF signaling including angiogenesis during cancer progression, and is upregulated in various cancers. Here we evaluated the contribution of endogenous FGFBP1 to development and homeostasis as well as to skin pathologies utilizing Fgfbp1-knockout (KO) mice. Relative to wild-type (WT) littermates KO mice showed no gross pathologies. Still, in KO mice a significant thickening of the epidermis associated with a decreased transepidermal water loss and increased pro-inflammatory gene expression in the skin was detected. Also, skin carcinogen challenge by DMBA/TPA resulted in delayed and reduced papillomatosis in KO mice. This was paralleled by delayed healing of skin wounds and reduced angiogenic sprouting in subcutaneous matrigel plugs. Heterozygous GFP-knock-in mice revealed rapid induction of gene expression during papilloma induction and during wound healing. Examination of WT skin grafted onto Fgfbp1 GFP knockin reporter hosts and bone marrow transplants from the GFP reporter model into WT hosts revealed that circulating Fgfbp1-expressing cells migrate into healing wounds. We conclude that tissue-resident and circulating Fgfbp1-expressing cells modulate skin carcinogenesis and inflammation.

Introduction

The fibroblast growth factor binding protein (FGFBP) family consists of three human and two murine (FGFBP1, 3) members, which are secreted chaperone proteins that bind to FGFs and enhance their biological activity (Tassi and Wellstein 2006). As the best characterized member, FGFBP1 has been shown to bind to FGF1, 2, 7, 10 and 22 in a reversible manner through its C-terminal domain (Tassi et al. 2011). Paracrine FGFs (e. g. FGF1 and FGF2) are immobilized in the extracellular matrix and are released to bind to their cognate FGF receptors. In this context FGFBP1 works as a modulator that chaperones the FGFs from their location in the extracellular matrix to target cells expressing FGF receptors.

FGFBP1 is expressed in epithelial cells in skin, stomach, eye, ileum and colon (Aigner et al. 2002; Kurtz et al. 1997), was found to act as an angiogenic switch molecule in cancer (Czubayko et al. 1997) and expressed in squamous cell carcinoma (Czubayko et al. 1994), pancreatic and colon cancer (Henke et al. 2006). Also, FGFBP1 is upregulated during a two-step chemical skin carcinogenesis challenge with DMBA and TPA (Kurtz et al. 2004). We have previously investigated the role of FGFBP1 in a transgenic mouse model and found that conditionally expressed FGFBP1 accelerated angiogenesis in subcutaneously implanted matrigel plugs, enhanced wound healing and reduced ischemic hindlimb injury. Furthermore, FGFBP1 and FGFBP2 play a critical role during chicken development: knockdown of either of them caused embryonic lethality in part through vascular leakage. (Gibby et al. 2009).

To investigate the function of endogenous FGFBP1 we generated a knockout and a knock-in GFP-reporter mouse model, to investigate the role of FGFBP1 in development, skin homeostasis and repair and during challenge by chemical carcinogenesis.

Results

Generation of Fgfbp1-knockout mice

The complete Fgfbp1 open-reading-frame contained in exon 2 on chromosome 5 was replaced by a floxed Fgfbp1 gene and a neo-GFP cassette, resulting in $Fgfbp1^{+/loxP\text{-}neo\text{-}gfp}$ mice, which were then crossed with mice expressing cre (**Fig. 1a**). The resulting mouse line expressed GFP in lieu of Fgfbp1 ($Fgfbp1^{+/gfp}$) and served to monitor activity of the Fgfbp1 promoter. To generate Fgfbp1-knockout mice (KO) the $Fgfbp1^{loxP\text{-}neo\text{-}gfp}$ mice were crossed with mice expressing the recombinase Flpase and then with cre-expressing mice (**Fig. 1b-f**). The mouse strain in this study is primarily C57Bl/6N and to a lower degree SV129N.

The epidermis of KO mice is thicker and has a reduced permeability

Since endogenous FGFBP1 is predominantly expressed in skin (Aigner et al. 2002), we initially focused on the analysis of the skin phenotype in the KO animals. The epidermis of adult (2-3 months old) but not juvenile KO mice (3 weeks old) showed a twofold increased thickness ($p<0.05$; **Fig. 2a, S1a)**. In contrast, the thickness of dermis, fat and panniculus muscle were not significantly different between WT and KO **(Fig. 2b)**. The increased thickness in KO mice coincided with an increased proliferation index in basal keratinocytes (**Fig 2c, e**). Also, ~50% of the epidermis in KO mice showed multilayered

keratinocyte strata in contrast with mostly single layers in WT (**Fig. 2d**). Commensurate with epidermal thickening in KO mice transepidermal water loss (TEWL) was decreased **(Fig. 2f)**. Also, global expression analysis of skin RNA, indicates significantly altered pathways related to barrier function in KO versus WT mice (**Fig. S2a**) although staining for Claudin1 and Filaggrin showed no differences in the epidermis between WT and KO (**Fig. 2e**). Analysis of RNA from the epidermis and from the dermis showed a higher expression of the macrophage marker F4/80 and Ffgr1c in the epidermis of KO mice (**Fig. 2g**). In KO mice both Fgfr1b and c are expressed at similar levels in the dermis and epidermis, whilst a 10-fold higher expression of the c-isoform was seen in the dermis vs the epidermis of WT animals (**Fig. 2g**). Fgf7 and Fgfr2 were not differentially expressed in the epidermis or dermis (**Fig. S1b**).

FGFBP1 upregulation in patients' psoriatic lesions and squamous cell skin cancer (SCC)

Epidermal thickening observed in the Fgfbp1-KO model has been described in inflammatory pathologies of the skin such as psoriasis (Stern 1997) and FGFR2 and FGF7 were found elevated in psoriatic skin (Guban et al. 2016). To assess FGFBP1 gene expression we analyzed two previously published gene expression studies (Nair et al. 2009; Reischl et al. 2007) of paired samples of normal skin, psoriatic skin without and with lesions. FGFBP1 is significantly upregulated in lesions but not in unaffected skin (**Fig. S3a, b**). Analysis of another study (Nindl et al. 2006) revealed that FGFBP1 is upregulated in actinic keratosis (AK) and invasive SCC relative to normal skin (**Fig. S3c**).

Skin epidermis of KO mice shows elevated pro-inflammatory gene expression

A psoriatic phenotype can be mimicked in mice by topical application of Aldara, a pro-inflammatory agent (Walter et al. 2013) **Fig. 3a)**. Aldara contains Imiquimod and activates the innate immune system via TLR-7 on neutrophils, macrophages and dendritic cells and indirectly induces proliferation of keratinocytes (van der Fits et al. 2009). As a readout for activation by Aldara, we monitored Myeloperoxidase (MPO) activity, which increased during Aldara treatment in both WT and KO skin **(Fig. 3b**). In response to Aldara, the expression of Fgfbp1 increased in WT mice (2.5-fold; **Fig. 3c)** as did GFP activity in heterozygous GFP-reporter mice ($Fgfbp1^{+/gfp}$; 6-fold; **Fig. 3d, e**). Aldara treatment also induced a striking, 4.5-fold epidermal thickening **(Fig. 3f, g)** and expression of the inflammatory genes Il6 and Il17a as well as the epithelial marker Krt16 **(Fig. 3h, S5)**. The expression of these genes was significantly elevated at baseline in the skin of KO mice, indicating a skin phenotype with activated immune response and thus increased epithelial proliferation **(Fig. 2b, d, 3f, g)**. It has been shown that the skin barrier function is highly dependent on FGF receptor expression (Yang et al. 2010). Fgfr2, 3, 4 expression and phosphorylation of Fgfr1 and 3, however, were not altered significantly (**Fig. S4**, **S5**). These data suggest that the loss of Fgfbp1 induces a baseline increase in pro-inflammatory gene expression in KO skin comparable to the Aldara treatment effect in WT.

DMBA/TPA-induced skin papilloma formation is reduced and delayed in KO mice

Fgfbp1 expression is increased in mouse skin during carcinogen-induced papilloma formation (Kurtz et al. 2004) suggesting a potential role during carcinogenesis. Six week old GFP reporter mice ($Fgfbp1^{+/gfp}$) treated topically with DMBA/TPA (**Fig. 4a**) showed macroscopically visible GFP activitiy in papillomas **(Fig. 4b)**, GFP protein expression in the more differentiated outer keratinocyte layers of the epidermis **(Fig. 4c,** magnified in **Fig. S6a)** and >2-fold GFP mRNA (**Fig. 4d)**. In WT skin Fgfbp1 expression was induced similarly by 2.8-fold (**Fig. 4k**). Skin biopsies taken from carcinogen treated WT and KO mice showed a similar increase in hyperplastic keratinocyte layers as early as 12 days after the first treatment and maximal thickness at 57 days **(Fig. 4e)**. However, the appearance of skin papillomas was significantly ($p<0.01$) delayed in KO mice: The first lesions in WT mice were found after 1.5 months (day 44) and only a month later (day 73) in the KO group **(Fig. 4f, g)**. By day 100 all WT mice developed papilloma whereas one KO mouse remained papilloma-free until the end of the experiment **(Fig. 4g)**. Also, the number of papilloma per mouse was significantly reduced in the KO mice **(Fig. 4h)**.
In addition to the reduced papilloma formation, we observed an increase of ulceration in the neck region of KO mice (**Fig. S7a).** In earlier work, we had observed an impact of FGFBP proteins on vascular leakiness in embryonic tissues (Gibby et al. 2009) and it is known that altered vascular permeability can cause ulcerative inflammation (Nagy et al. 2008). Thus, we evaluated papilloma tissues for vessel integrity. Quite strikingly, the number of extravasated erythrocytes was increased >3-fold in the KO mice indicating a contribution of Fgfbp1 to vascular integrity in adult tissues (**Fig. 4 i, j).**

Pathway activation after DMBA/TPA challenges

To complement the phenotypic analyses, we compared the impact of DMBA/TPA treatment on the gene expression profile in skin and found robust gene expression difference associated with epidermal development, immune response and extracellular matrix (ECM) (**Fig. S8**). Carcinogen treatment induced the activated keratinocyte-specific genes Krt16 and Sprr2d to comparable levels in both WT and KO skin. Due to the elevated level at baseline, the relative induction by carcinogen was much lower in KO versus WT skin. The same pattern was observed for the immune response gene S100a8. Its baseline level expression in untreated KO skin was 13-fold higher than the expression in WT skin and the induction by carcinogen treatment elevated its expression to similar levels in both KO and WT. Finally, the ECM protease Klk6 was upregulated at baseline by 4.3-fold in KO skin. DMBA/TPA treatment induced its expression in both WT and KO skin (**Fig. 4k**). Immunohistochemistry confirmed the upregulation of the Krt13 and Krt16 protein in the epidermis as well as the downregulation of Col1A2 in the dermis during DMBA/TPA treatment (**Fig. S6b**).

An analysis of Fgfr mRNA by qRT-PCR did not show any significant differences in b/c splice isoform expression of Fgfr1, 2 and 3 **(Fig. S7b, c)**. Also, immunohistochemistry did not reveal any differences in phosphorylation of Fgfr1 (**Fig. S6b)** or difference in keratinocyte proliferation between WT and KO **(Fig. S6c).** Pathway analysis of the global gene expression patterns revealed that carcinogen treatment activated Tight Junction Signaling, Agranulocyte Adhesion, Extravasation and Diapedesis, Epithelial Adherens Junction Signaling, and Role of IL-17a in Psoriasis in both WT and KO skin. These pathways are already activated at baseline in the untreated KO skin **(Fig. S2a, b, c)**. Upstream regulators that are significantly altered with a z-score above 2 include Tnf,

LPS, Ifn-□, Nf□b, Cebp-□, Tgf-□1, all of which are involved in cancer pathways as well as inflammatory responses (**Fig. S2d, e)**.

Fgfbp1 expression is induced and required for timely wound healing

We have previously found that conditional transgenic FGFBP1 expression accelerates wound healing (Tassi et al. 2011). Complementary to that we observed a significant three-day delay in full-thicknewss skin wound healing in KO mice **(Fig. 5a, b**). This supports a significant contribution of endogenous Fgfbp1 to timely wound healing. Fgfbp1$^{+/gfp}$-reporter mice showed maximal levels of GFP fluorescence adjacent to the wounds on day 4 (**Fig. 5c, d**). This was corroborated by IHC that showed a high expression of GFP protein close to the wounds and a low expression at remote skin (**Fig. S9a**). Fgfbp1-expressing cells were identified as hyperpoliferating keratinocytes and inflammatory cells in the granulation tissue (**Fig. 5e** magnified in **Fig. S9b**). Microscopic analysis of wounds on day four (**Fig. 5f,** magnified in **Fig. S9c**) showed that the reëpithelialization of wounds in the WT mice was more advanced **(Fig. 5g).** Also, the granulation tissue in wounds in KO mice contained a significantly higher number of extravasated erythrocytes and fewer microvessels and capillaries than WT mice **(Fig. 5h,i magnified in Fig. S9c)** indicating less mature angiogenesis. There was a slight decrease in total cells in the granulation tissue of KO mice **(Fig S9d)** though no difference in their proliferation index (**Fig. S9e, f)**.

Fgfbp1-expressing cells are recruited to healing wounds

To investigate the expression of Fgfbp1 in cells recruited to healing wounds versus tissue resident cells we transplanted skin from WT donors onto the back of Fgfbp1$^{+/gfp}$ recipient mice. The transplanted skin was wounded and the fluorescence of the wound and the surrounding transplant tissue was monitored **(Fig. 6a)**. The inside of wounds in wild type skin transplanted to Fgfbp1$^{+/gfp}$ recipient mice started to fluoresce during wound healing even when surrounded by the non-fluorescent WT skin transplant (**Fig. 6b, c)** suggesting that GFP-expressing cells from the host entered the wound as early as two days after wounding. IHC analysis of the granulation tissue in the wound confirmed the influx of GFP-positive cells from the host **(Fig. 6b)**, thus corroborating that as late as five days after injury Fgfbp1-expressing cells localize to the wound**.**

In complementary experiments, Fgfbp1$^{+/gfp}$ skin transplanted and wounded on a WT recipient showed increased GFP activity at edge of a wound as it healed but the GFP activity inside the open wound did not increase significantly (**Fig. S10a-d**). These results suggest the contribution of circulating cells from the host to the wound healing of the transplant and we thus tested that next in a separate experimental setting.

To test whether bone marrow can provide Fgfbp1-expressing (GFP positive) cells via the circulation to a healing wound, we isolated bone marrow cells from Fgfbp1$^{+/gfp}$ mice and transplanted those into WT mice with skin wounds (**Fig. 6d)**. GFP fluorescence in the wounded area peaked at days two and three after wounding (**Fig. 6e, f**) and sections of the wounds showed strong GFP staining of cells in the granulation tissue (**Fig. 6e**, magnified in **Fig. S10e**). These transplant experiments demonstrate that Fgbp1-expressing cells home to the wound from both the circulation and adjacent tissue and

reveal that Fgfbp1-expressing bone marrow-derived cells are recruited to healing wounds.

Endogenous Fgfbp1 contributes to neoangiogenesis

Subcutaneous matrigel plugs are a well-defined model of neoangiogenesis that mimics part of the wound healing process and is driven by the invasion of monocytic cells recruited from the circulation (Anghelina et al. 2004). In earlier studies FGFBP1 was found expressed in tissue resident monocytes / macrophage (Ray et al. 2014) and gain-of-function studies had shown that expression of FGFBP1 enhances neoangiogenesis in a matrigel plug model (Tassi et al. 2011). In Fgfbp1-KO mice, a significant 3-4-fold reduction of cells that fully invade the matrigel plug and reach the center was observed. It is noteworthy that similar numbers of infiltrating cells were observed at the edges of the plugs (regions 1 and 5; **Fig. 6g, h**). Examination of matrigel plugs in Fgfbp1$^{+/gfp}$ reporter mice revealed a strong GFP staining of the majority of invasive cells. A large percentage of the Fgfbp1-expressing cells were inflammatory cells with multilobular nuclei **(Fig. S10f)**.

Additional phenotypic analysis of FGFBP1-KO mice

Fgfbp1-KO mice were viable and fertile and did not show any gross phenotypic abnormalities. The expected Mendelian ratio of the offspring indicated a lack of embryonic lethality in mice in contrast to chick embryonic development where FGFBP1 is crucial for survival (Gibby et al. 2009). To detect subtle phenotypic changes, we subjected a cohort of WT and KO animals to a systematic and comprehensive

characterization for 550 parameters that include behavior, neurology, morphology, metabolism, hematology and immunology (Fuchs et al. 2009). In summary of the analyses detailed in **Tables S1** to **S21,** and **Figs. S11** to **S16**, we found significant phenotypic alteration in KO mice in the ratio of fat versus lean body mass, food intake, spleen and heart weights, blood glucose, cholesterol, iron binding capacity, lactate, urea, serum IgG3 and IgE, behavioral tests, and in the auditory brain stem response.

Discussion

Previous studies have shown that FGFBP1 interacts with FGF1 and 2 as well as with members of the FGF7 subfamily i.e. FGF7, 10 and 22 (Beer et al. 2005). These FGFs are expressed in the skin and signal through the IIIb isoform of FGFRs. Indeed, FGF22-knockout mice develop fewer papilloma than WT mice during skin carcinogenesis while skin development and wound healing is not affected (Jarosz et al. 2012). Mice lacking keratinocyte Fgfr1b and Fgfr2b lose epidermal barrier function and the ability to maintain skin homeostasis (Yang et al. 2010). Also, a lack of Fgfr2b in keratinocytes made skin hypersensitive to papilloma formation (Grose et al. 2007). We have previously found that DMBA/TPA upregulates FGFBP1 in human skin grafted onto mice (Kurtz et al. 2004) and the analysis of published data shown above revealed increased FGFBP1 expression in hyperproliferative skin diseases such as psoriasis, actinic keratosis and SCC.

Here we report that endogenous Fgfbp1 plays a significant role in skin repair and carcinogenesis. While Fgfbp1-KO mice did not show any gross phenotypic abnormalities, a functional screen showed a decrease of transepidermal waterloss (TEWL) in KO mice that matches with significant thickening of the epidermal layer in

KO mice. Interestingly, keratinocyte-specific deletion of Fgfr1 and Fgfr2b resulted in changes of the barrier function and ulceration of mouse skin (Yang et al. 2010). Epidermal thickening was also observed in keratinocyte Fgfr2b-knockout skin (Grose et al. 2007). Taken together, the results show that FGFBP1 expression is induced upon injury and tissue regeneration, whilst loss of FGFBP1 slows the response to injury during the DMBA/TPA induced carcinogenesis, wound healing and invasion into a matrigel plug. We found that the FGFR1c isoform is upregulated and the isoform ratio is shifted towards the mesenchymal c-isoform in the KO epidermis. This indicates that the loss of FGFBP1 causes an increase in mesenchymal expression pattern in the skin. This may contribute to the increased epithelial barrier function of KO skin and matches with the mesenchymal transition of the epidermis during carcinogenesis (Tanner and Grose 2015). It is noteworthy that global gene expression changes in the skin of KO mice mimic the altered gene expression pattern observed after carcinogen treatment of WT skin. E.g. genes involved in epidermal development such as cytokeratins (Krt13, 16, 27, Sprr2d), immune response genes (Il6, Il17a, Il23, S100a8, S100a9) and the kallikrein peptidase, Klk6, are upregulated in the skin of KO mice. Indeed, these genes are upregulated in psoriasis (Kim et al. 2016; Schonthaler et al. 2013; Vinter et al. 2014) squamous cell carcinoma (De Heller-Milev et al. 2000; Ghosh et al. 2015; Iotzova-Weiss et al. 2015; Kishibe et al. 2007; Lessard and Coulombe 2012; Prassas et al. 2015; Reichelt et al. 2004) and in chronic wounds (Singh et al. 2016). Also, expression of the S100a8/a9 heterodimer which is thought to suppress papilloma formation (McNeill and Hogg 2014) is increased in the skin of KO mice (**Fig. 4k).** Overall the loss of Fgfbp1 increases the pro-inflammatory gene expression in the skin.

The deletion of FGF22 led to a delay in carcinogen-induced papilloma formation (Jarosz et al. 2012) matching with our results. Wound healing was, however, not affected in FGF22-KO mice. Also, it has been shown that lack of FGFR2b in keratinocytes leads to increased and spontaneous papilloma formation suggesting that FGFR2b functions as a tumor suppressor in the skin (Grose et al. 2007). Our results are somewhat different since we observed a strong upregulation of the mesenchymal FGFR1c in the epidermis of KO mice. This might increase the mesenchymal character of the epidermis preventing hyperproliferation of the keratinocytes in the epidermal layer of the skin. Finally, vascular leakage in papilloma and wound granulation tissues in KO mice is reminiscent of vascular leakage after FGFBP1 knock-down in chicken embryos (Gibby et al. 2009).

The Fgfbp1$^{+/gfp}$ reporter mice allowed us to distinguish between the contribution of locally resident and systemically recruited Fgfbp1-expressing cells. In the skin transplant experiments Fgfbp1-expressing cells migrate into healing wounds as indicated by GFP activity in the granulation tissue. Furthermore, the bone marrow transplant from Fgfbp1$^{+/gfp}$ reporter mice shows that these infiltrating cells originate from bone marrow and enter the wounds via the circulation. The model also demonstrates that Fgfbp1 is an indicator of differentiation of infiltrating cells. Early during wound healing infiltrating cells are derived from the hematopoetic lineage in the bone marrow but switch to mesenchymal progenitor cells during tissue remodeling (Opalenik and Davidson 2005). In our study, during the inflammatory phase of wound healing (day 4) most of the inflammatory cells express Fgfbp1. Similarly, in the neoangiogenesis matrigel assay the majority of invasive, inflammatory cells express Fgfbp1. This corroborates previous

results by us and others that FGFBP1 is expressed in tissue-infiltrating monocytes / macrophage (Ray et al. 2014).

In conclusion, our study identifies endogenous Fgfbp1 as a significant modulator of pathways that are involved in early carcinogenesis and inflammatory tissue regeneration and links Fgfbp1 expression to tissue-infiltrating inflammatory cells from the bone marrow.

Material and Methods

Generation of knockout mice

The Fgfbp1-knockout targeting vector, Fgfbp1-KO mice and Fgfbp1^{gfp} mice in a C57BL/6 and SV129 mixed background were generated by Ingenious Targeting Company and is described in the Supplemental Materials.

Transepidermal Water Loss (TEWL)

Mouse skin was analyzed in a non-invasive manner with a special Tewameter (AquaFlux AF200) that was placed on the skin. During a short time of 60 to 90 seconds TEWL [g/(m2h)] was recorded (Fluhr et al. 2006).

Illumina RNA expression assay and Ingenuity pathway analysis

PolyA RNA was analyzed by the UCLA Neuroscience Genomics core utilizing an Illumina bead array (Mouse ref 8 v 2.0) system. RNA expression values were evaluated with the Ingenuity Pathway analysis software.

Separation of dermis from epidermis

The epidermis dissociation kit (Miltenyi Biotec) was used for epidermis dermis separation according to manufacturer's instructions.

Statistical Analyses

Prism 5 (GraphPad) software was used to compare the means of two or more groups by Student's *t*-test or analysis of variance, respectively. Statistical significance was defined as $P < 0.05$. Figures legends: *, P<0.05; **, P<0.01; ***, P<0.001

An expanded Methods section is available in the Supplementary Materials and Methods.

Figure Legends:

Figure 1: Generation of Fgfbp1 KO and GFP-knock-in mice. (**a**) Schematic of the knockout strategy for the Fgfbp1 gene depicts the endogenous locus of the Fgfbp1 gene on chromosome 5 and the targeting construct below. Mice with the targeted insertion of a floxed Fgfbp1 Neo and Gfp cassette in the Fgfbp1 locus ($Fgfbp1^{loxP\text{-}neo\text{-}gfp}$) were crossed with Cre expressing mice resulting in an insertion of a GFP reporter allele ($Fgfbp1^{gfp}$), or with FLPase mice resulting in a floxed Fgfbp1 ($Fgfbp1^{loxp}$) allele. $Fgfbp1^{loxP}$ mice were further crossed with cre-mice to generate Fgfbp1-KO mice ($Fgfbp^{-/-}$, KO). Numbered arrows depict locations of genotyping primer (**Suppl. Table S22).** (**b-f**) PCR analysis of genomic DNA isolated from tail snips. (**b**) Primers 4 and 7 resulted in an amplicon of

5000 bp only in the allele with the floxed Fgfbp1 Neo and GFP cassette. (**c**) Primers 1 and 2 resulted in an amplicon of 478 bp with the 5'loxP site in the floxed Fgfbp1 allele and 416 bp in the WT allele. (**d**) Primers 3 and 6 resulted in an amplicon of 582 bp with the 3'loxP site in the floxed Fgfbp1 allele and 463 bp in the WT allele. (**e**) Primers 1 and 5 resulted in an amplicon of 484 bp only in the GFP reporter allele. (**f**) Primers 1 and 6 resulted in an amplicon of 432 bp in the KO allele and 2.5kb in the WT allele.

Figure 2: Fgfbp1-KO mouse epidermis is thicker and has reduced permeability. (**a,b**) Representative high magnification pictures of Masson's trichrome stained tissue section of skin from WT and KO mice shows a thicker epidermal layer (E) in KO mice. (**b**) In contrast to the epidermis, dermis, fat layer and muscle are not significantly different. (Mann Whitney test, WT n=5; KO n=6; 20 fields per skin sample). (**c**) Proliferation of basal keratinocytes in KO epidermis is higher than in WT (PCNA positive nuclei, Student's t test, n=5). (**d**) Keratinocyte layers in KO epidermis contains multiple layers whereas WT epidermis ist mostly a monolayer (Chi-square test, n=3), (**e**) Representative images of skin section stained for Claudin 1, Filaggrin, PCNA (scale bar = 100 µm). (**f**) Transepidermal water loss (TEWL) was decreased in male KO compared to WT males (Student's t test, WT n=14; KO n=15). (**g**) RNA expression in separated dermis and epidermis (Student's t test, WT n=4; KO n=3).

Figure 3: Effect of topical Aldara treatment. (**a**) Daily treatment of shaved back skin of Fgfbp1^{gfp} mice for 4 days. Skin turned red as the inflammation progresses. (**b**) Myeloperoxidase (MPO) activity (Student's t-test, WT n=4; KO n=5). (**c**) Induction of

Fgfbp1 expression in WT skin. (**d**) GFP fluorescence in Aldara and ctrl (vaseline) treated mice for 5 days. Fluorescence intensity is shown as scaled counts/s in a heatmap from 0 (black) to 0.8 (dark red). (**e**) Quantification of GFP-fluorescence in panel **b** (Chi-square, n=2). (**f**) Masson's trichrome stained tissue sections of WT and KO epidermis (scale bar = 50 μm). (**g**) Quantification of the thickness of the epidermis (Student's t-test, n=7). (**h**) Effect on mRNA expression of Krt16, Il6, Il17a and Il23. (Student's t test, n=7)

Figure 4: DMBA/TPA (D/T) effects are delayed in Fgfbp1-KO mice. (**a**) Treatment scheme: A single topical treatment with DMBA was followed by biweekly TPA treatments for 180 days. (**b**) In vivo fluorescence of Fgfbp1$^{+/gfp}$ mouse skin after 180 days of treatment shows GFP activity in papillomas. Visible (left panel) and green fluorescence channels (right panel) are shown. Arrows indicate papillomas (scale bar = 5 mm). (**c**) Immunostaining of representative tissue sections with anti-GFP antibody shows staining of the epidermis (E) excluding the basal layer of keratinocytes. (Dermis (D), scale bar =200 μm (top panel), 100 μm (bottom panel), magnified in **Suppl. Fig. S6a**), (**d**) GFP RNA expression in Fgfbp1$^{+/gfp}$ mice after 180 days of treatment (n=3). (**e**) The thickness of the epidermal layer progressively increased upon treatment. Biopsies were taken and the epidermal thickness was measured. On days 57 and 124 only papilloma-free skin sections were measured. (**f**) Papilloma on day 161. (**g**) Kaplan-Meier plot of papilloma occurrence ($p<0.01$; Mantel-Cox test, WT n=9; KO n=8). (**h**) Papilloma frequency (2-way ANOVA, WT n=9; KO n=8). (**i**) Vascular leakiness in papilloma indicated by extravasated erythrocytes (student's t-test, n=5, 35 fields per sample). (**j**) Representative anti CD31-stained tissue section; E=epidermis, V=vessel; interrupted

white line surrounds area with extravasated erythrocytes (scale bar = 100 µm). (**k**) Illumina bead array analysis of DMBA/TPA treated skin shows induction of Fgfbp1 (left panel) and increased expression of S100a8, Krt16, Sprr2d and Klk6. Baseline expression is higher in Fgfbp1-KO skin but induced upon DMBA/TPA treatment (Student's t-test, WT n=4; KO n=3).

Figure 5: Wound healing is delayed in Fgfbp1-KO mice. (**a**) The back skin of WT and KO mice was wounded on day 0 and wound sizes were measured daily for 7 days (scale bar = 5 mm). (**b**) Quantification of wound sizes (2-way Anova, WT n=20; KO n=12). (**c**) Activation of the Fgfbp1 expression during wound healing indicated by fluorescence in Fgfbp1$^{+/gfp}$ mouse skin. Heat map images are shown (scale bar = 2.5 mm). (**d**) GFP quantitation after wounding. GFP fluorescence peaks on day 4 (student's t-test for each time point, n=10). (**e**) Immunostaining of representative tissue sections with anti-GFP antibody (scale bar = 1 mm, magnified scale bar 100 µm, higher magnification in **Suppl. Fig. S9b**). (**f**) Representative images of hematoxylin/eosin stained wounds (scale bar = 1 mm), magnified sections show extravasated red blood cells (eR), single erythrocytes (arrow heads); (scale bar = 100 µm, granulation tissue (G), fat (F), scab (S), dermis (D), muscle (M), hair follicles/glands (H), epidermis (E) (higher magnification in **Suppl. Fig S9c).** (**g**) Relative opening of wounds, calculated by the ratio between wound opening divided by wound diameter (distance between collagen-containing dermis times 100, n=5). (**h**) Quantification of extravasated erythrocytes (Student's t test; WT n=5; KO n=6 wounds; means of at least 10 fields per wound). (**i**) Quantification of microvessels and capillaries (Student's t test, WT n=5; KO n=6 wounds; at least 10 fields per wound).

Figure 6: Fgfbp1-expressing cells migrate into wounds. (**a to c**) Host Fgfbp1 expressing cells enter wound in transplanted skin. (**a**) Time line (in days) and schematic of experiments. Skin from a WT mouse was transplanted onto the back of a $Fgfbp1^{+/gfp}$ mouse, wounded after 7 days and fluorescence monitored. (**b**) Left panels: Bright field images and GFP fluorescence during wound healing (scale bar = 5 mm). Right panels: Immunostaining of a representative tissue section with an anti-GFP antibody shows staining of inflammatory cells that entered transplanted skin wound (scale bar = 250 µm). (**c**) Quantification of GFP signal in intact and wounded skin transplant (2-way Anova, n=7). (**d to f**) Wound healing with concurrent bone marrow transplant from the $Fgfbp1^{+/gfp}$ reporter model. (**d**) Schematic of the experiment. (**e**) Bright field and GFP fluorescence images of wounds over 4 days (scale bar = 5 mm). Immunostaining of representative tissue sections with anti-GFP antibody confirmed GFP-positive cells in granulation tissue of the wound (Scale bars = 500 µm top right panel, 100 µm bottom right panel; higher magnification in **Suppl. Fig. S10e**). (**f**) Quantification of GFP activity; 2-way Anova, n=8. (**g**) Matrigel plug neoangiogenesis assay. H&E stained tissue sections of subcutaneously injected matrigel after 7 days in WT and KO mice. Scale bar, 100 µm. (**h**) Quantification of invasive cells per field in different regions of the matrigel. Regions 1 and 5 represent the edges of the plugs, regions 2-4 the center; WT n=12; KO n=20.

Acknowledgements: This work has been funded by NIH grant P01 HL068686 to A. W. and by the German Federal Ministry of Education and Research to the GMC (Infrafrontier grant 01KX1012).

Footnote:

[§]German Mouse Clinic, Helmholtz Zentrum München, German Research Center for Environmental Health GmbH, Neuherberg, Germany

Lore Becker[1,3], Alexandra Vernaleken[1,3], Thomas Klopstock[3,12,13,16,17], Thure Adler[1], Irina Treise[1], Dirk H. Busch [2], Marion Horsch[1], Johannes Beckers[1,14,15], Kristin Moreth[1], Raffi Bekeredjian[4], Lillian Garrett[1,6], Sabine M. Hölter[1,6], Annemarie Zimprich[1,6], Wolfgang Wurst [6,11,12,13], Robert Brommage[1], Wolfgang Hans[1], Oana Amarie[1,6], Jochen Graw [6], Jan Rozman [1,15], Martin Klingenspor[7,8], Julia Calzada-Wack[1,5], Patricia da Silva-Buttkus[1,5], Frauke Neff[1,5], Ildiko Racz[1,9], Andreas Zimmer[9], Birgit Rathkolb [1,10,15], Eckhard Wolf [10], Manuela Östereicher[1], Ralph Steinkamp[1], Christoph Lengger[1], Holger Maier[1], Claudia Stoeger[1], Stefanie Leuchtenberger[1]

1 German Mouse Clinic, Institute of Experimental Genetics, Helmholtz Zentrum München, German Research Center for Environmental Health GmbH, Ingolstädter Landstrasse 1, 85764 Neuherberg, Germany

2 Institute for Medical Microbiology, Immunology and Hygiene, Technical University of Munich, Trogerstrasse 9, 81675 Munich, Germany

3 Department of Neurology, Friedrich-Baur-Institut, Ludwig-Maximilians-Universität Ziemssenstrasse 1a, 80336 Munich, Germany

4 Department of Cardiology, University of Heidelberg, Im Neuenheimer Feld 410, 69120 Heidelberg, Germany

5 Institute of Pathology, Helmholtz Zentrum München, German Research Center for Environmental Health GmbH, Ingolstädter Landstrasse 1, 85764 Neuherberg, Germany

6 Institute of Developmental Genetics, Helmholtz Zentrum München, German Research Center for Environmental Health GmbH, Ingolstädter Landstrasse 1, 85764 Neuherberg, Germany

7 Chair for Molecular Nutritional Medicine, Technische Universität München, Else Kröner-Fresenius Center for Nutritional Medicine, 85350 Freising, Germany

8 ZIEL – Center for Nutrition and Food Sciences, Technische Universität München, 85350 Freising, Germany

9 Institute of Molecular Psychiatry, Medical Faculty, University of Bonn, Sigmund-Freud-Strasse 25, 53127 Bonn, Germany

10 Ludwig-Maximilians-Universität München, Gene Center, Institute of Molecular Animal Breeding and Biotechnology, Feodor-Lynen Strasse 25, 81377 Munich, Germany

11 Chair of Developmental Genetics, Center of Life and Food Sciences Weihenstephan, Technische Universität München, Ingolstädter Landstrasse 1, 85764 Neuherberg, Germany

12 Deutsches Institut für Neurodegenerative Erkrankungen (DZNE) Site Munich, Schillerstrasse 44, 80336 Munich, Germany

13 Munich Cluster for Systems Neurology (SyNergy), Adolf-Butenandt-Institut, Ludwig-Maximilians-Universität München, Schillerstrasse 44, 80336 Munich, Germany

14 Chair of Experimental Genetics, Center of Life and Food Sciences Weihenstephan, Technische Universität München, Ingolstädter Landstrasse 1, 85354 Freising-Weihenstephan, Germany

15 Member of German Center for Diabetes Research (DZD), Ingolstädter Landstraße 1, 85764 Neuherberg, Germany

16 German Network for Mitochondrial Disorders (mitoNET)

17 German Center for Vertigo and Balance Disorders, Munich, Germany

References cited

Aigner A, Ray PE, Czubayko F, Wellstein A. Immunolocalization of an FGF-binding protein reveals a widespread expression pattern during different stages of mouse embryo development. Histochem Cell Biol. 2002;117(1):1–11

Anghelina M, Krishnan P, Moldovan L, Moldovan NI. Monocytes and macrophages form branched cell columns in matrigel: implications for a role in neovascularization. Stem Cells Dev. 2004;13(6):665–76

Beer H-D, Bittner M, Niklaus G, Munding C, Max N, Goppelt A, et al. The fibroblast growth factor binding protein is a novel interaction partner of FGF-7, FGF-10 and FGF-22 and regulates FGF activity: implications for epithelial repair. Oncogene. 2005;24(34):5269–77

Czubayko F, Liaudet-Coopman ED, Aigner A, Tuveson AT, Berchem GJ, Wellstein A. A secreted FGF-binding protein can serve as the angiogenic switch in human cancer. Nat Med. 1997;3(10):1137–40

Czubayko F, Smith RV, Chung HC, Wellstein A. Tumor-Growth and Angiogenesis Induced by a Secreted Binding-Protein for Fibroblast Growth-Factors. J. Biol. Chem. 1994;269(45):28243–8

De Heller-Milev M, Huber M, Panizzon R, Hohl D. Expression of small proline rich proteins in neoplastic and inflammatory skin diseases. Br. J. Dermatol. 2000;143(4):733–40

Fluhr JW, Feingold KR, Elias PM. Transepidermal water loss reflects permeability barrier status: validation in human and rodent in vivo and ex vivo models. Exp. Dermatol. 2006;15(7):483–92

Fuchs H, Gailus-Durner V, Adler T, Pimentel JAA, Becker L, Bolle I, et al. The German Mouse Clinic: A Platform for Systemic Phenotype Analysis of Mouse Models. Curr Pharm Biotechnol. 2009;10(2):236–43

Ghosh D, Ding L, Sivaprasad U, Geh E, Biagini Myers J, Bernstein JA, et al. Multiple Transcriptome Data Analysis Reveals Biologically Relevant Atopic Dermatitis Signature Genes and Pathways. Simon M, editor. PLoS ONE. 2015;10(12):e0144316

Gibby KA, McDonnell K, Schmidt MO, Wellstein A. A distinct role for secreted fibroblast growth factor-binding proteins in development. Proc Natl Acad Sci USA. 2009;106(21):8585–90

Grose R, Fantl V, Werner S, Chioni A-M, Jarosz M, Rudling R, et al. The role of fibroblast growth factor receptor 2b in skin homeostasis and cancer development. EMBO J. 2007;26(5):1268–78

Guban B, Vas K, Balog Z, Manczinger M, Bebes A, Groma G, et al. Abnormal regulation of fibronectin production by fibroblasts in psoriasis. Br. J. Dermatol. 2016;174(3):533–41

Henke RT, Eun Kim S, Maitra A, Paik S, Wellstein A. Expression analysis of mRNA in formalin-fixed, paraffin-embedded archival tissues by mRNA in situ hybridization. Methods. 2006;38(4):253–62

Iotzova-Weiss G, Dziunycz PJ, Freiberger SN, Läuchli S, Hafner J, Vogl T, et al. S100A8/A9 Stimulates Keratinocyte Proliferation in the Development of Squamous Cell

Carcinoma of the Skin via the Receptor for Advanced Glycation-End Products. Hudson BI, editor. PLoS ONE. 2015;10(3):e0120971

Jarosz M, Robbez-Masson L, Chioni A-M, Cross B, Rosewell I, Grose R. Fibroblast growth factor 22 is not essential for skin development and repair but plays a role in tumorigenesis. PLoS ONE. 2012;7(6):e39436

Kim KE, Houh Y, Park HJ, Cho D. Therapeutic Effects of Erythroid Differentiation Regulator 1 on Imiquimod-Induced Psoriasis-Like Skin Inflammation. Int J Mol Sci. 2016;17(2)

Kishibe M, Bando Y, Terayama R, Namikawa K, Takahashi H, Hashimoto Y, et al. Kallikrein 8 is involved in skin desquamation in cooperation with other kallikreins. J Biol Chem. 2007;282(8):5834–41

Kurtz A, Aigner A, Cabal-Manzano RH, Butler RE, Hood DR, Sessions RB, et al. Differential regulation of a fibroblast growth factor-binding protein during skin carcinogenesis and wound healing. NEO. 2004;6(5):595–602

Kurtz A, Wang HL, Darwiche N, Harris V, Wellstein A. Expression of a binding protein for FGF is associated with epithelial development and skin carcinogenesis. Oncogene. 1997;14(22):2671–81

Lessard JC, Coulombe PA. Keratin 16–Null Mice Develop PalmoplantarKeratoderma, a Hallmark Feature of PachyonychiaCongenita and Related Disorders. J Investig Dermatol. Elsevier Masson SAS; 2012;132(5):1384–91

McNeill E, Hogg N. S100A9 has a protective role in inflammation-induced skin carcinogenesis. Int J Cancer. 2014;135(4):798–808

Nagy JA, Benjamin L, Zeng H, Dvorak AM, Dvorak HF. Vascular permeability, vascular hyperpermeability and angiogenesis. Angiogenesis. 2008;11(2):109–19

Nair RP, Duffin KC, Helms C, Ding J, Stuart PE, Goldgar D, et al. Genome-wide scan reveals association of psoriasis with IL-23 and NF-κB pathways. Nat Genet. 2009;41(2):199–204

Nindl I, Dang C, Forschner T, Kuban RJ, Meyer T, Sterry W, et al. Identification of differentially expressed genes in cutaneous squamous cell carcinoma by microarray expression profiling. Mol. Cancer. 2006;5:30

Opalenik SR, Davidson JM. Fibroblast differentiation of bone marrow-derived cells during wound repair. FASEB J. 2005;19(11):1561–3

Prassas I, Eissa A, Poda G, Diamandis EP. Unleashing the therapeutic potential of human kallikrein-related serine proteases. Nature reviews Drug discovery. 2015;14(3):183–202

Ray PE, Al-Attar A, Liu X-H, Das JR, Tassi E, Wellstein A. Expression of a Secreted Fibroblast Growth Factor Binding Protein-1 (FGFBP1) in Angioproliferative Kaposi Sarcoma. J AIDS Clin Res. 2014;05(06)

Reichelt J, Furstenberger G, Magin TM. Loss of keratin 10 leads to mitogen-activated protein kinase (MAPK) activation, increased keratinocyte turnover, and decreased tumor formation in mice. J. Invest. Dermatol. 2004;123(5):973–81

Reischl J, Schwenke S, Beekman JM, Mrowietz U, Stürzebecher S, Heubach JF. Increased expression of Wnt5a in psoriatic plaques. J. Invest. Dermatol. 2007;127(1):163–9

Schonthaler HB, Guinea-Viniegra J, Wculek SK, Ruppen I, Ximénez-Embún P, Guío-Carrión A, et al. S100A8-S100A9 Protein Complex Mediates Psoriasis by Regulating the Expression of Complement Factor C3. Immunity. Elsevier Inc; 2013;39(6):1171–81

Singh K, Agrawal NK, Gupta SK, Sinha P, Singh K. Increased expression of TLR9 associated with pro-inflammatory S100A8 and IL-8 in diabetic wounds could lead to unresolved inflammation in type 2 diabetes mellitus (T2DM) cases with impaired wound healing. J. Diabetes Complicat. 2016;30(1):99–108

Stern RS. Psoriasis. The Lancet. 1997;350(9074):349–53

Tanner Y, Grose RP. Dysregulated FGF signalling in neoplastic disorders. Seminars in Cell and Developmental Biology. 2015;

Tassi E, Wellstein A. The angiogenic switch molecule, secreted FGF-binding protein, an indicator of early stages of pancreatic and colorectal adenocarcinoma. Semin. Oncol. 2006;33(6):S50–6

Tassi E, McDonnell K, Gibby KA, Tilan JU, Kim SE, Kodack DP, et al. Impact of fibroblast growth factor-binding protein-1 expression on angiogenesis and wound healing. Am J Pathol. 2011;179(5):2220–32

van der Fits L, Mourits S, Voerman JSA, Kant M, Boon L, Laman JD, et al. Imiquimod-Induced Psoriasis-Like Skin Inflammation in Mice Is Mediated via the IL-23/IL-17 Axis. J Immunol. 2009;182(9):5836–45

Vinter H, Iversen L, Steiniche T, Kragballe K, Johansen C. Aldara-induced skin inflammation - studies of psoriasis patients. Br. J. Dermatol. 2014;

Walter A, Schaefer M, Cecconi V, Matter C, Urosevic-Maiwald M, Belloni B, et al. Aldara activates TLR7-independent immune defence. Nature Communications. 2013;4

Yang J, Meyer M, Müller A-K, Böhm F, Grose R, Dauwalder T, et al. Fibroblast growth factor receptors 1 and 2 in keratinocytes control the epidermal barrier and cutaneous homeostasis. J Cell Biol. 2010;188(6):935–52

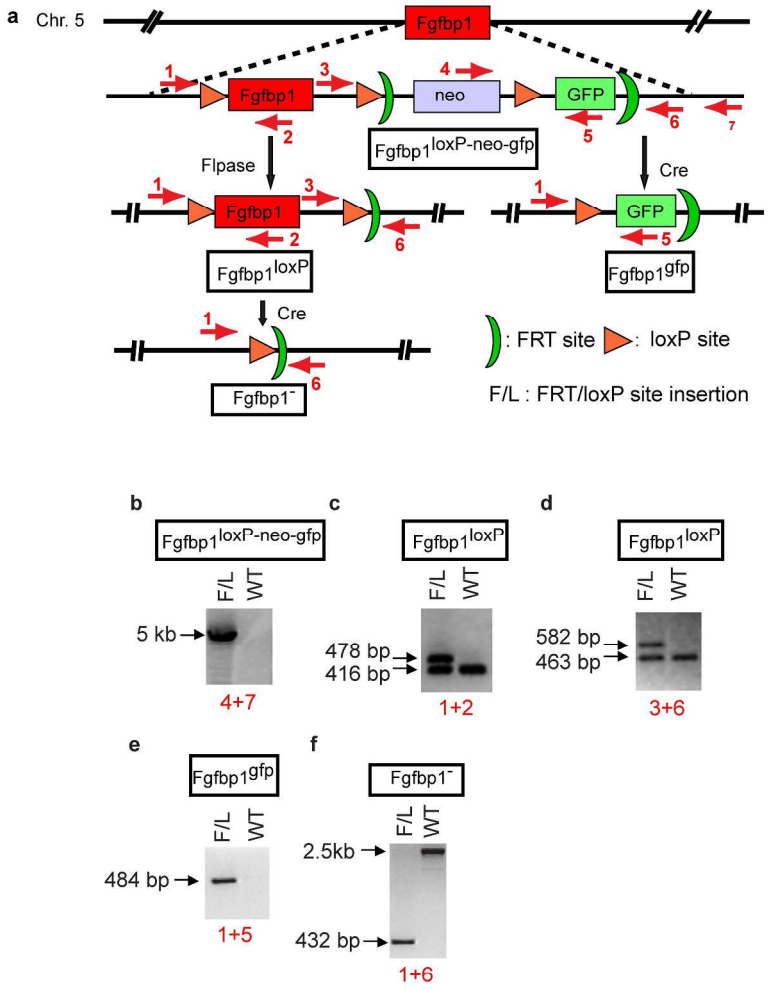

Schmidt et al., Figure 1

Generation of Fgfbp1 KO and GFP-Knock-in mice

279x361mm (300 x 300 DPI)

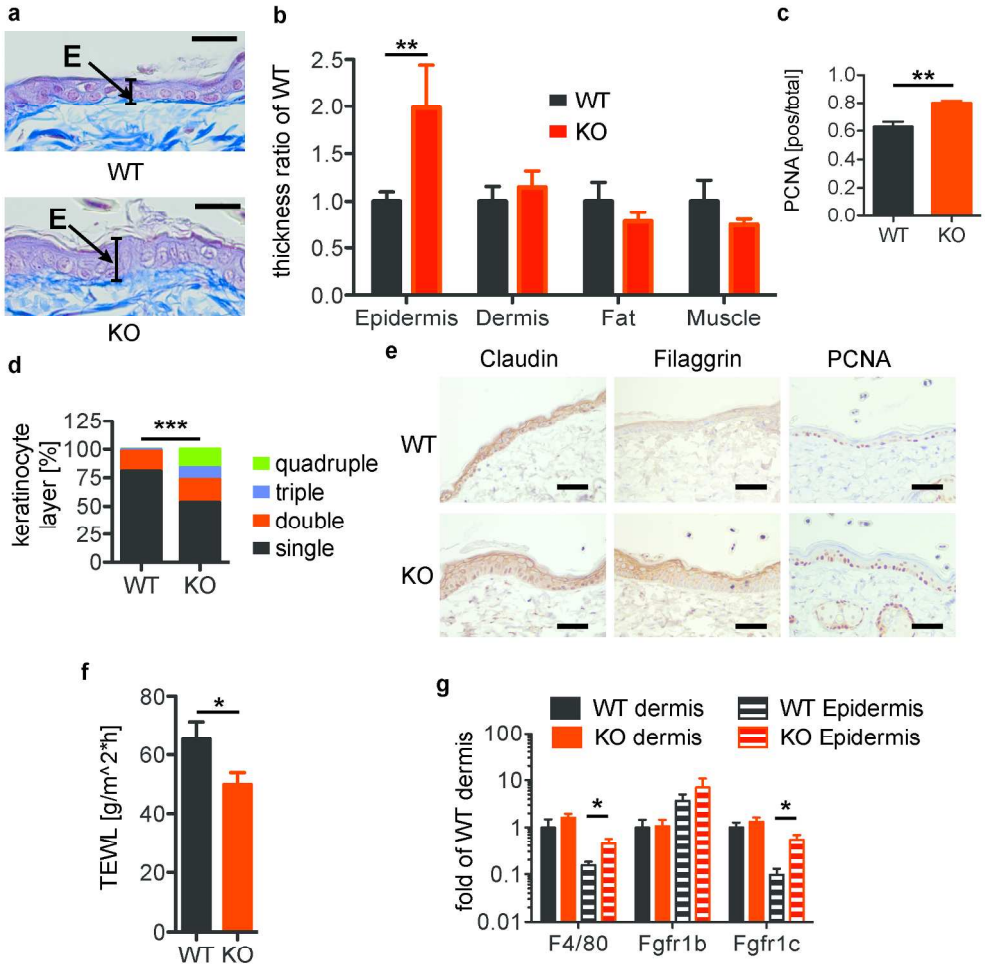

Schmidt et al., Figure 2

Figure: Fgfbp1-KO mice epidermis is thicker and has reduced permeability

212x222mm (300 x 300 DPI)

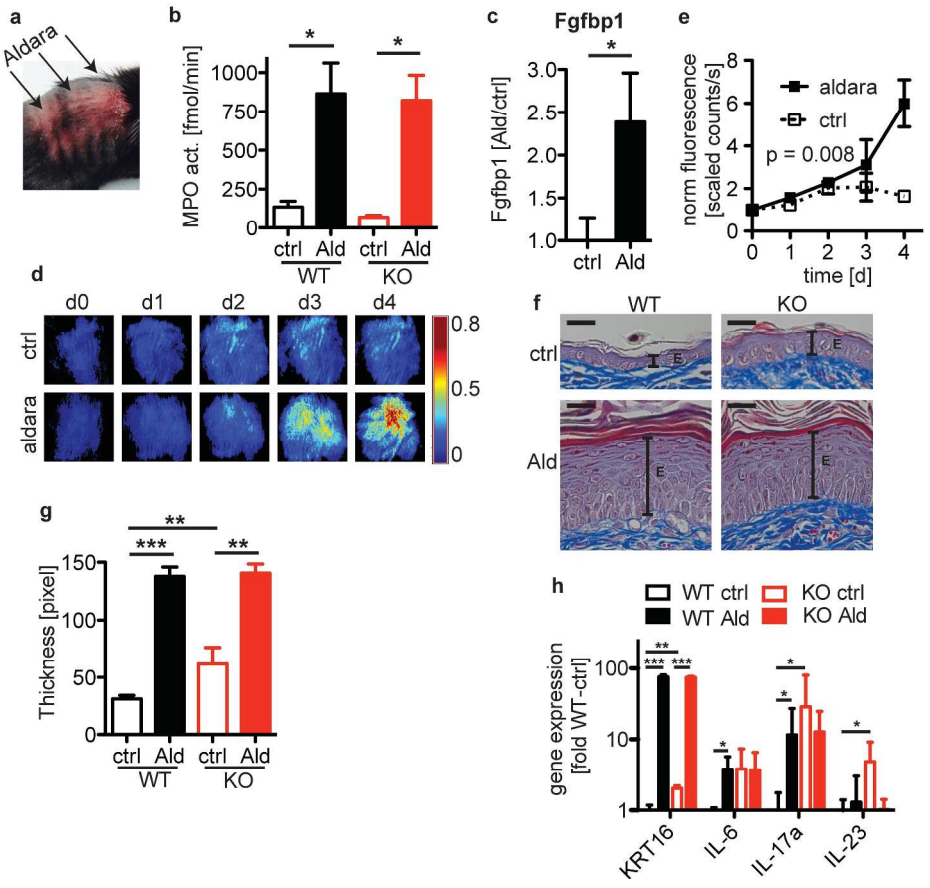

Schmidt et al. Figure 3

Figure 3: Effect of topical Aldara treatment.

279x361mm (300 x 300 DPI)

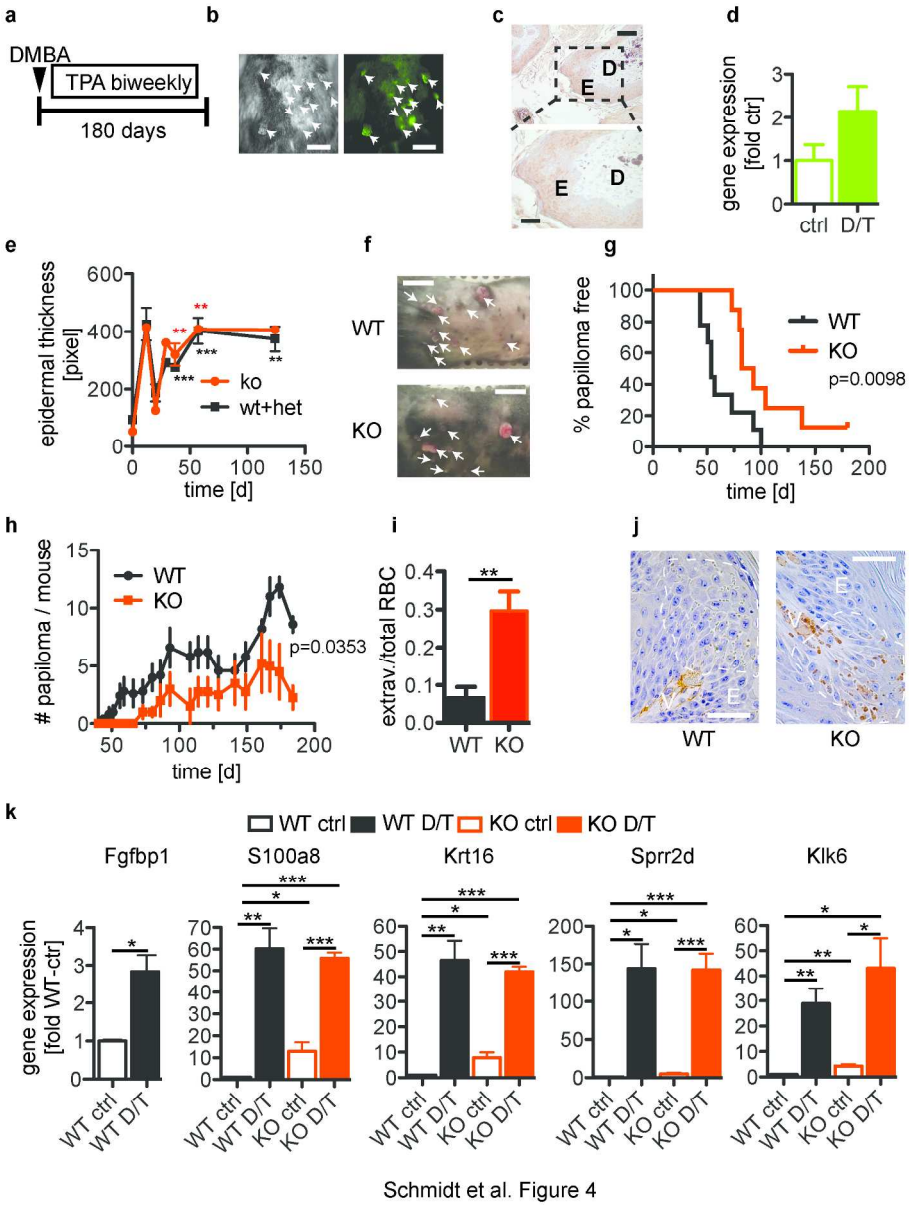

Schmidt et al. Figure 4

Figure 4: DMBA/TPA (D/T) effects are delayed in Fgfbp1-KO mice.

210x276mm (300 x 300 DPI)

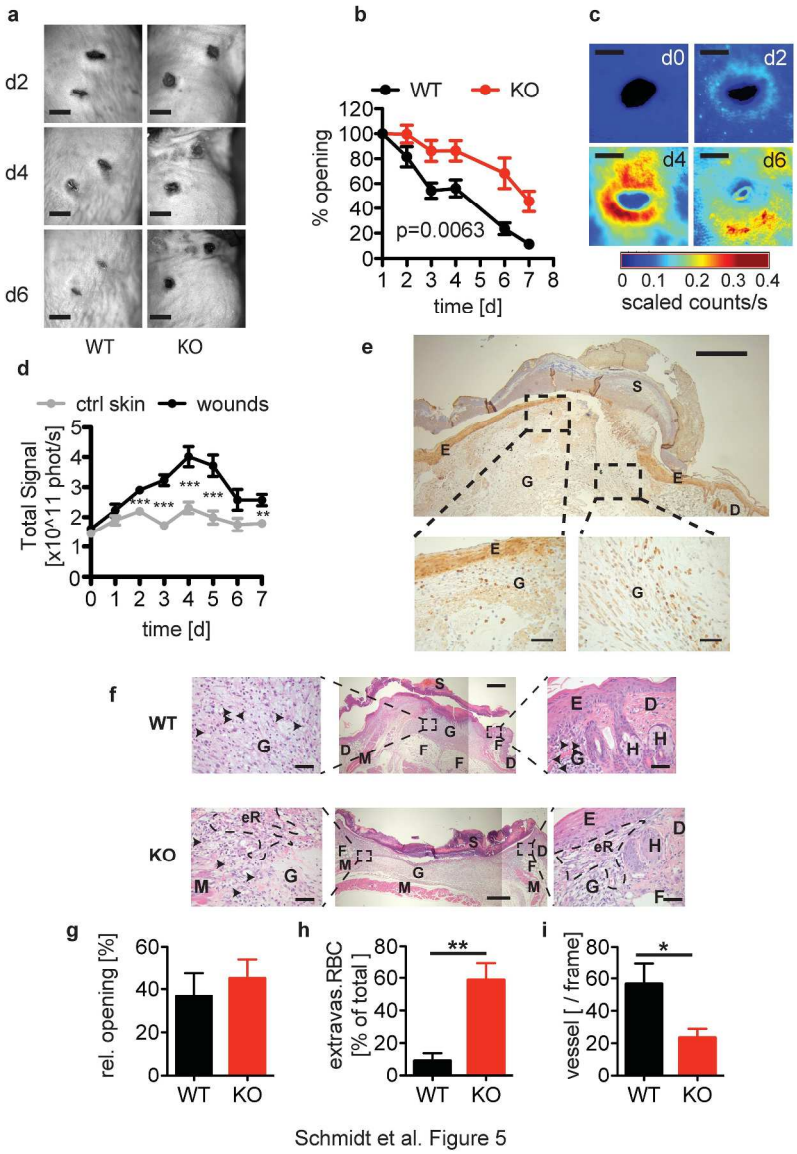

Figure 5: Wound healing is delayed in Fgfbp1-KO mice.

279x361mm (300 x 300 DPI)

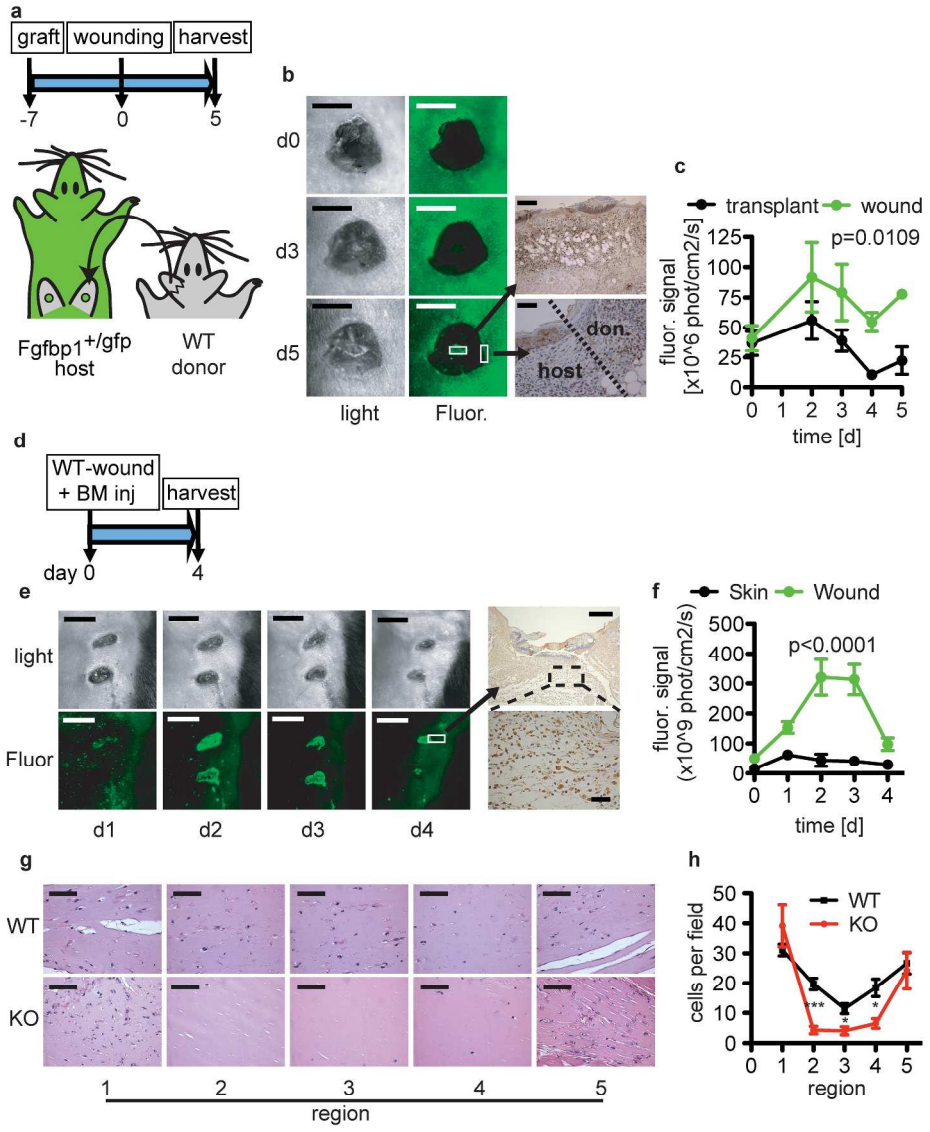

Schmidt et al. Figure 6

Figure 6: Fgfbp1-expressing cells migrate into wounds

279x361mm (300 x 300 DPI)

Supplemental Materials and Methods:

Mice

Mice were housed with food and water available *ad libitum* under standard laboratory conditions. Animals were separated based on sex, but not genotype. All animal studies were approved by Georgetown University's institutional animal care and use committee and conducted according to the NIH Guide for the Care and Use of Laboratory Animals.

Generation of knockout mice

The Fgfbp1-knockout targeting vector and mutant mice were generated by Ingenious Targeting Company. In short, a targeting vector with exon 2 of Fgfbp1 flanked by loxP and FRT sites, neo and GFP cassettes was inserted into mouse embryonic stem cells (C57Bl/6N;129/SvEv) and injected into blastocysts derived from C57Bl/6N mice. The resulting chimeras were mated with C57Bl/6N mice to generate F1 offspring, which were screened for $Fgfbp1^{loxP\text{-}neo\text{-}gfp}$ mice. GFP reporter knock-in ($Fgfbp1^{gfp}$) mice were generated by crossing $Fgfbp1^{loxP\text{-}neo\text{-}gfp}$ mice with (C57BL/6; SV129) R26CreERT2- mice (NCI #01XAB) and the offspring was fed Tamoxifen in their regular chow. After inbreeding $Fgfbp1^{gfp}$ mice without cre transgene were selected.

Fgfbp1-KO mice were generated by crossing $Fgfbp1^{loxP\text{-}neo\text{-}gfp}$ mice with C57BL/6 FLP mice (derived from JAX #003800, further backcrossed to C57BL/6 for 10 generations). After inbreeding $Fgfbp1^{loxP}$ mice without FLP transgene were selected and further crossed with (C57BL/6; SV129) R26CreERT2- mice (NCI #01XAB) and treated with Tamoxifen in their regular chow. Resulting mice were crossed and Fgfbp1-KO mice

without cre transgene were selected. Each crossing step was accompanied by PCR-based genotyping of tail snip DNA with primers (**Table S22**) resulting in specific bands for wt and mutant mice, respective (**Fig. 1**).

Aldara treatment

The backs of twelve week old mice were shaved and treated topically daily for four days with 50 µl of commercially available Aldara cream (active ingredient: 5% Imiquimod, Taro) and Petroleum Jelly (Vaseline, Unilever) as control. Each mouse was treated with Aldara on the upper-right side of its back and Vaseline on the upper-left side of its back. The skin was harvested on day five 24 hours after the last treatment.

DMBA/TPA treatment

The backs of twelve week old male mice were shaved and treated topically first with 7,12-dimethylbenz[a]anthracene (DMBA, 200 µg in 200 µl Acetone) followed by twice weekly treatments with 12-O-tetradecanoylphorbol-13- acetate (TPA, 10 µg in 200 µl Acetone) for up to 190 days. Control treatment was performed with 200 µl acetone at the same time intervals as DMBA/TPA treatments. Papillomas were counted on TPA treatment days. In a subset of mice biopsies (2 mm diameter punch; Miltex) were taken one hour after treatment with TPA. The skin was harvested 24 hours after the last treatment.

Wound Healing Assay

A dermal biopsy punch (3 mm diameter; Miltex Inc.) was used to create four, full-thickness skin wounds on the skin in anesthetized three months old female mice. Wounds were photographed daily with the Maestro2 *in vivo* imaging system (CRI, PerkinElmer) and wound sizes were measured using NIH ImageJ software. Mice were euthanized at 4 and 7 days and wounded tissues harvested. Histological sections were cut at a right angle to the skin surface across the wound. Serial paraffin-embedded tissue sections (5 µm) were stained with hematoxylin and eosin (H&E)

Transplant

For transplants dorsal ear skin from euthanized 3 months old donor mice was separated from the collagenous ventral side {Garrod:2008iv} in ice cold saline (PBS). Recipient 3 months old female mice were shaved on the back and two ca. 1 cm diameter skin pieces were removed from the upper left and and right side of the back. The donor skins were placed into the transplant sites with minimal overlap of the recipient's skin. The recipient mouse was wrapped in a bandage for four days. Transplants were then evaluated for proper healing. On day 7 after transplantation a dermal biopsy punch (2 mm diameter; Miltex Inc.) was used to create two full-thickness skin wounds in both transplants and the wound healing was monitored daily with the MAESTRO2 in vivo imager for 3 or 5 more days, when the skin transplants were harvested. Histological sections were cut at a right angle to the skin surface across the wound. Serial paraffin-embedded tissue sections (5 µm) were stained with hematoxylin and eosin (H&E).

Matrigel Angiogenesis Assay

Growth factor–depleted Matrigel (0.5 ml; BD Biosciences) was injected subcutaneously into three months old female mice. After seven days, the Matrigel plugs were harvested, and 5-µm sections of formalin-fixed, paraffin-embedded tissues were stained with hematoxylin and eosin (H&E). The sections were divided into five regions of the same size across the full diameter of each plug and in each region cell nuclei were counted in ten random fields (40x magnification). Regions 1 and 5 represent the edges of the plug and regions 2 to 4 the center.

Quantitative Real-Time PCR (qRT-PCR)

Total RNA from wounded tissues and bone marrow was extracted using the RNeasy fibrous mini kit and RNeasy mini kit (Qiagen), respectively, according to the manufacturer's instructions. cDNA was synthesized using the iScript cDNA synthesis kit (Bio-Rad Laboratories) according to the manufacturers' protocol. qRT-PCR was performed in a thermocycler (Eppendorf) using the iQ SYBR green supermix (Bio-Rad Laboratories) under the following conditions: 95°C for 3 minutes followed by 40 cycles (95°C for 20 seconds, 65°C for 30 seconds, and 72°C for 40 seconds using gene-specific primers listed in **Table S22**.

In Vivo Fluorescence Imaging

In vivo fluorescence imaging of GFP fluorescence of Aldara-treated skin, transplants and wounds was performed daily using a MAESTRO2 *in vivo* imaging system (CRI, PerkinElmer) with an excitation wavelength of 455 nm, and an emission detected between 500 and 720 nm). Spectral analysis of the images was conducted using the

Maestro software by unmixing the pure spectrum of a GFP solution from the autofluorescence of skin of wild type mice. The fluorescence signal of the skin was quantified and averaged.

Immunohistochemical analysis

Immunohistochemical analyses using antibodies against GFP (Invitrogen), mouse Krt13 (Abcam), Krt16 (LSbio), Colla1a2 (Abcam), phospho-FGFR1(Y653/654, Thermofisher), FGFR2 (Abcam), FGFR3 (Abcam), phosphor-FGFR3 (Y724, Biorbyt), FGFR4 (Sigma), CD31 (Abcam), BrdU (Roche), PCNA (Santa Cruz), Claudin1 (Abcam), and Filaggrin (Biolegend) were performed according to the manufacturer's instructions. PCNA-positive and BrdU nuclei were counted in at least 10 non-overlapping visual fields. Thickness was measured along 10 to 15 mm cross sections of hematoxylin/eosin stained dorsal skin. Approximately 20 high magnification pictures were taken and the epidermal thickness was measured at approximately 4 spots in each field. Keratinocyte layers were counted on at least 10 Claudin 1 stained tissue sections. For BrdU-based proliferation assay mice were injected intraperitoneal for 4 h prior to euthanasia (100 mg/kg).

Phenotype screen:

Open Field (OF)

The Open Field test was carried out according to the standardized phenotyping screens developed by the EUMORPHIA partners and available at http://www.empress.har.mrc.ac. The test apparatus from ActiMot, TSE was a square-shaped frame with two pairs of light-

beam strips, each pair consisting of one transmitter strip and one receiver strip. These basic light barrier strips were arranged at right angles to each other in the same plane to determine the X and Y coordinates of the animal, and thus its location (XY frame). Each strip was equipped with 16 infrared sensors with a distance between adjacent sensors of 28 mm. With two further pairs of uni-dimensional light-barrier strips (Z1 and Z2), rearing could be detected in addition to location. The light barriers were scanned with a frequency of 100 Hz each on fast computer platforms. Whenever an even number of light beams was interrupted, the center of gravity was calculated to lie between adjacent sensors. The test apparatus where the mouse was placed consisted of a transparent and infrared light permeable acrylic test arena (internal measurements: 45.5 x 45.5 x 39.5 cm) with a smooth floor. The illumination levels were set at approximately 150 lux in the corners and 200 lux in the middle of the test arena. At the beginning of the experiment, all animals were transported to the test room and left undisturbed for at least 30 minutes before the testing started. Then each animal was placed individually into the middle of one side of the arena facing the wall and allowed to explore it freely for 20 min. After each trial, the test arena was cleaned carefully with a disinfectant. For data analysis, the arena was divided by the computer in two areas, the periphery defined as a corridor of 8 cm width along the walls and the remaining area representing the center of the arena (42% of the total arena in our TSE-system). The following parameters were recorded: distance traveled, resting and permanence time as well as speed of movement for the whole arena, the periphery and the center. Additionally, rearing frequency, percentage distance traveled and percentage time spent in the center as well as the latency to first entry in center and center entry frequency were calculated. The time courses of distance

traveled, rearing frequencies as well as percentage distance traveled and percentage time spent in the center were additionally analyzed in 5-min-intervals.

Pre pulse inhibition (PPI)

PPI was assessed using a startle apparatus setup (Med Associates Inc., VT, USA) including four identical sound-attenuating cubicles. The protocols were written using the Med Associates ”Advanced Startle“ software. Experiments were carried out between 08:30h and 17:00h. Background noise was 65 dB, and startle pulses were bursts of white noise (40 msec). A session was initiated with a 5-min-acclimation period followed by five presentations of leader startle pulses (110 dB) that were excluded from statistical analysis. Trial types for the PPI included four different prepulse intensities (67, 69, 73, 81 dB); each prepulse preceded the startle pulse (110 dB) by a 50 msec inter-stimulus interval. Each trial type was presented 10 times in random order, organized in 10 blocks, each trial type occurring once per block. Inter-trial intervals varied from 20-30 sec. This protocol is based on the Eumorphia protocol (see www.eumorphia.org), adapted to the specifications of our startle equipment.

Modified SHIRPA protocol

The primary observation screen is a modification of the Irwin procedure (**Irwin, 1968**) and was proposed as a rapid, comprehensive and semi-quantitative screening method for qualitative analysis of abnormal phenotypes in a mouse strain (**Rogers et al., 1997**). We examined the mice using 23 designed test parameters (See webpage: http://www.har.mrc.ac.uk/services/phenotyping/neurology/shirpa.html) to detect

phenotypic differences between mutant and control mice. Each test parameter contributes to an overall assessment in muscle, lower motor neuron, spinocerebellar, sensory and autonomic function and is scored qualitatively after a defined rating scale. Assessment of each animal began with observation of undisturbed behavior (Viewing Jar Behavior) in a glass cylinder (11 cm in diameter). The mice were then transferred to an arena consisting of a clear Perspex box (420 x 260 x 180 mm) in which a Perspex sheet on the floor is marked with 15 squares. Locomotor activity and motor behavior within this area was observed (Behavior recorded in the Arena). This was followed by a sequence of manipulations testing reflexes (Behavior recorded on or above the arena). Measurements were completed with the recording of body weight. The last part of the primary screen also involved the analysis of contact righting reflex. Throughout the entire procedure, abnormal behavior, biting, defecation, and vocalization were recorded. Between testing of each mouse, fecal pellets and urination were removed from the viewing jar and arena. All experimental equipment was thoroughly cleaned with Pursept-A and dried prior to testing.

Grip strength

The grip strength meter system determines the grip strength of the limbs, i.e. muscle strength of a mouse. The device exploits the tendency of a mouse to grasp a horizontal metal grid while being pulled by its tail. During the trial set-up, the mouse grasps a special adjustable grid mounted on a force sensor. The mouse is allowed to catch the grid with either 2 or 4 paws. Three trials were undertaken for each mouse and measurement within one minute. The mean values are used to represent the grip strength of a mouse.

All experimental equipment was thoroughly cleaned with Pursept-A and dried prior subsequent tests. Grip strength trial results are compared between genotypes, controlling for the effects of sex and weight, by fitting linear models (**Pinheiro and Bates, 2000**). A linear model is a modified analysis of variance/covariance approach allowing for dependencies in the data. In our case, dependencies arise from repeated trials within each mouse. Genotype, sex and weight are modeled as fixed effects; Interaction effects are tested for and included in the model if they show a significant contribution. The p-value for the genotype effect within the specific model found for the data indicates the significance of the statistical test of interest

Rotarod test

The rotarod (Bioseb, Chaville, France) was used to measure fore limb and hind limb motor coordination, balance and motor learning ability (**Jones and Roberts, 1968).** The machine was set up in an environment with minimal stimuli such as noise and movement. The rotarod device is equipped with a computer controlled motor-driven rotating rod. The unit consists of a rotating spindle and five individual lanes for each mouse. Magnetic sensors are used to detect when a mouse falls from the rotarod. In general, the mouse is placed perpendicular to the axis of rotation, with head facing the direction of the rotation. All mice were placed on the Rotarod at an accelerating speed from 4 to 40 rpm for 300 sec with 15 min between each trial. In motor coordination testing, mice were given three trials at the accelerating speed at one day. The mean latency to fall off the Rotarod during the trials was recorded and used in subsequent analysis. In addition, the reason for the trial end (falling, jumping or rotating passively) is

recorded. Before the start of the first trial, mice were weighed. The Rotarod data contain dependencies, which are more complex than the grip strength data. Therefore a linear mixed-effects model is used. Repeated measurements arise from three different trials with a break in between. To compare the performance results between genotypes, linear mixed-effect models are fitted, that allow for the dependencies of genotype and trial and for the effects of sex and weight. The latter are modeled as fixed effects. Interaction effects are considered and included in the model, if necessary. In each model, the parameter of interest is the coefficient of the genotype effect. A significance test or a confidence interval for this coefficient can be extracted from the model fitted.

Auditory Brainstem Response (ABR)

Auditory brainstem response (ABR) is a type of auditory evoked potential and one of the key methods in non-invasive assessment of hearing sensitivity in mice. This physiological measurement represents the electrical potentials recorded at various levels of the auditory system in response to auditory stimulation (**Willott, 2001; Burkard et al., 2007**). The auditory stimulus generates a response from the hair cells of the cochlea and the signal travels along the auditory pathway. This response is recorded as a series of vertex positive waves which are generated by different auditory structures. In humans, ABR allows diagnosing of various otological, audiological, and neurological abnormalities and is a part universal newborn hearing screening. In mice, similar to humans, ABR is applied for evaluation of suspected retrocochlear pathology such as acoustic neuroma, vestibular schwannoma, and hearing sensitivity. The threshold, amplitude, and latency analysis of the ABR deliver information on the peripheral hearing

status and the integrity of brainstem pathways (**Burkard et al., 2007**).

In the primary analysis, the sound intensity thresholds are determined using different stimuli, either a broadband click or defined tone-bursts of distinct frequencies. More detailed analysis of the waveform characteristics is performed if appropriate. Mice anaesthetised with ketamine/xylazine are transferred onto a heating blanket in the acoustic chamber and tree subcutaneous needle electrodes are placed (**Ingham et al., 2011**). Since the stimuli are present as free-field sounds from a loudspeaker, the head of the mouse should be placed on the calibrated distance. This distance is determined by the calibration by white noise with the calibration microphone every day prior to measurements beginning.

For threshold determination, the clicks (0.01 ms duration) or tone pips (6, 12, 18, 24, and 30 kHz of 5 ms duration, 1 ms rise/fall time) stimuli over a range of intensity levels from 5-85 dB SPL in 5 dB steps produced by Tucker Davis Technologies hardware with customized software, kindly provided by Welcome Trust Sanger Institute, are used. The sound intensity threshold is chosen manually from the first appearance of the characteristic waveform. For quality control, this choice is re-checked routinely by an independent observer. For each mouse, once placed in the acoustic chamber for recording, the following procedure is used:

• Initial ABR test. A response to 70 dB click broadband stimuli is recorded to ensure correct setup.

• Determination of ABR hearing threshold. A series of click-evoked ABRs is recorded in response to broadband click stimuli ranging from 0 to 85 dB SPL in 5 dB intervals.

• Determination of tone-evoked ABR thresholds. Tone-evoked ABRs are recorded for a

set of frequencies (6, 12, 18, 24, and 30 kHz) over sound levels ranging from 0 to 85 dB SPL in 5 dB intervals.

• The recording of the response to 70 dB click broadband stimuli (1.) is repeated to ensure consistency of measurement.

For statistical analysis, a Wilcoxon Rank Sum test is used to analyze the thresholds of the different auditory stimuli. The audiograms normally show a characteristic pattern with higher thresholds in very low and very high frequencies. We evaluate a possible shift in this pattern using a linear mixed-effects-model with a random intercept and the frequency levels as a covariate into the analysis in addition to the effects of sex and genotype.

Hot plate test

The mice were placed on a metal surface maintained at 52 ± 0.2 C (Hot plate system was made by TSE GMBH, Germany; (**Eddy and Leimbach, 1953**). Locomotion of the mouse on the hot plate was constrained by 20 cm high Plexiglas wall to a circular area with a diameter of 28 cm. Mice remained on the plate until they performed one of three behaviors regarded as indicative of nociception: hind paw lick (h.p. licking), hind paw shake/flutter (h.p. shaking) or jumping. We evaluated only hind paw but not the front paw responses, because fore paw licking and lifting are components of normal grooming behavior. Each mouse was tested only once since repeated testing leads to profound changes in response latencies. The latency was recorded to the nearest 0.1 s. To avoid tissue injury 30 s cut-off time was used. The data values are given in seconds.

Statistical analyses were performed using R-scripts implemented in the database (MausDB). Differences between genotypes were analyzed with ANOVAs and Tuckey‘s

test for post hoc comparisons. Statistical significance was assumed at $p < 0.05$. Data are presented as mean values ± standard deviation.

Morphological Observation

The animals were screened using the protocol for morphological analysis from (**Fuchs et al., 2000**) as adapted for the German Mouse Clinic. Using a clickbox (supplied by the MRC Institute of Hearing Research, Nottingham, UK) we tested the mice's ability to hear a sound of 20 kHz. The reaction of the animals was classified into six categories (0=no reaction at all, 1=no Preyer reflex, 2= retarded reaction, 3= normal reaction, 4= strong reaction, 5=particularly strong reaction).

X-ray Images for Dysmorphology

Equipment: Faxitron X-ray Model MX-20 equipped with a DC-12 digital camera (Faxitron X-ray, Illinois, USA),

Quality control: Calibration of the system is done in monthly intervals,

Settings: Automatic exposure control (AEC) selects the appropriate exposure time and *kV settings for the specimen,*

Procedure: The anesthetized mouse was fixed on an X-ray-permeable plate and placed in the machine. Using DX software with ImageAssistTM supplied by the manufacturer, the image was taken and analyzed. Analysis was done qualitatively by visual inspection of the images as well as quantitatively by using the ruler tool of DX software.

Bone density analysis

Equipment: pDEXA Sabre X-ray Bone Densitometer (Norland Medical Systems. Inc., Basingstoke, Hampshire, UK; distributed by Stratec Medizintechnik GmbH, Pforzheim, Germany),

Quality control: Calibration of the system was done in daily intervals using the QC and the QA phantoms delivered by the manufacturer. Results from the quality control were recorded by the system.

Settings: Scan speed 20 mm/s, Resolution 0.5 mm x 1.0 mm, HAW 0.020

Procedure: After anesthesia, the weight and length of the mouse were recorded, and the mouse was placed in the analyzer. After a scout scan, the area of interest was optimized and the measure scan started.

Data-analysis: The whole body excluding the skull was analyzed.

Indirect calorimetry

High precision CO_2 and O_2 sensors measure the difference in CO_2 and O_2 concentrations in air volumes flowing through control or animal cages. The amount of oxygen consumed over a given period of time can be calculated with air flow through the cage measured in parallel. Data for oxygen consumption are expressed as ml O_2/h/animal. The system also monitors CO_2 production; therefore, the respiratory exchange ratio (RER) and heat production can be calculated.

The RER is calculated as the ratio VCO_2/VO_2.

Heat production (HP) is calculated from VO_2 and RER using the formula:

$HP[mW] = (4.44 + 1.43 * RER) * VO_2$ [ml / h]

The test is performed at regular room temperature (23 C) with a 12:12 hrs light/dark

cycle in the room (lights on 06:00 CET, lights off 18:00 CET). Paper tissue is provided as bedding material. Each mouse is placed individually in the chamber for a period of 21 hours (from 13:00 CET to 10:00 CET next day) with free access to food and water. Metabolic cuvettes are set up in a ventilated cabinet continuously supplied with an overflow of fresh air from outside.

In addition, body mass before and after gas exchange measurements are taken. Before returning the mice to their home, cage rectal body temperature is also determined. Food intake is monitored by continuously weighing food hoppers that are attached to electronic scales. Thereby, total daily food intake as well as meal size and meal duration can be determined in case genotype effects on food intake could be detected. Physical activity is measured by infrared light beam frames set up around the cages. This system allows the measurement of distance travelled and the number of rearings per time interval.

Determination of Body Composition

Most energy metabolism parameters are related to body mass and body composition. For the accurate evaluation of energy expenditure it is, therefore, of advantage to gain precise knowledge about body composition in addition to gas exchange data. Our whole body composition analyzer (Bruker MiniSpec) based on Time Domain Nuclear Magnetic Resonance (TD-NMR) provides a precise method for the measurement of lean tissue and body fat in live mice without anaesthesia. It uses TD-NMR signals from all protons in the entire sample volume and can provide data on lean and fat mass. Statistical analyses were performed using R-scripts implemented in the database (MausDB). Differences between genotypes were evaluated by Linear Models. Statistical significance was assumed at $p <$

0.05. Data are presented as mean values ± standard deviation.

Echocardiography

Left ventricular function was evaluated with transthoracic echocardiography using a Vevo 2100 Imaging System (Visual Sonics) with a 30MHz probe. The echocardiographer was blinded with respect to the genotype. In order to avoid anesthetic-related impairment of cardiac function during echocardiography (**Roth et al., 2002**), examinations were performed on conscious animals (**Schoensiegel et al., 2011**). Left ventricular parasternal short and long-axis views were obtained in B-mode imaging and left ventricular parasternal short-axis views were obtained in M-mode imaging at the papillary muscle level. The short axis M-mode images were used to measure left ventricular end-diastolic internal diameter (LVEDD), left ventricular end-systolic internal diameter (LVESD), diastolic and systolic septal wall thickness (IVS) and diastolic and systolic posterior wall thickness (LVPW) in three consecutive beats according to the American Society of Echocardiography leading edge method (**Sahn et al., 1978**). Fractional shortening (FS) was calculated as FS%=[(LVEDD-LVESD)/LVEDD]x100. Ejection fraction (EF) was calculated as EF%=100*((LVvolD-LVvolS)LVvolD) with LVvol=((7.0/(2.4+LVID)*LVID^3). The corrected left ventricular mass (LV MassCor) was calculated as LV MassCor=0.8 (1.053 * ((LVIDD + LVPWD + IVSD)^3 - LVIDD^3)). The Stroke volume (SV) is the volume of blood pumped from one ventricle of the heart with each beat. The Stroke volume of the left ventricle was obtained by substracting end-systolic volume (ESV) from end-diastolic volume (EDV). In addition, heart rate and respiratory rate were calculated by measuring three systolic intervals, respectively three

respiratory intervals.

Electrocardiography

ECG´s were recorded in conscious mice with the ECGenie (Mouse Specificy Inc., Boston, MA) and analysed using e-Mouse software (Mouse Specifics Inc.) The cardiac electrical activity was detected non-invasively through the animals´ paws. The size and arrangement of the electrodes are configured to advance contact with three of the animals' paws to provide an ECG signal that is equivalent to Einthoven lead II. For each animal, intervals and amplitudes were evaluated from continuous recordings of at least 15 ECG signals. e-MOUSE software uses peak detection to calculate the heart rate (HR). HR variability (HRV) is calculated as the mean of the differences between sequential HRs. The software plots its interpretation of P, Q, R, S, and T for each beat so that unfiltered noise or motion artifacts are rejected. This is followed by calculations of the mean of the ECG time intervals for each set of waveforms. The corrected QT interval (QTc) is calculated by dividing the QT interval by the square root of the preceeding RR interval. QT dispersion was measured as inter-lead variability of QT intervals. The QTc dispersion was calculated as the rate corrected QT dispersion.

Heart Weight Determination

During the final examination in the Pathology Screen the heart weight was determined together with body weight and tibia length. Briefly, mice were sacrificed by CO2 inhalation, weighed and opened from the ventral midline. Exsanguination was achieved by cutting the dorsal aorta. Prior to dissection the heart was inspected for abnormalities or

excessive fat. For excision the heart was removed from the pericardial membrane and the major vessels were cut through at the point they enter or exit the atria. The heart weight was obtained wet after blotting the organ on paper towels. The tibia length was determined from the left tibia of the mouse using a digital caliper "MarCal" (Mahr GmbH; Göttingen, Germany). The data were analyzed statistically with R-scripts. Wilcoxon rank sum tests for the detection of genotype effects were performed for all animals together and for each sex separately.

Eye Screen

For Laser Interference Biometry and Optical Coherence Tomography, mice were anaesthetized with 137 mg Ketamine and 6.6 mg Xylazine per kg body weight. Eyes were further treated with 1% Atropine to ensure pupil dilation. When the mice were killed for pathological examinations, the eyes of some mice were fixed for histological analysis in the eye screen.

Laser Interference Biometry (LIB)

Eye size measurement was performed using the "AC Master" (Meditec, Carl Zeiss, Jena, Germany). Briefly, anaesthetized mice were placed on a platform and orientated in an appropriate position using light signals from six infrared LEDs arranged in a circle that must be placed in the center of the pupil. Central measurements of axial eye length were performed essentially as described (**Schmucker and Schaeffel, 2004**).

Optical Coherence Tomography

Eye fundus and retina were analyzed with a Spectralis OCT (Heidelberg Engineering, Heidelberg, Germany) modified with a 78 diopter double aspheric lens (Volk Optical, Inc., Mentor, OH, USA) that is fixed directly to the outlet of the device. To the eye of the mouse, a contact lens with a focal length of 10 mm (Roland Consult, Brandenburg, Germany) was applied with a drop of methyl cellulose (Methocel 2%, OmniVision, Puchheim, Germany). For measurements, anaesthetized mice were placed on a platform in front of the Spectralis OCT such that the eye is directly facing the lens of the recording unit. Images were taken as described previously (**Fischer et al., 2009**). Retinal thickness was calculated with the provided thickness profile tool.

Scheimpflug Imaging

Images of corneas and lenses were taken with the Pentacam digital camera system (Oculus GmbH,Wetzlar, Germany). Mice were hold on a platform such that the vertical light slit (light source: LEDs, 475 nm) was orientated in the middle of the eye ball. Distance between eye and camera was fine adjusted with the help of the provided software in order to guarantee optimal focus. Subsequently, measurements were started manually. Mean density across the lens was quantified with the provided densitometry tool.

Virtual vision test

Vision tests were performed between 9 am and 4 pm using a virtual optomotor system (Cerebral Mechanics, Lethbridge, Canada) as described previously (**Prusky et al., 2004**). Briefly, a rotating cylinder covered with a vertical sine wave grating was calculated and

drawn in virtual three-dimensional space on four computer monitors facing to form a square. Visually unimpaired mice track the grating with reflexive head and neck movements (head-tracking). Vision threshold of the tested mice was quantified by a randomized simple staircase test. Rotation speed and contrast were set to 12.0 d/s and 100%, respectively. Medians, first and third quartile, and p-values were calculated by a Wilcoxon rank-sum test. Statistical significance was set at $p < 0.05$.

Intraperitoneal Glucose-Tolerance-Test

Mice were used for the glucose tolerance test after a 16-18 hours-lasting overnight food-withdrawal. In the beginning of the test, the body weight of mice was determined. For the determination of the fasting blood glucose level, the tip of the tail was scored using a sterilized scalpel blade and a small drop of blood was analyzed with the Accu-Chek Aviva glucose analyzer (Roche/Mannheim). Thereafter mice were injected intraperitoneally with 2 g of glucose/kg body weight using a 20 % glucose solution, a 25-gauge needle and a 1-ml syringe. 15, 30, 60 and 120 minutes after glucose injection, additional blood samples (one drop each) were collected and used to determine blood glucose levels as described before. Repeated bleeding was induced by removing the clot from the first incision and massaging the tail of the mouse. After the experiment was finished, mice were placed in a cage with plentiful supply of water and food.

Blood Withdrawal and Storage

Blood samples were taken from isoflurane-anesthetized mice by puncturing the retro-bulbar sinus with non-heparinized glass capillaries (1.0 mm in diameter; Neolab; Munich,

Germany). The time of sample collection was recorded in a work list. Blood taken after overnight food-withdrawal was collected in heparinized sample tubes (Li-heparin, KABE; Nümbrecht, Germany; Art.No. 078028), blood sample collected from ad libitum fed mice were divided into two portions. The major portion was collected in a heparinized tube (Li-heparin, KABE; Nümbrecht, Germany; Art.No. 078028). The smaller portion was collected (using the same capillary) in an EDTA-coated tube (KABE, Art.No 078035) and each tube was immediately inverted five times to achieve a homogeneous distribution of the anticoagulant. Samples collected from unfed mice were stored in a rack on ice, separated by centrifugation (10 min, 5000 ´ g; 8 C, Biofuge fresco, Heraeus; Hanau, Germany) as soon as possible and plasma was used for clinical-chemical analysis. Heparinized blood collected from ad libitum fed mice was left in a rack at room temperature for one to two hours. Afterwards, cells and plasma were separated by a centrifugation step (10 min, 5000 ´ g; 8 °C, Biofuge fresco, Heraeus; Hanau, Germany). Plasma was distributed between the Immunology Screen (30 ml), the Allergy Screen (30 ml), the Clinical Chemical Screen (110 ml) and the Steroid Screen (50 ml), while the cell pellet was given to the Immunology Screen for FACS-analysis. The plasma samples for the clinical chemical analyses were transferred into Eppendorf tubes and either used immediately (plasma of unfed mice) or diluted 1:2 with aqua dest. (ad libitum fed mice). The solution was mixed for a few seconds (Vortex genie, Scientific Industries; New York, USA) to prevent clotting and then centrifuged again for 10 min at 5000 x g at 8 °C. In addition, the Clinical Chemical Screen received the EDTA-blood samples for hematological investigations, which were placed on a rotary agitator at room temperature until analysis.

Clinical Chemistry

The screen was performed using a Beckman-Coulter AU 480 autoanalyzer and adapted reagents from Beckman-Coulter (Krefeld, Germany), except free fatty acids (NEFA) that were measured using a kit from Wako Chemicals GmbH (NEFA-HR2, Wako Chemicals, Neuss, Germany) and Glycerol, which was measured using a kit from Randox Laboratories GmbH (Krefeld, Germany) as described before **(Rathkolb et al. 2013b)**. In the primary screen, a broad set of parameters was measured including various enzyme activities, as well as plasma concentrations of specfic substrates and electrolytes in ad libitum fed mice. A set of six measured parameters and one calculated value (blood lipid and glucose levels) was determined in samples derived from mice after overnight food withdrawal.

Hematology

For hematological assessment, 50 µl EDTA-blood were diluted 1:5 with cell-pack buffer using Sysmex capillary tubes and analyzed with a Sysmex XT2000iV hematology analyzer (Sysmex Deutschland GmbH, Bornbach, Germany) as described before **(Rathkolb et al. 2013a)**.

To determine number and size of red blood cells, white blood cells, and platelets, mean corpuscular volume (MCV), mean platelet volume (MPV) and red blood cell distribution width (RDW) are calculated directly from the cell volume measurements. The hematocrit (HCT) is assessed by multiplying the MCV with the red blood cell count. Mean corpuscular hemoglobin (MCH) and mean corpuscular hemoglobin concentrations

(MCHC) are calculated from hemoglobin/ red blood cells count (MCH) and hemoglobin/ hematocrit (MCHC), respectively.

Additional sample for a second measurement was collected four weeks after the first sample collection without fasting from a subgroup of mice (usually 10 per sex and genotype). Data were statistically analyzed using R-Scripts. Depending on the distribution of the respective data parametric or non-parametric statistical methods are used.

Immunology Screen: Peripheral blood leukocytes (PBLs)

PBLs were isolated from the cell pellet of 500ml whole blood samples after centrifugation. The cell pellet is dissolved in 600 ml NH4Cl-based, Tris-buffered erythrocyte lysis solution, and 150ml transferred into 96-well micro titer plates. After subsequent washing steps with FACS staining buffer (PBS, 0.5%BSA, 0.02%sodium azide, pH 7.45), PBLs were incubated for 20 min with Fc block (clone 2.4G2, PharMingen, San Diego, USA). Cells were then stained with fluorescence-conjugated monoclonal antibodies (PharMingen). After the antibody incubation, propidium iodide was added for the identification of dying/dead cells (**Zamai et al., 1996**), which might bind antibodies unspecifically, and/or loose specific antigens upon apoptosis (Diaz et al., 2004).

Samples were acquired from 96 well plates and measured in one of our two three laser 10-color flow cytometers (LSRII, Becton Dickinson, USA; Gallios, Beckman Coulter, USA). A total number of 10.000- 30.000 living CD45+ per sample is reached. For analysis, intact cells are first identified by their FSC/SSC profile. These cells were gated

on the basis of their propidium iodide/PE signal (compensated parameters), allowing the dead cells to be gated out. Living cells were then gated using their SSC/CD45 signal, gating out remaining erythrocytes, thrombocytes and debris (Weaver et al., 2002). CD45+ cells are subsequently analyzed by software based analysis (Flowjo, TreeStar Inc, USA; SPICE (**Roederer et al., 2011**)). In former experiments, FMO (Fluorescence minus one) controls from wild-type mice have been used to define 'positive' and 'negative' regions (**Baumgarth and Roederer, 2000**).

Immunoglobulins

The plasma levels of IgM, IgG1, IgG2a, IgG2b, IgG3, and IgA were determined simultaneously in the same sample using a bead-based assay (Fulton et al., 1997) with monoclonal anti-mouse antibodies conjugated to beads of different regions (Biorad, USA), and acquired on a Bioplex reader (Biorad). The presence of rheumatoid factor and anti-DNA antibodies was evaluated by indirect ELISA with rabbit IgG (Sigma-Aldrich, Steinheim, Germany) and calf thymus DNA (Sigma-Aldrich), respectively, as antigens and AP-conjugated goat anti-mouse secondary antibody (Sigma-Aldrich). Serum samples from MRL/MpJ-Tnfrsf6lpr mice (Jackson Laboratory, Bar Harbor, USA) were used as positive controls in the autoantibody assays.

IgE ELISA

Plasma was analyzed for total IgE, using a classical immunoassay isotype-specific sandwich ELISA. In brief, microtiter plates (96-well) were coated with 10 mg/ml anti mouse-IgE rat monoclonal IgG (clone-PC284, The Binding Site) to detect total IgE.

Serum samples were diluted 1:10 and standards for murine IgE (Mouse IgE, k clone C38-2 BD Pharmingen) were appropriately diluted. As secondary antibodies, biotinylated rat anti-mouse IgE (clone R35-118, BD Pharmingen) were used followed by incubation with BD OptEIA Reagent Set B (Cat. No. 550534 BD Pharmingen) Plates were analyzed using a standard micro well ELISA reader at 450 nm. Total murine IgE data are reported in ng/ml, based on a standard curve of purified murine IgE (**Alessandrini et al., 2001**).

Molecular Phenotyping

The molecular phenotyping screen archives organs of mutant and control mice for subsequent DNA-chip expression profiling analysis. Usually eight male mice (four mutants and four controls) were provided to the molecular phenotyping screen. To minimize the influence of circadian rhythm on gene expression, mice were killed between 9 and 12 am by carbon dioxide asphyxiation. The listed organs were collected and archived in liquid nitrogen following our established SOPS: spleen, kidney, liver, heart, thymus, skeletal muscle, pancreas and brain. Organs were immediately frozen and stored in liquid nitrogen until isolation of total RNA. Pancreas was stored at 4°C in RNAlater buffer (Qiagen) for 1-2 days. Afterwards the tissue was removed from the buffer and stored at -80°C. Organ samples collected in this collaboration may either be used for expression profiling analysis in the GMC or on request send to the collaboration partner. The storage time for the organs is limited to approximately 3-4 years

RNA isolation

Total RNA was isolated just before processing the microarray experiment. For

preparation of total RNA individual organs were thawed in 4 ml Trizol Reagents (Sigma) and homogenized using a Polytron homogenizer (Heidolph). Total RNA from individual samples were obtained from a 1 ml aliquot of the homogenate according to manufacturer's protocol using RNeasy Mini Kits (Qiagen). Another 2 ml homogenate was stored at -80°C as backup. 2 mg RNA aliquots were run on a formaldehyde agarose gel to check for RNA integrity. The concentration was measured by a Nanodrop device. The RNA was stored at -80°C. The storage time for the RNA is limited to approximately 2-3 years.

Illumina Bead Arrays

For each selected organ one Illumina Bead Array enabling the performance of eight samples in parallel, was processed. Usually, four biological replicates for each genotype group were performed. Therefore, 500 ng of total RNA was amplified in a single round with the Illumina TotalPrep RNA Amplification Kit (Ambion). 750 ng of amplified RNA was hybridized on Illumina MouseRef8 v2.0 Expression Bead Chips containing about 25K probes (25.600 well-annotated Ref-Seq transcripts). Staining and scanning (Illumina HiScan Array reader) was done according to the Illumina expression protocol.

Illumina Genomestudio 2011.1 software was used for background correction and normalization of the data (cubic spline). The remaining negative expression values were corrected by introducing an offset. The identification of significant gene regulation was performed using SAM (Significant Analysis of Microarrays) included the TM4 software package (**Horsch et al., 2008; Saeed et al., 2003; Tusher et al., 2001**). Genes were ranked according to their relative difference value d(i), a score assigned to each gene on

the basis of changes in gene expression levels relative to the standard deviation. Genes with d(i) values greater than a threshold were selected as significantly differentially expressed in an one class analysis. The percentage of such genes identified by chance is the false discovery rate (FDR). To estimate the FDR, nonsense genes were identified by calculation 1000 permutations of the measurements. The selection of the top differentially expressed genes with reproducible up- or down-regulation includes less than 10% false positives (FDR < 10) in combination with fold change > 1.4.

Macroscopial and histological analyses

Mice received in the laboratory of pathology were sacrificed with CO2. The animals were analyzed macroscopically and weighed. The thymus and left lobe of the liver were measured with a digital caliper (MarCal Mahr GmbH; Göttingen, Germany). Blood samples were taken, centrifuged and the serum was saved at -20 C. Tails were preserved at -70 C for further genetic analysis. Following a complete dissection, an x-ray of the complete bone structure was taken, when indicated (Hewlett Packard, Cabinet X-Ray System Faxitron Series). All organs were fixed in 4 % buffered formalin and embedded in paraffin for histological examination. Two-mm-thick sections from skin, heart, muscle, lung, brain, cerebellum, thymus, spleen, cervical lymph nodes, thyroid, parathyroid, adrenal gland, stomach, intestine, liver, pancreas, kidney, reproductive organs, and urinary bladder were cut and stained with hematoxylin and eosin (H&E).

References:

Alessandrini, F., Jakob, T.,Wolf, A.,Wolf, E., Balling, R., Hrabe de Angelis, M., et al. ENU mouse mutagenesis: generation of mouse mutants with aberrant plasma IgE levels. Int Arch Allergy Immunol 2001;124(1-3):25–8.

Baumgarth, N. Roederer, M. A practical approach to multicolor flow cytometry for immunophenotyping. J Immunol Methods 2000;243(1-2):77–97.

Burkard, R. F., Don, M., Eggermont, J. J. Auditory Evoked Potentials, Lippincott Williams and Wilkins, Philadelphia; 2007.

Eddy, N. B. Leimbach, D. Synthetic analgesics. II. dithienylbutenyl- and dithienylbutylamines. J Pharmacol Exp Ther 1953;107(3):385–93.

Fischer, M. D., Huber, G., Beck, S. C., Tanimoto, N., Muehlfriedel, R., Fahl, E., et al. Noninvasive, in vivo assessment of mouse retinal structure using optical coherence tomography. PLoS ONE 2009;4(10):7507.

Fuchs, H., Schughart, K., Wolf, E., Balling, R., Hrabe de Angelis, M. Screening for dysmorphological abnormalities–a powerful tool to isolate new mouse mutants. Mamm Genome 2000;11(7):528–30.

Ingham, N. J., Pearson, S., Steel, K. P. Using the Auditory Brainstem Response (ABR) to determine sensitivity of hearing in mutant mice. Current Protocols in Mouse Biology 2011;1:279–287.

Irwin, S. Comprehensive observational assessment: Ia. A systematic, quantitative procedure for assessing the behavioral and physiologic state of the mouse. Psychopharmacologia 1968;13(3):222–57.

Jones, B. Roberts, D. The quantitative measurement of motor incoordination in naive mice using an accelerating Rota-Rod. J Pharm Pharmacol 1968;20:302–304.

Horsch, M., Schädler, S., Gailus-Durner, V., Fuchs, H., Meyer, H., Hrabe de Angelis, M., et al. Systematic gene expression profiling of mouse model series reveals coexpressed genes. Proteomics 2008;8(6):1248–56.

Pinheiro, J. Bates, D. Mixed-Effect Models in S and S-PLUS, Springer, New York; 2000.

Prusky, G. T., Alam, N. M., Beekman, S., Douglas, R. M. Rapid quantification of adult and developing mouse spatial vision using a virtual optomotor system. Invest Ophthalmol Vis Sci 2004;45(12):4611–4616.

Rathkolb B, Fuchs H, Gailus-Durner V, Aigner B, Wolf E, Hrabě de Angelis M. Blood Collection from Mice and Hematological Analyses on Mouse Blood. Curr Protoc Mouse Biol 2013;3(2):101–19

Rathkolb B, Hans W, Prehn C, Fuchs H, Gailus-Durner V, Aigner B, et al. Clinical Chemistry and Other Laboratory Tests on Mouse Plasma or Serum. Curr Protoc Mouse Biol 2013;3(2):69–100

Roederer, M., Nozzi, J. L., Nason, M. X. SPICE: Exploration and analysis of post-cytometric complex multivariate datasets. Cytometry A 2011;79(2):167–74.

Rogers, D. C., Fisher, E. M., Brown, S. D., Peters, J., Hunter, A. J., Martin, J. E. Behavioral and functional analysis of mouse phenotype: SHIRPA, a proposed protocol for comprehensive phenotype assessment. Mamm Genome 1997;8(10):711–3.

Roth, D. M., Swaney, J. S., Dalton, N. D., Gilpin, E. A., Ross, J. Impact of anesthesia on cardiac function during echocardiography in mice. Am J Physiol Heart Circ Physiol 2002;282(6):H2134–H2140.

Saeed, A. I., Sharov, V., White, J., Li, J., Liang,W., Bhagabati, N., Braisted, J., et al. TM4: a free, open-source system for microarray data management and analysis. Biotechniques 2003;34(2):374–8.

Sahn, D. J., DeMaria, A., Kisslo, J., Weyman, A. Recommendations regarding quantitation in M-mode echocardiography: results of a survey of echocardiographic measurements. Circulation 1978;58(6):1072–83.

Schmucker, C. Schaeffel, F. In vivo biometry in the mouse eye with low coherence interferometry. Vision Res 2004;44(21):2445–56.

Schoensiegel, F., Ivandic, B., Geis, N. A., Schrewe, A., Katus, H. A., Bekeredjian, R. High throughput echocardiography in conscious mice: training and primary screens. Ultraschall Med 2011;32 Suppl 1:S124–S129.

Tusher, V. G., Tibshirani, R., Chu, G. Significance analysis of microarrays applied to the ionizing radiation response. Proc Natl Acad Sci U S A 2001;98(9):5116–21.

Willott, J. F., ed. In: Handbook of Mouse Auditory Research. From Behaviour to molecular Biology, CRS Press, Boca Raton; 2001.

Zamai, L., Falcieri, E., Marhefka, G., Vitale, M. Supravital exposure to propidium iodide identifies apoptotic cells in the absence of nucleosomal dna fragmentation. Cytometry 1996;23(4):303–11.

Legends to Supplemental Figures:

Supplemental Figure S1. (a) Epidermal thickness of juvenile skin at 3 weeks of age (WT n=4, KO n=5). (**b**) RNA expression in epidermis and dermis (WT n=4, KO n=3)

Supplemental Figure S2. **Ingenuity Pathway Analysis of mRNA expression.** Canonical pathway analysis for (**a**) untreated KO skin compared to untreated WT skin, (**b**) DMBA/TPA (D/T) treated WT papilloma compared to untreated WT skin, (**c**) DMBA/TPA treated KO papilloma compared to untreated WT skin. Upstream regulators (**d**) DMBA/TPA treated WT papilloma compared to untreated WT skin, (**e**) DMBA/TPA treated KO papilloma compared to untreated WT skin. (WT $n_{=}4$, KO $n_{=}3$)

Supplemental Figure S3. Fgfbp1 is upregulated in psoriatic lesions and in squamous cell carcinoma in skin. Analysis of gene expression omnibus datasets (GEO). (**a**) Psoriasis (GDS41602, "normal" n=64, "no lesion" n=58, "with lesion" n=58). (**b**) Skin from healthy subjects and patients with psoriasis (GDS2518, n=13). (**c**) Skin from healthy subjects and patients with actinic keratosis (AK) or invasive cutaneous squamous cell carcinoma (SCC) (GDS2200, "normal" n=6, AK n=4, SCC n=5).

Supplemental Figure S4. FGFR isoform expression in Aldara treated skin. (**a**) RNA expression measured by qRT-PCR. (**b**) Ratio of FGFR isoform expression. WT $n_{=}4$, KO $n_{=}5$

Supplemental Figure S5. Immunohistochemical analysis of Aldara treated skin. Representative images of tissue sections of skin from untreated and Aldara treated WT and KO mice stained with antibodies against Krt16, phospho-Fgfr1, Fgfr2, phospho-Fgfr3, Fgfr3 and Fgfr4 (scale bar=100 µm).

Supplemental Figure S6. Immunohistochemical analysis of DMBA/TPA treated skin. (**a**) Papilloma tissue section stained with anti-GFP antibody, magnified image of Fig. 4c (dermis=D, epidermis=E, scale bar=100 µm), (**b**) Representative images of tissue sections of skin from untreated and DMBA/TPA treated WT and KO mice stained with antibodies against Krt16, phospho-Fgfr1, Fgfr2, phospho-Fgfr3, Fgfr3 and Fgfr4 (scale bar=100 µm), (**c**) Proliferation index of keratinocytes in papilloma of WT and KO mice quantified by counting BrdU positive nuclei, (WT $n=4$, KO $n=3$)

Supplemental Figure S7. Incidence of ulcers and expression of isoforms of Fgfr in DMBA/TPA-treated skin. (**a**) Kaplan-Mayer plot of the incidence of ulcers in DMBA/TPA treated mice. (n=9, Wilcoxon Test). (**b**) Fgfr isoform expression detected by qRT-PCR. (**c**) Fgfr isoform ratios (WT $n=4$, KO $n=3$). (**d**) Representative in-situ hybridization (ISH) of tissue sections. (WT $n=4$, KO $n=3$). (**e**) representative image of papilloma with sense control probe for Fgfr1 IIIb and Fgfr1 IIIc ISH

Supplemental Figure S8. Illumina bead assay RNA expression levels in DMBA/TPA treated skin. The most selectively expressed genes relative to WT control are shown sorted by function/location (WT $n=4$, KO $n=3$).

Supplemental Figure S9. Analysis of wound healing tissues. (**a**) Representative skin tissue section stained with anti GFP antibody proximal and distal to wounds. (**b**) Granulation tissue section stained with anti-GFP antibody (magnification of **Fig. 5e**, scale bar=100 µm). (**c**) H&E stained wound section (scale bar=1 mm). The magnified sections show extravasated red blood cells (eR), single red blood cells (arrow heads; scale bar=100 µm), granulation tissue (G), Fat (F), Scab (S), dermis (D), muscle (M), Hair follicles/glands (H), epidermis (E) (magnification of **Fig. 5f**). (**d**) Quantification of the number of cells in the granulation tissue (Student's t test, WT n=5, KO n=6, at least 10 fields counted for each wound). (**e**) Representative images for the quantification of cell proliferation in granulation tissues. (**f**) PCNA stained nuclei were counted.

Supplemental Figure S10, Wound healing of Fgfbp1+/^{gfp} mouse skin transplanted onto WT recipient. (**a, b**) Skin from a Fgfbp1+/^{gfp} mouse was transplanted onto the back of a WT mouse, wounded after 7 days and fluorescence was monitored for 3 days. (**c**) Left panels: Bright field images and GFP fluorescence of wounded skin transplant at different times after wounding. Right panels: Immunostaining of representative tissue sections on day 3 post wounding with anti-GFP antibody. No staining of inflammatory cells was detectable (top panel). The border between donor skin transplant and host skin showed GFP-positive epidermal staining in the donor skin (bottom panel). (**d**) Quantification of GFP signal in the wound and transplant. No significant increase in signals were detected over time. (2-way Anova, n=7). (**e**) Representative wound tissue section from WT mice that received bone marrow cell transplants from a Fgfbp1+/^{gfp}

mouse. Anti-GFP antibody stain; magnification of **Fig. 6e**. Scale bar left panel=500 μm; right panel=100 μm. (**f**) Matrigel plug neoangiogenesis assay. Representative tissue section from Fgfbp1+/^{gfp} mice stained with anti-GFP antibody (scale bar = 100 μm)

Supplemental Figure S11. Fgfbp1-KO mice show a significant increase in fat mass with decreased VO2 and food intake. (**a**) total body mass. (**b, c**) Body composition by Time Domain Nuclear Magnetic Resonance (TDNMR); (**b**) fat mass; (**c**) lean mass. (**d**) lean mass detection by Dual energy X-ray Absorptiometry (DXA). (**e**) Indirect calorimetry oxygen consumption and (**f**) food intake. (**g**) Locomotor activity and (**h**) respiratory exchange ratio (RER). Mean, standard deviation and p-values.

Supplemental Figure S12. Heart and Spleen weights altered in female Fgfbp1-KO mice. (**a**, **b**, **c**) Heart weight was significantly higher in female KO mice when normalized to body weight (**h**). (**d, e, f**) The spleen weight was lower in female KO mice both absolute and when normalized to tibia length (**g**). p-values from Wilcoxon rank-sum test.

Supplemental Figure S13. Clinical chemistry analysis: Differences between Fgfbp1-KO and WT mice. (a to **d**)16 week old mice. (**a**) Blood glucose after fasting; (**b**) cholesterol; (**c**) total iron binding capacity (TIBC); (**d**) lactate. (**e, f**) 22 week old mice. (**e**) cholesterol; (**f**) urea. Means, standard deviation and p-values.

Supplemental Figure S14. Plasma immunoglobulins and leukocyte populations. Plasma analysis of (**a**) IgM, (**b**) IgG2b, (**c**) IgG3, (**d**) IgE. (**e, f**) Leukocyte subpopulation. (**e**) CD45 subsets, (**f**) monocyte subsets. p-values from a Wilcoxon rank-sum test.

Supplemental Figure S15. Behavioral experiments. (**a, b**) Rotarod test. (**a**) falling frequency (Fisher's exact test), (**b**) latency to fall (mean, standard deviation). (**c** to **h**) Open field tests. (**c**) distance covered, (**d**) time in center (**e, f**) distance covered relative (e) and absolute (f), (**g**) number of entries into the center, (**h**) number of rears in the last 5 min of the test. Means, standard deviation and p-values.

Supplemental Figure S16. Auditory brain response (ABR) threshold. (**a**) Click-evoked response threshold. Tone-evoked thresholds at (**b**) 6 kHz, (**c**) 12 kHz, (**d**) 18 kHz, (**e**) 24 kHz and (**f**) 30 kHz. Means, standard deviation and p-values were calculated by a Wilcoxon rank-sum test. Values above measurement limit (85db) were replaced by 100.

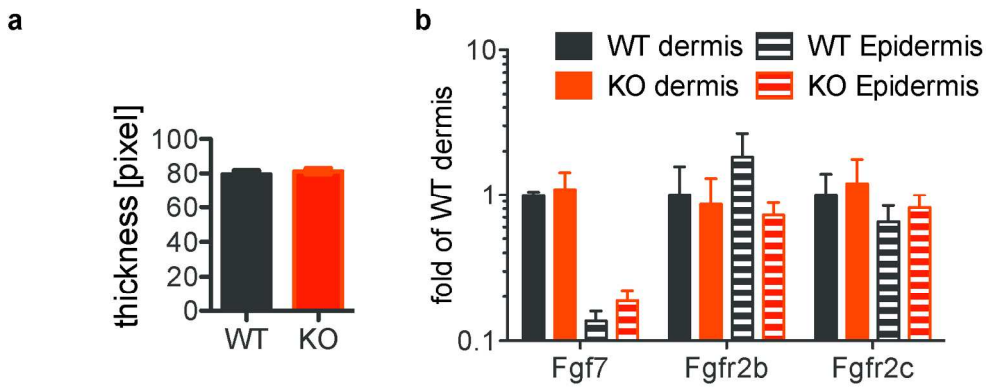

Schmidt et al., Suppl. Fig. S1

173x100mm (300 x 300 DPI)

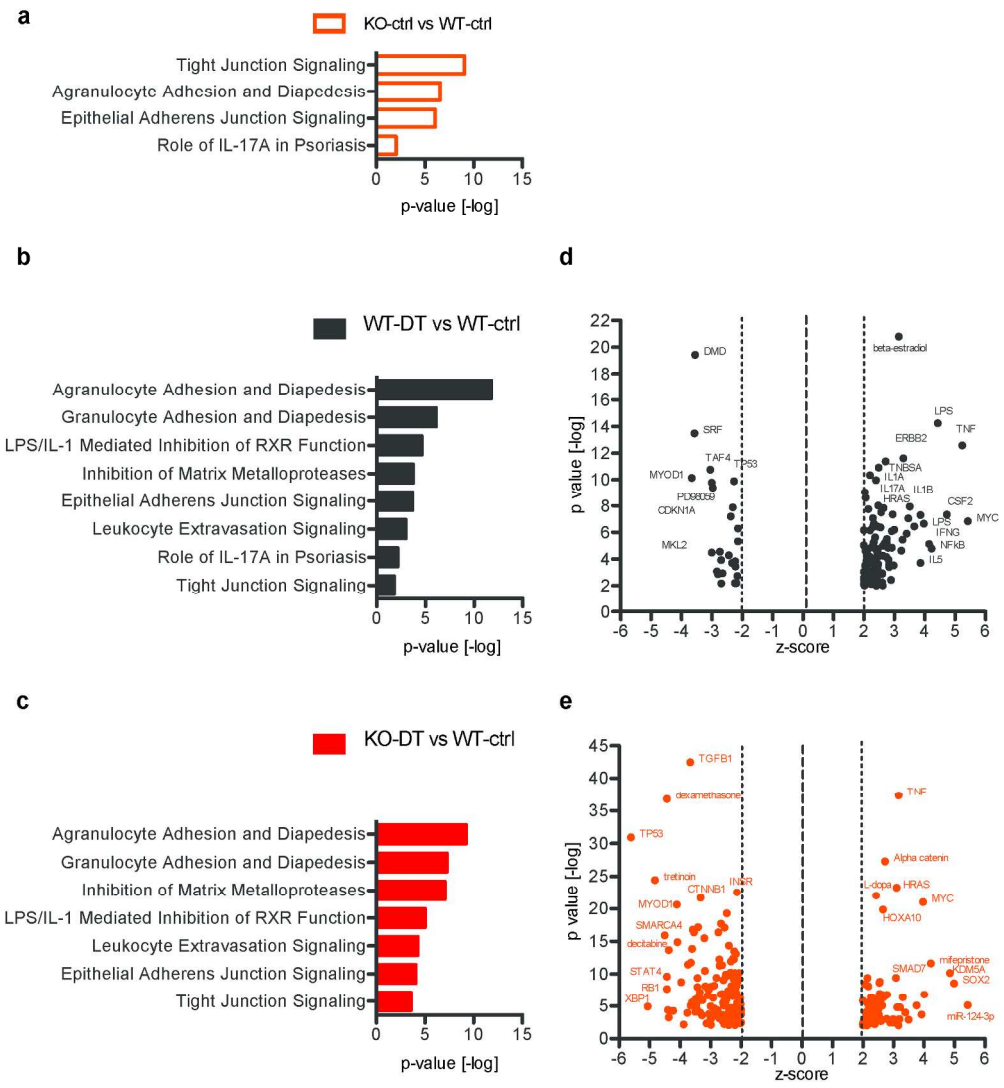

Schmidt et al., Suppl. Fig. S2

203x246mm (300 x 300 DPI)

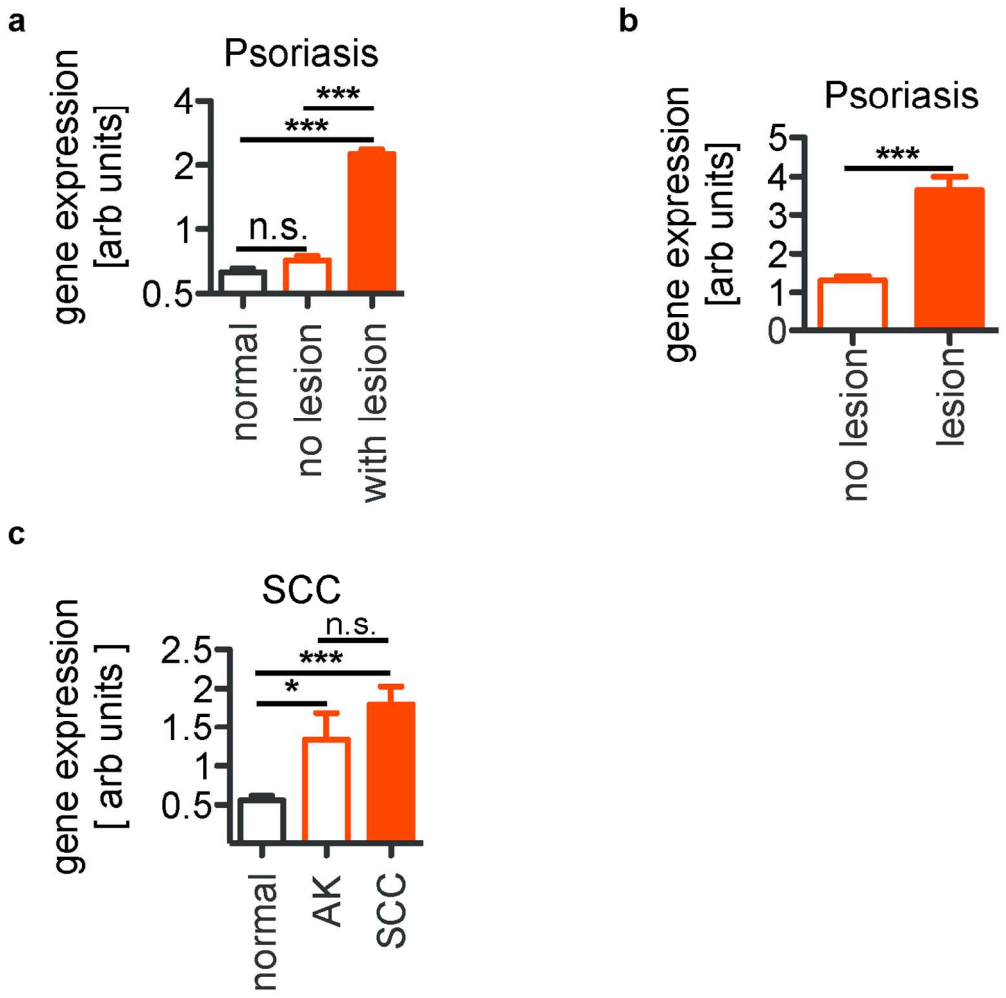

Schmidt et al., Suppl. Fig. S3

128x146mm (300 x 300 DPI)

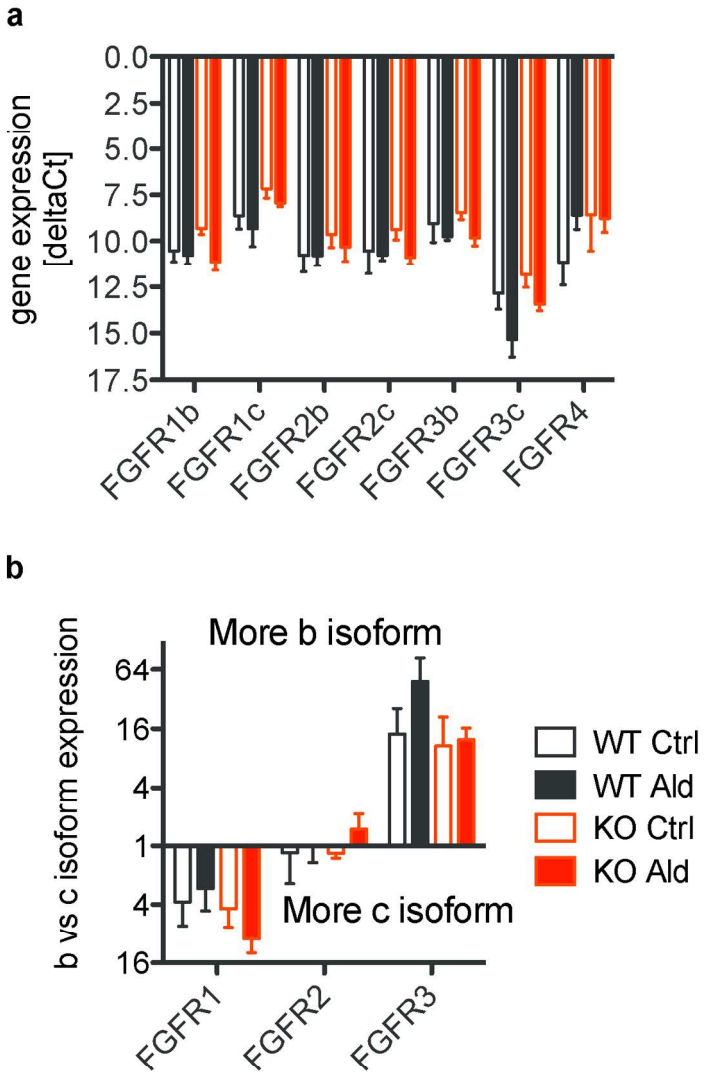

Schmidt et al., Suppl. Fig. S4

117x185mm (300 x 300 DPI)

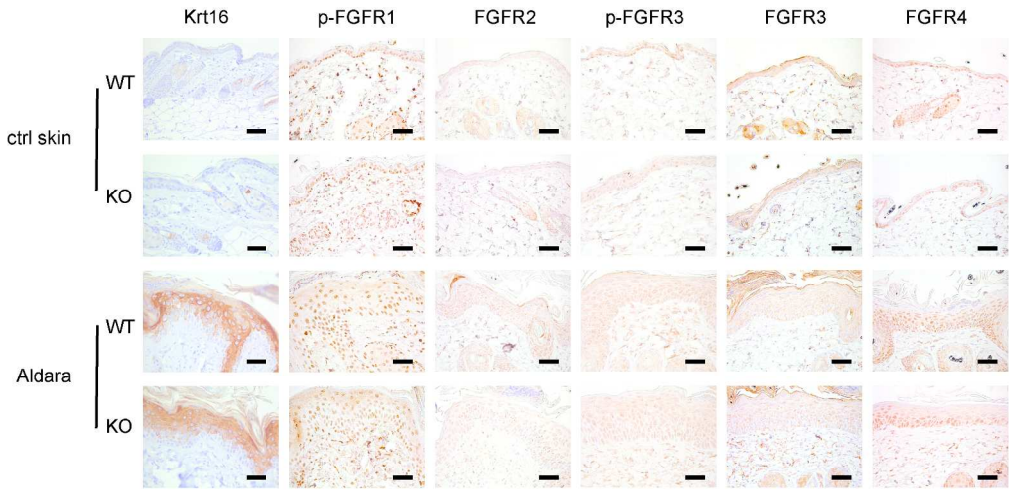

Schmidt et al. Suppl. Fig.S5

260x144mm (300 x 300 DPI)

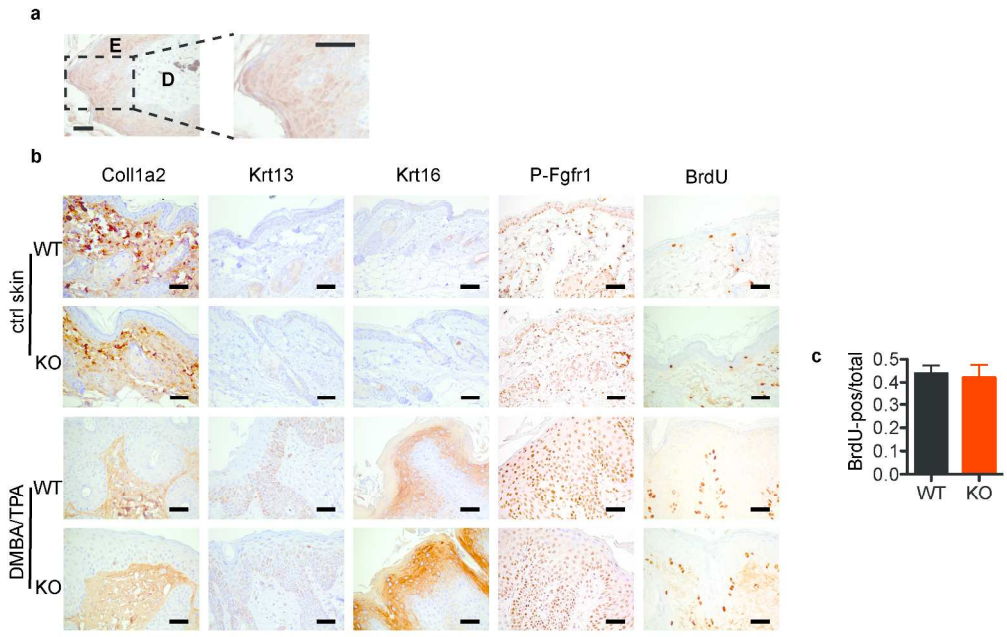

Schmidt et al., Suppl. Fig. S6

260x179mm (300 x 300 DPI)

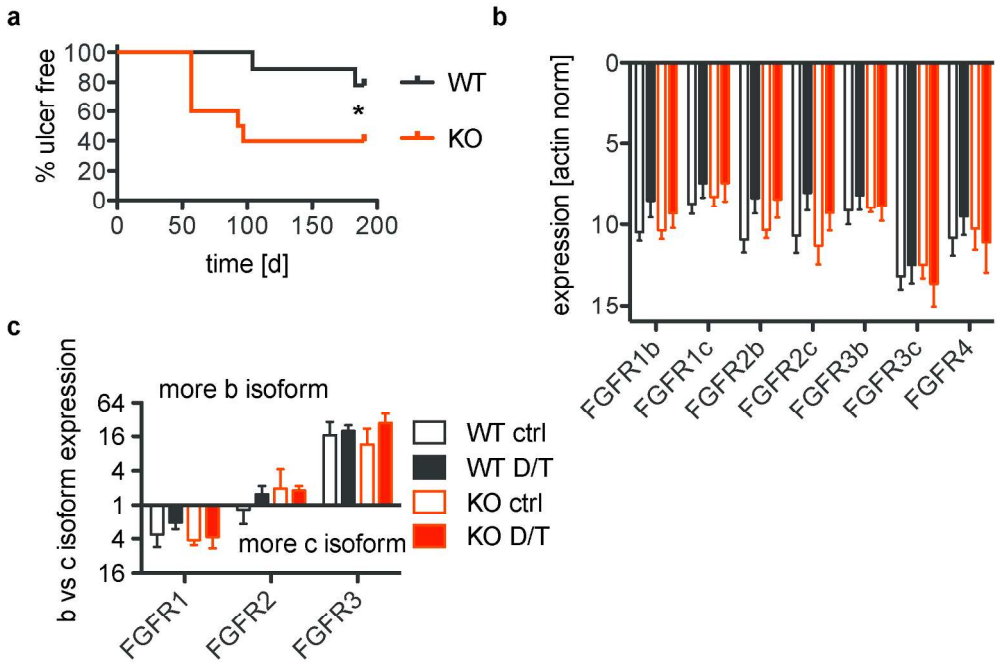

Schmidt et al., Suppl. Fig. S7

192x156mm (300 x 300 DPI)

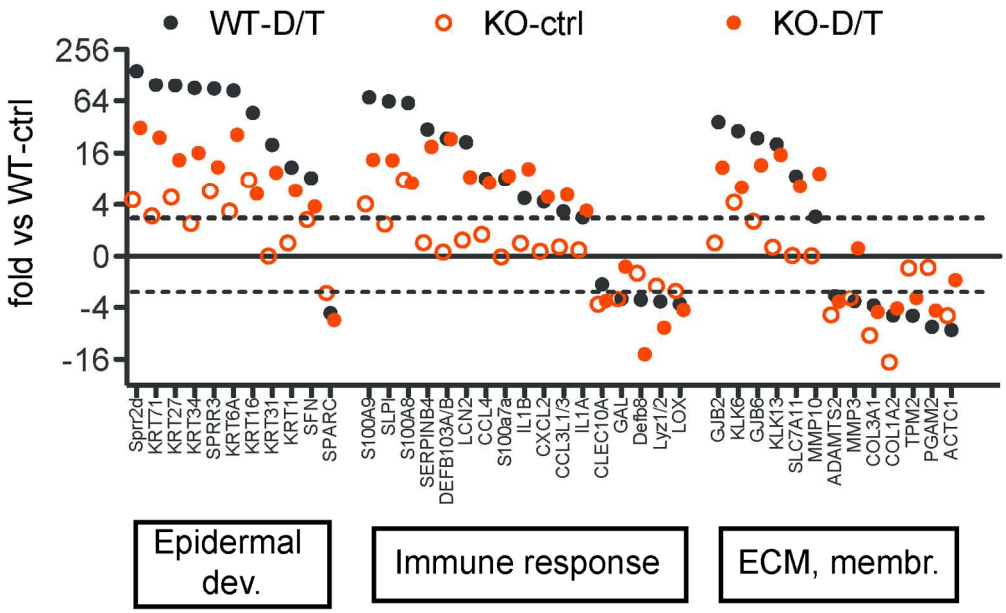

Schmidt et al., Suppl. Fig. S8

148x110mm (300 x 300 DPI)

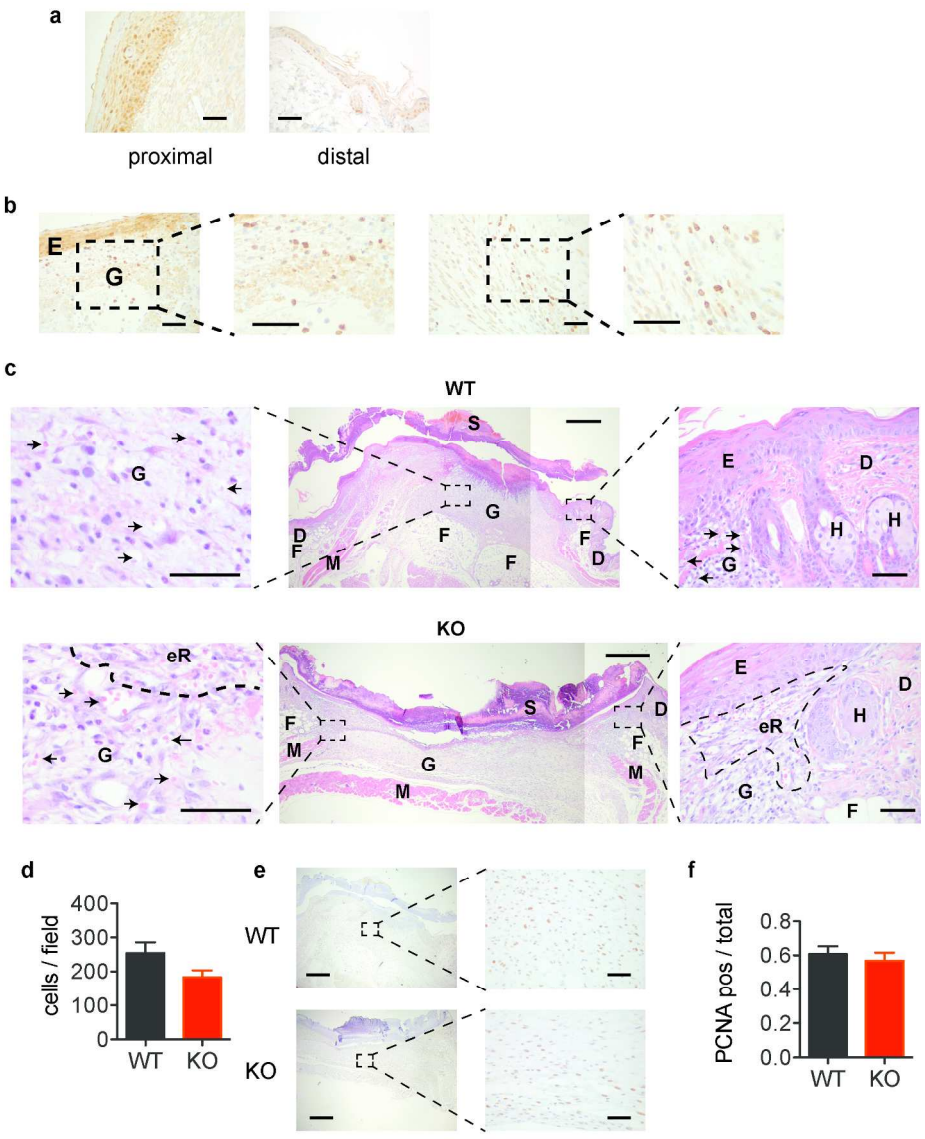

Schmidt et al. Suppl. Fig. S9

201x263mm (300 x 300 DPI)

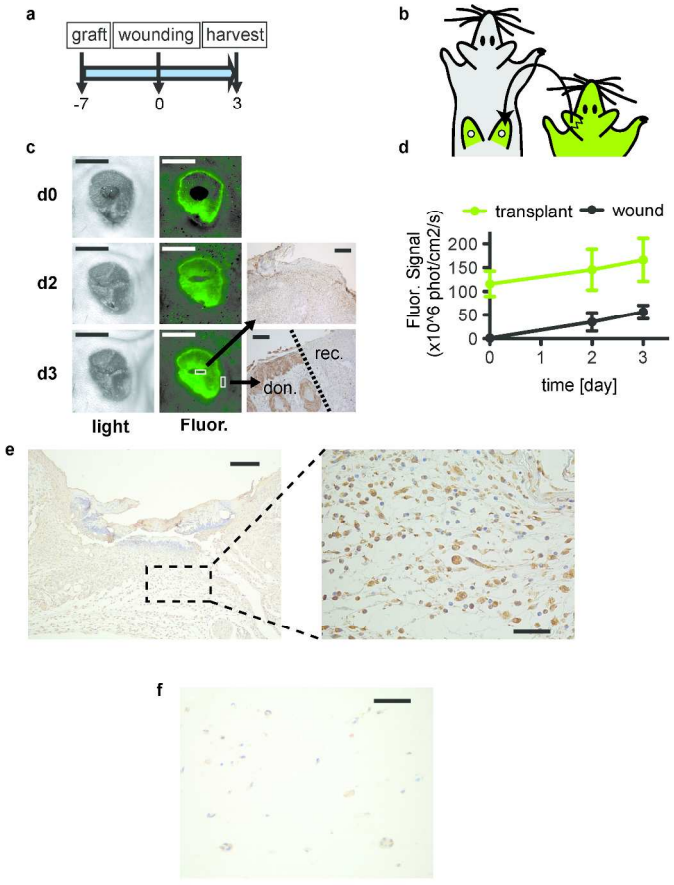

Schmidt et al., Suppl. Fig. S10

279x259mm (300 x 300 DPI)

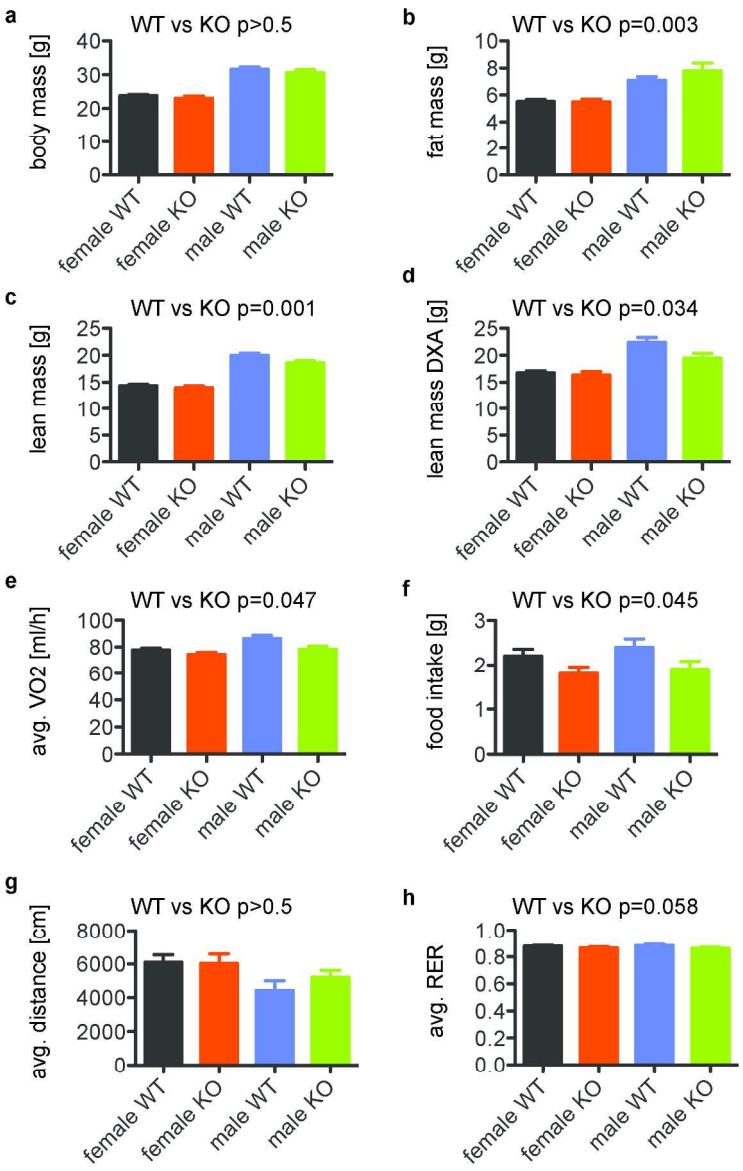

Schmidt et al., Suppl. Fig. S11

165x268mm (300 x 300 DPI)

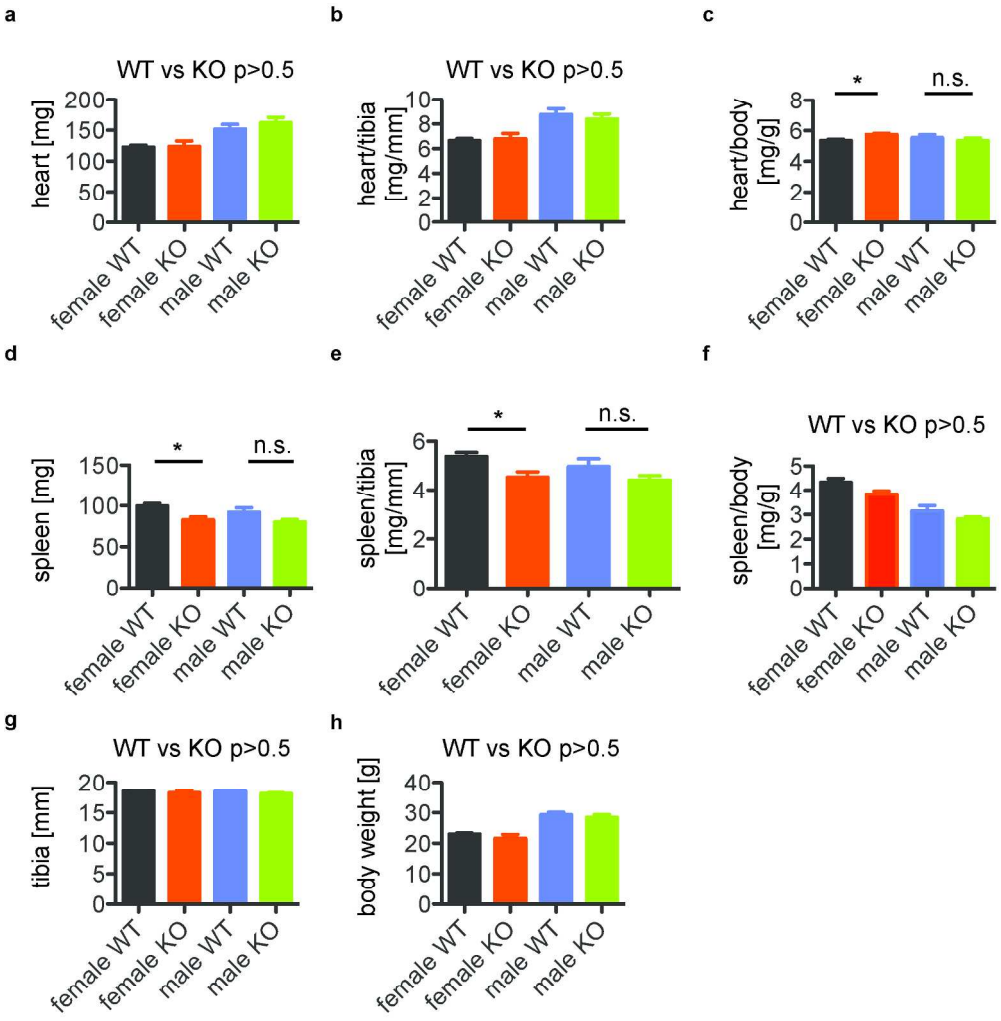

Schmidt et al., Suppl. Fig. S12

204x220mm (300 x 300 DPI)

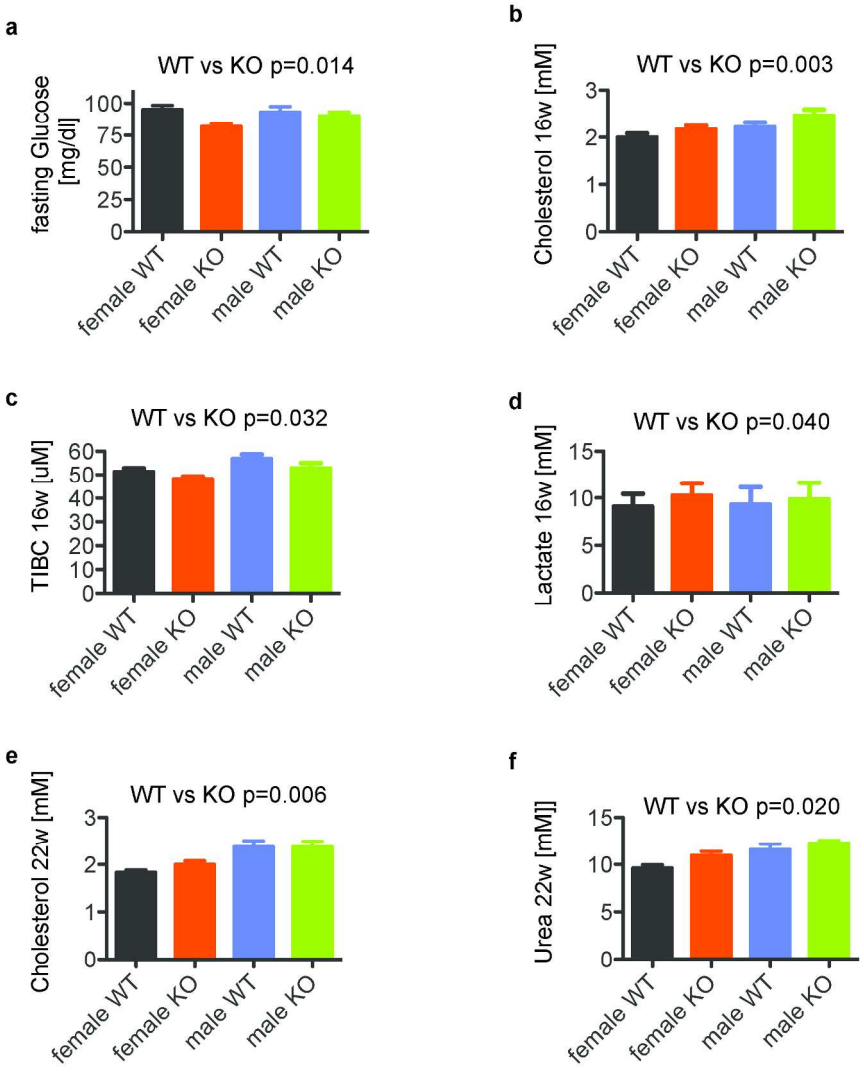

Schmidt et al., Suppl. Fig. S13

182x254mm (300 x 300 DPI)

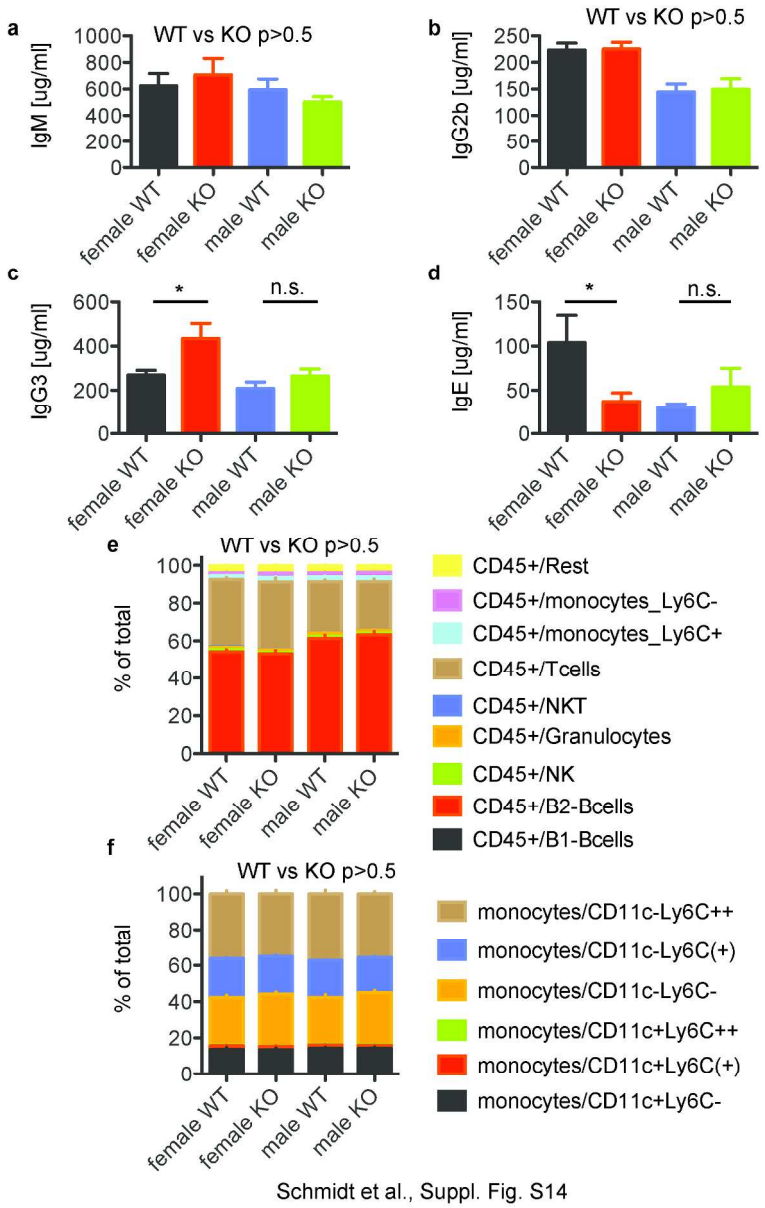

Schmidt et al., Suppl. Fig. S14

172x273mm (300 x 300 DPI)

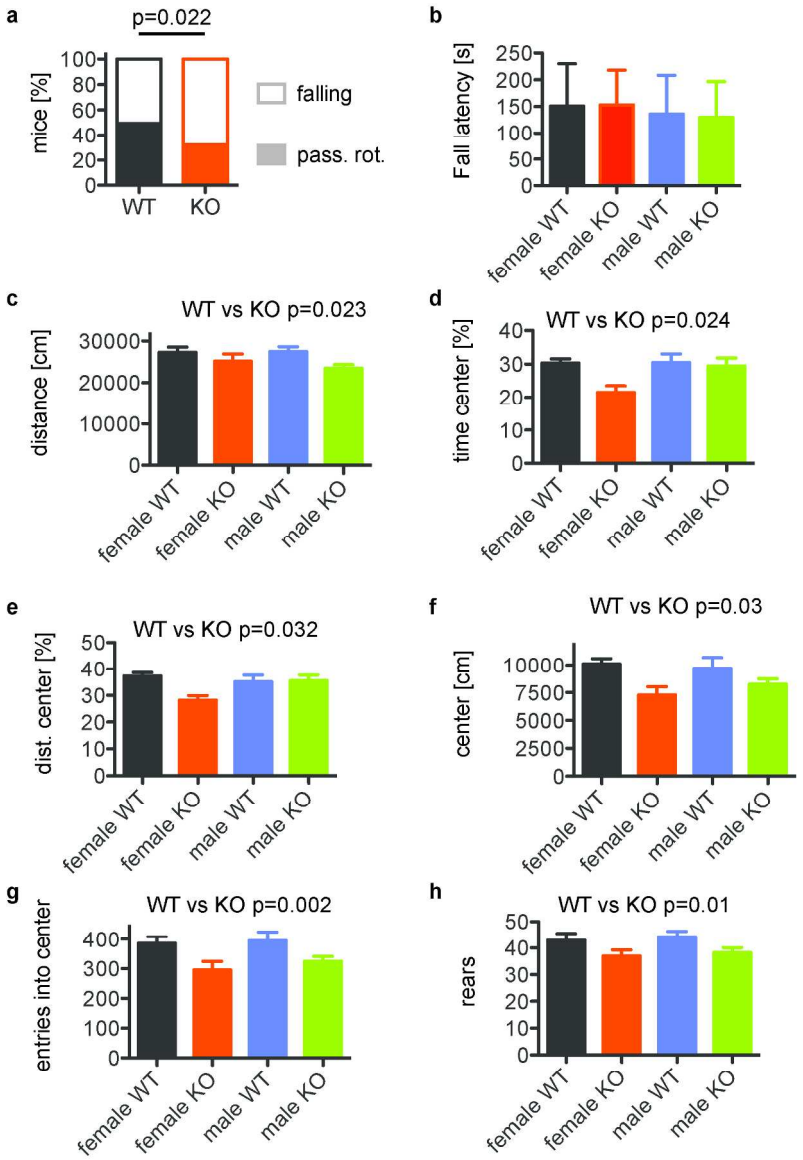

Schmidt et al., Suppl. Fig. S15

179x270mm (300 x 300 DPI)

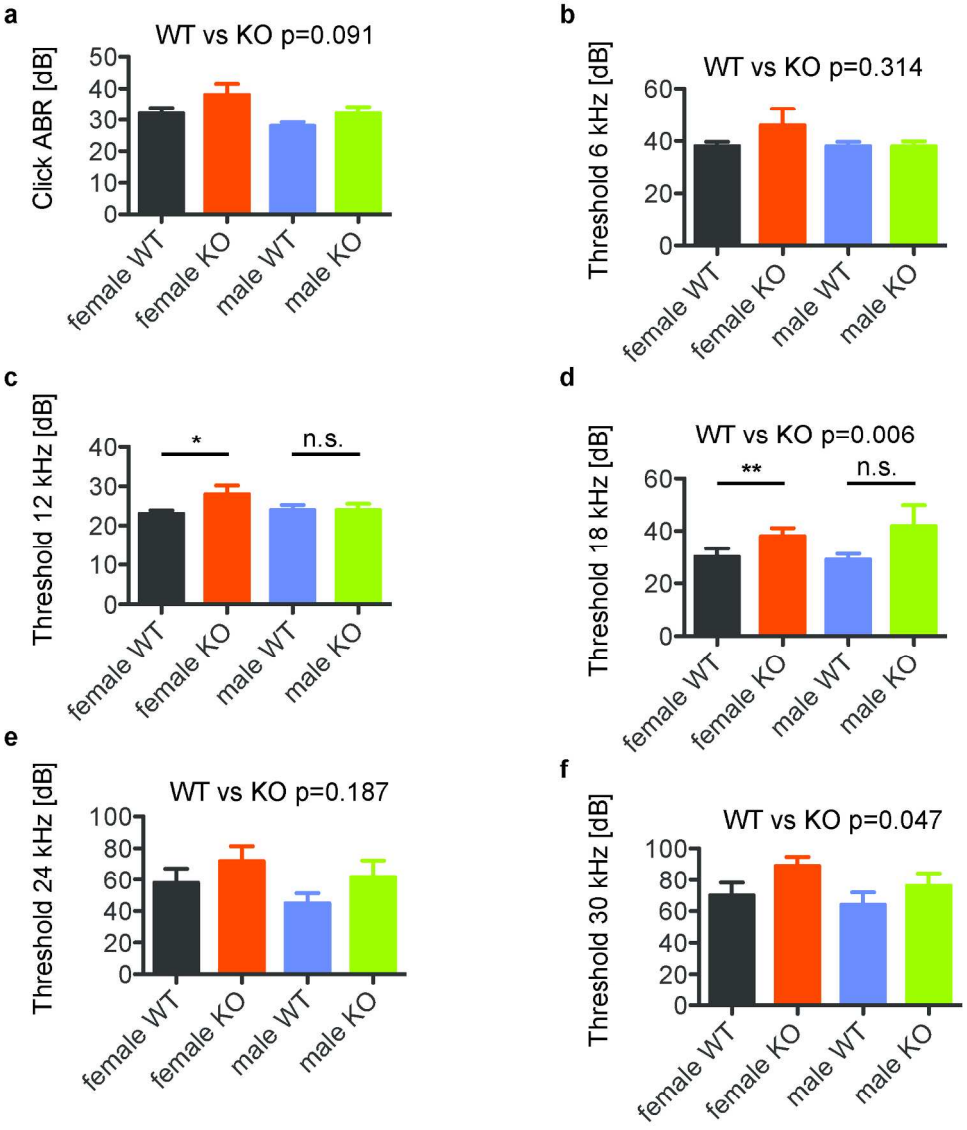

Schmidt et al., Suppl. Fig. S16

183x227mm (300 x 300 DPI)

Suppl. table S1. Phenotype screen overview						
GMC Module	**Parameterset**	**age in weeks**	**significant parameters**	**KO vs WT [p=value]**	**Figure**	**Table**
Behaviour	Open Field	8	decreased travel, less center, slower, decrease rearing	<0.05	S15c-h	S11
Behaviour	Acoustic Startle and PPI	9		n.s.		S14
Cardiovascular	ECG	14		n.s.		S15
Clinical Chemistry	Simplified IPGTT	13	basal fasting Glucose	<0.05	S13a	S6
Clinical Chemistry	Clinical Chemistry (ad. lib. fed mice)	16	cholesterol, TIBC, Lactate	<0.05	S13b, c, d	S7
Clinical Chemistry	Clinical Chemistry (ad. lib. fed mice)	22	cholesterol, Urea	<0.05	S13e, f	S8
Clinical Chemistry	Clinical Chemistry (fasting values)	10		n.s.		S16
Clinical Chemistry	Hematology	16		n.s.		S17
Dysmorphology	DEXA	19	lean mass		S11d	S2
Dysmorphology	Morphological Observation	11		n.s.		
Eyes	Eye Size, Optical coherence tomography, Scheimpflug analysis, Virtual Drum	15		n.s.		
Immunology	Determination of immunglobuline levels in blood	16	IgG3, IgE	<0.05	S14	S9
Metabolism	Minispec MRI	12		n.s.		S18
Metabolism	Minispec MRI	20	fat mass, lean mass	<0.05	S11b, c	S3
Metabolism	Calorimetry TSE	12	food intake, avg. VO2	<0.05	S11e-h	S4
Metabolism	Food efficiency	21		n.s.		S19
Molecular phenotyping	genome-wide transcriptome analysis of liver	24	24 genes >1.5 fold, <-1.5 fold			S10
Neurology	Rotarod	9	increased falling, less passive rotation	0.022	S15a, b	S12
Neurology	Auditory brainstem response	19	threshold at 12, 18, 30 kHz	<0.05	S16	S13
Neurology	Modified SHIRPA	8		n.s.		S14
Neurology	Grip Strength	8		n.s.		S20
Nociceptive	Hotplate	11		n.s.		S21
Pathology	Organ weight	22	Spleen, heart	<0.05	S12	S5

Suppl. table S2. Dysmorphology (DXA, 11 weeks)									
	female		male		females	males			
	WT	KO	WT	KO	genotype		genotype	sex	sex:genotype
	N=15	N=15	N=14	N=14	adj. p-value	adj. p-value	p-value	p-value	p-value
	mean ± sd	mean ± sd	mean ± sd	mean ± sd	pairwise (Tukey)		ANOVA		
BMD [mg/cm^2]	50 ± 3	50 ± 2	52 ± 5	54 ± 5	0.966	0.507	0.528	0.003	0.190
BMC [mg]	415 ± 80	414 ± 53	511 ± 72	511 ± 163	1.000	1.000	0.994	0.001	0.990
Body length [cm]	9.39 ± 0.20	9.29 ± 0.45	9.69 ± 0.20	9.63 ± 0.19	0.737	0.933	0.255	< 0.001	0.779
Body weight [g]	24.05 ± 2.01	23.89 ± 2.85	32.36 ± 3.14	30.84 ± 3.26	0.999	0.491	0.278	< 0.001	0.361
Fat Mass [g]	2.29 ± 1.56	2.51 ± 1.46	4.13 ± 2.06	5.56 ± 4.65	0.996	0.509	0.266	0.001	0.398
Lean Mass [g]	16.74 ± 1.62	16.34 ± 2.61	22.42 ± 3.19	19.49 ± 3.39	0.978	0.034	0.029	< 0.001	0.088

Suppl. table S3. Body composition (MRI, 20 weeks)								
	female		male		Linear model			
	WT	KO	WT	KO	sex	genotype	body mass	sex:genotype
	n=15	n=15	n=14	n=15				
	mean ± sd	mean ± sd	mean ± sd	mean ± sd	p-value	p-value	p-value	p-value
Body mass NMR [g]	23.8 ± 1.6	23.1 ± 2.5	31.6 ± 2.7	30.6 ± 3.4	< 0.001	0.237	NA	0.809
Fat mass NMR [g]	5.5 ± 0.6	5.5 ± 0.8	7.1 ± 0.9	7.8 ± 2.1	0.006	0.003	< 0.001	0.028
Lean mass NMR [g]	14.4 ± 0.9	14 ± 1.4	20 ± 1.6	18.6 ± 1.6	< 0.001	0.001	< 0.001	0.014

Suppl. table S4. Calorimetry (12 weeks)								
	female		male		Linear model			
	WT	KO	WT	KO	sex	genotype	body mass	sex:genotype
	n=15	n=15	n=14	n=15				
	mean ± sd	mean ± sd	mean ± sd	mean ± sd	p-value	p-value	p-value	p-value
avg. body weight [g]	20.6 ± 1.7	20.6 ± 2	28 ± 3.3	25.7 ± 2.2	< 0.001	0.067	NA	0.070
Food intake [g]	2.2 ± 0.6	1.8 ± 0.6	2.4 ± 0.7	1.9 ± 0.7	0.034	0.045	0.002	0.789
avg. VO2 [ml/(h animal)]	77.783 ± 5.963	74.421 ± 6.65	86.409 ± 8.975	78.499 ± 8.755	0.016	0.047	< 0.001	0.967
min. VO2 [ml/(h animal)]	46.933 ± 6.181	45.667 ± 6.925	56 ± 6.598	49.533 ± 5.78	0.060	0.160	< 0.001	0.625
max. VO2 [ml/(h animal)]	115.467 ± 10.46	105.933 ± 14.002	128.357 ± 11.057	119.8 ± 19.068	0.997	0.070	0.007	0.418
avg. RER VCO2/VO2	0.879 ± 0.031	0.865 ± 0.035	0.883 ± 0.038	0.862 ± 0.037	0.970	0.058	NA	0.665
avg. distance [cm]	6100 ± 1750	6013 ± 2278	4425 ± 2166	5206 ± 1566	0.018	0.500	NA	0.398
avg. rearing [counts]	181 ± 79	171 ± 86	100 ± 62	117 ± 41	< 0.001	0.840	NA	0.462

Suppl. table S5. Pathology							
	female		male		female	male	overall
	WT	KO	WT	KO	Wilcoxon rank-sum test		
	n=5	n=5	n=6	n=6			
	median [25%, 75%]	median [25%, 75%]	median [25%, 75%]	median [25%, 75%]	p-value		
Heart weight [mg]	125 [121 , 126]	118 [114 , 132]	154[a] [153 , 161]	153 [138 , 158.2]	1	0.537	0.986
Tibia length [mm]	18.5 [18.4 , 18.6]	18.5 [18.2 , 18.8]	18.5 [18.3 , 18.6]	18.1 [18 , 18.3]	1	0.18	0.21
Liver weight [g]	1.191 [1.153 , 1.244]	1.153 [1.015 , 1.183]	1.551[a] [1.532 , 1.572]	1.473 [1.368 , 1.594]	0.46	0.662	0.771
Spleen weight [g]	0.104 [0.096 , 0.104]	0.079 [0.077 , 0.083]	0.092[a] [0.089 , 0.101]	0.08 [0.074 , 0.084]	0.032	0.132	0.005
Body weight [g]	23.128 [22.752 , 23.245]	20.848 [19.872 , 22.996]	28.585 [27.64 , 29.907]	28.241 [26.979 , 30.223]	0.31	0.937	0.949
Heart Weight / Tibia Length [mg/mm]	6.76 [6.45 , 6.83]	6.39 [6.03 , 7.03]	8.36[a] [8.27 , 8.75]	8.56 [7.53 , 8.8]	0.635	0.89	0.904
Heart Weight / Body Weight [mg/g]	5.32 [5.24 , 5.4]	5.74 [5.66 , 5.74]	5.5[a] [5.11 , 5.85]	5.31 [4.97 , 5.75]	0.016	0.537	0.5
Liver Weight / Tibia Length [mg/mm]	64.66 [62.2 , 66.35]	62.39 [53.7 , 62.99]	82.46[a] [82.28 , 85.48]	80.83 [75.23 , 87.33]	0.548	0.931	0.918
Liver Weight / Body Weight [mg/g]	54.21 [49.47 , 54.68]	51.44 [51.08 , 53.92]	54.74[a] [53.15 , 57.11]	52.28 [50.39 , 53.67]	0.841	0.329	0.282
Spleen Weight / Tibia Length [mg/mm]	5.58 [5.25 , 5.6]	4.42 [4.11 , 4.67]	4.94[a] [4.86 , 5.45]	4.36 [4.07 , 4.7]	0.032	0.247	0.007
Spleen Weight / Body Weight [mg/g]	4.33 [4.15 , 4.61]	3.8 [3.65 , 3.87]	3.17[a] [2.95 , 3.29]	2.79 [2.66 , 2.89]	0.056	0.195	0.119

Suppl. table S6. IpGTT							
	female		male		Linear model		
	WT	KO	WT	KO	genotype	sex	sex:genotype
	n=15	n=15	n=14	n=15			
	mean ± sd	mean ± sd	mean ± sd	mean ± sd	p-value	p-value	p-value
Glucose (T=0) [mg/dl]	95.12 ± 12.61	81.8 ± 8.29	93.15 ± 16.04	90.27 ± 10.99	0.014	0.316	0.111
AUC 0-30	4068 ± 1026	4043 ± 1215	5613 ± 1185	5785 ± 1315	0.815	< 0.001	0.753
AUC 30-120	6340 ± 1922	6810 ± 2209	12018 ± 3205	12098 ± 3408	0.706	< 0.001	0.788

Suppl. table S7. Clinical Chemistry (16 weeks)							
	female		male		Linear model		
	WT	KO	WT	KO	genotype	sex	genotype:sex
	n=15	n=15	n=14	n=14			
	mean ± sd	mean ± sd	mean ± sd	mean ± sd	p-value	p-value	p-value
Cholesterol [mmol/l]	2.006 ± 0.294	2.174 ± 0.28	2.229 ± 0.347	2.473 ± 0.437	0.003	0.005	0.673
Triglyceride [mmol/l]	0.979 ± 0.163	0.827 ± 0.178	1.547 ± 0.378	1.798 ± 0.475	0.180	< 0.001	0.114
ALAT/GPT [U/l]	25 ± 4	36 ± 17	38 ± 22	45 ± 25	0.077	0.024	0.617
ASAT/GOT [U/l]	45 ± 8	51 ± 17	43 ± 8	39 ± 5	0.664	0.011	0.085
alpha-Amylase [U/l]	585.76 ± 58.16	600.08 ± 48.33	698.17 ± 112.16	705.92 ± 106.98	0.624	<0.001	0.884
Glucose [mmol/l]	244.50 ± 35.30	229.55 ± 34.22	229.73 ± 33.15	151.53 ± 28.11	0.261	0.116	0.527
LDH [U/l]	257.2 ± 40.4	293.4 ± 50.6	254.3 ± 50.2	263.6 ± 61.6	0.096	0.229	0.319
Fructosamine [umol/l]	346.9 ± 18.1	348.5 ± 32.2	359.9 ± 24.8	355.1 ± 36.9	0.831	0.199	0.678
Sodium [mmol/l]	149 ± 2	150 ± 2	147 ± 2	147 ± 3	0.513	0.001	0.188
Potassium [mmol/l]	3.8 ± 0.3	3.9 ± 0.3	4.5 ± 0.6	4.3 ± 0.6	0.862	< 0.001	0.307
Chloride [mmol/l]	111.7 ± 2	113.1 ± 2	107.9 ± 1.9	107 ± 1.9	0.550	< 0.001	0.027
Total protein [g/l]	51.4 ± 2.9	50.1 ± 1.4	46.9 ± 2.6	48.5 ± 2.5	0.841	< 0.001	0.021
Albumin [g/l]	29.8 ± 2.9	28.6 ± 1.9	24.4 ± 2	25.8 ± 1.6	0.876	< 0.001	0.026
Creatinine enz. [mumol/l]	10.97 ± 1.56	11.35 ± 1.2	10.72 ± 2.81	11.06 ± 2.12	0.499	0.611	0.977
Urea [mmol/l]	10.39 ± 2.1	10.64 ± 1.58	11.3 ± 1.98	12.05 ± 1.5	0.296	0.018	0.601
Calcium [mmol/l]	2.57 ± 0.11	2.6 ± 0.12	2.45 ± 0.07	2.47 ± 0.1	0.362	< 0.001	0.828
Inorganic phosphate [mmol/l]	2.16 ± 0.38	2.17 ± 0.38	1.97 ± 0.48	1.74 ± 0.45	0.323	0.007	0.269
Iron [mumol/l]	23.18 ± 4.461	24.907 ± 4.071	21.2 ± 2.857	22.536 ± 2.806	0.116	0.027	0.839
ALP [U/l]	133 ± 15	129 ± 20	70 ± 7	79 ± 14	0.506	< 0.001	0.118
Unsaturated iron binding capacity [mumol/l]	28.2 ± 6.6	23.4 ± 6.4	35.7 ± 7.3	30.4 ± 8.1	0.009	< 0.001	0.904
Total iron binding capacity [mumol/l]	51.4 ± 5.3	48.3 ± 4	56.9 ± 6.7	52.9 ± 8	0.032	0.003	0.794
Calc transferrin saturation [\%]	45.5 ± 8.8	52.1 ± 10.8	37.7 ± 6.4	43.5 ± 9	0.011	0.001	0.860
Lactate [mmol/l]	9.13 ± 1.31	10.28 ± 1.27	9.34 ± 1.82	9.91 ± 1.72	0.040	0.840	0.490

Suppl. table S8. Clinical Chemistry (22 weeks)							
	female		male		Linear model		
	WT	KO	WT	KO	genotype	sex	genotype:sex
	n=15	n=15	n=14	n=14			
	mean ± sd	mean ± sd	mean ± sd	mean ± sd	p-value	p-value	p-value
Cholesterol [mmol/l]	1.828 ± 0.221	1.996 ± 0.29	2.034 ± 0.314	2.372 ± 0.388	0.006	0.002	0.337
Triglyceride [mmol/l]	0.849 ± 0.201	0.827 ± 0.218	1.478 ± 0.481	1.843 ± 0.763	0.191	< 0.001	0.142
ALAT/GPT [U/l]	21 ± 6	20 ± 4	23 ± 9	21 ± 3	0.363	0.267	0.956
ASAT/GOT [U/l]	41 ± 5	43 ± 6	38 ± 4	35 ± 3	0.700	< 0.001	0.058
alpha-Amylase [U/l]	612.85 ± 134.25	623.21 ± 75.58	672.97 ± 73.18	722.13 ± 91.99	0.315	0.009	0.511
Glucose [mmol/l]	161.8 ± 16.76	165.59 ± 1.22	165.59 ± 21.98	149.73 ± 33.15	0.704	0.073	0.882
LDH [U/l]	178 ± 43.6	186.1 ± 42.3	229.5 ± 37.9	196.1 ± 26.6	0.272	0.010	0.075
Fructosamine [umol/l]	331.8 ± 24	329.1 ± 25.1	408.1 ± 37	408.6 ± 19.7	0.890	< 0.001	0.836
Total protein [g/l]	50.5 ± 2.4	49.9 ± 1.9	50.2 ± 1.4	51.4 ± 1.8	0.635	0.285	0.114
Albumin [g/l]	29.4 ± 1.6	28.6 ± 1.1	26.8 ± 1.6	27.6 ± 0.9	0.935	< 0.001	0.052
Creatinine enz. [mumol/l]	14.45 ± 5.62	15.44 ± 6.35	11.37 ± 7.4	13.84 ± 7.36	0.372	0.228	0.700
Urea [mmol/l]	9.61 ± 1.31	10.94 ± 1.62	11.57 ± 1.82	12.26 ± 0.94	0.020	< 0.001	0.451
Calcium [mmol/l]	2.35 ± 0.04	2.34 ± 0.06	2.37 ± 0.08	2.41 ± 0.07	0.340	0.010	0.145
Inorganic phosphate [mmol/l]	1.15 ± 0.25	1.11 ± 0.12	0.98 ± 0.19	1.05 ± 0.25	0.715	0.065	0.372
Iron [mumol/l]	22.504 ± 2.677	23.788 ± 3.545	22.473 ± 3.615	20.125 ± 1.901	0.545	0.040	0.043
ALP [U/l]	119 ± 12	128 ± 20	63 ± 6	66 ± 7	0.143	< 0.001	0.421
Total iron binding capacity [mumol/l]	57.2 ± 4	55.3 ± 3.8	54.8 ± 5.5	53.9 ± 3.5	0.248	0.129	0.718
Calc transferrin saturation [\%]	39.5 ± 5.3	43.3 ± 7.4	41.4 ± 8.5	37.6 ± 5.1	0.997	0.318	0.055

Suppl. table S9. Immunology

	female		male		female	male	overall
	WT	KO	WT	KO	Wilcoxon rank-sum test		
	n=15	n=15	n=14	n=14			
	median [25%, 75%]	median [25%, 75%]	median [25%, 75%]	median [25%, 75%]	p-value	p-value	p-value
Ig M	501.81[a] [374.98 , 737.78]	596.17 [348.39 , 773.37]	461.33 [394.02 , 660.4]	456.99 [404.62 , 504.75]	0.660	1.000	0.8230
IgG2b	220.12[a] [197.12 , 237.68]	234.97 [176.96 , 245.79]	131.62 [100.51 , 187.56]	120.91 [95.54 , 172.34]	0.949	0.710	0.9840
IgG3	268.49[a] [223.94 , 344]	401.82 [274.64 , 470.79]	175.02 [134.39 , 214.06]	246.35 [181.82 , 317.93]	0.020	0.169	0.0200
IgE	57.1 [34.55,91.75]	26.3 [16.5,38.9]	26.05 [18.23,37.33]	28.55 [18.32,45.12]	0.022	0.752	0.1320
CD45+/Tcells	35.7 [34.1 , 38]	32.9 [29.8 , 41.3]	26.05 [25.23 , 27.65]	24.25 [22.75 , 27.45]	0.814	0.270	0.555
CD45+/B-2cells	53.2 [51.7 , 57.4]	53.8 [48.4 , 59.2]	62.35 [60.15 , 64.58]	65.4 [59.48 , 66.78]	0.721	0.312	0.725
CD45+/B-1cells	0.18 [0.17 , 0.24]	0.2 [0.17 , 0.24]	0.14 [0.09 , 0.16]	0.12 [0.1 , 0.16]	0.992	0.955	0.754
CD45+/CD11b+Ly6G+	1.02 [0.62 , 1.24]	1.33 [1 , 1.66]	1.37 [1.06 , 1.88]	0.9 [0.73 , 1.33]	0.072	0.153	0.905
CD45+/NKcells	0.99 [0.8 , 1.71]	0.88 [0.56 , 1.23]	1.29 [0.88 , 1.73]	0.99 [0.86 , 1.22]	0.140	0.270	0.094
CD45+/NKTcells	0.37 [0.3 , 0.46]	0.18 [0.16 , 0.26]	0.32 [0.18 , 0.4]	0.2 [0.16 , 0.28]	< 0.001	0.181	< 0.001
CD45+/Ly6C-CD11b+	4.2 [3.68 , 4.58]	4.51 [4.25 , 5.05]	4.49 [3.96 , 5.21]	4.83 [4.23 , 5.25]	0.177	0.643	0.192
CD45+/Ly6C+CD11b+	2.48 [2.24 , 3.06]	2.84 [2.19 , 3.48]	2.86 [2.29 , 3.87]	3.13 [2.83 , 3.21]	0.330	0.759	0.328
CD45+/non-spec-rest	0.55 [0.42 , 0.6]	0.59 [0.46 , 0.64]	0.6 [0.53 , 0.65]	0.5 [0.45 , 0.56]	0.280	0.063	0.663
NKcells/CD11b+	71.7 [68.05 , 74]	72.7 [65.8 , 75.7]	66.1 [63.92 , 72.47]	63.3 [60.98 , 67.9]	0.705	0.198	0.339
NKcells/CD11c+	3.21 [3 , 5.08]	6.09 [4.71 , 7.83]	5.38 [3.85 , 6.73]	5.62 [4.91 , 8.08]	0.040	0.541	0.036
NKcells/Ly6C+	31.8 [30.4 , 34.65]	32.2 [28.5 , 36.75]	29.65 [27.68 , 35.3]	28.8 [26.75 , 33.67]	0.975	0.475	0.470
Bcells/CD11b+	0.47 [0.4 , 0.54]	0.46 [0.37 , 0.55]	0.54 [0.43 , 0.71]	0.7 [0.54 , 0.98]	0.894	0.197	0.465
Bcells/Ly6C+	0.24 [0.16 , 0.3]	0.22 [0.18 , 0.28]	0.23 [0.14 , 0.39]	0.23 [0.19 , 0.39]	0.992	0.563	0.591
Tcells/Ly6C+	12.5 [10.11 , 13.6]	11.2 [10.12 , 14.2]	17.95 [12.88 , 22.68]	16.75 [13.78 , 18.1]	0.894	0.301	0.731
monocytes/Ly6C-CD11c-	48 [43.2 , 52.45]	46.9 [43.2 , 51.15]	41.15 [36.65 , 48.5]	44.3 [38.52 , 49.17]	0.783	0.448	0.737
monocytes/Ly6C-CD11c+	7.84 [6.62 , 9.23]	8.22 [6.42 , 9.3]	8.69 [8.11 , 10.6]	9.59 [8.04 , 10.15]	0.775	0.626	0.624
monocytes/Ly6C++CD11c+	0.18 [0.11 , 0.26]	0.23 [0.12 , 0.31]	0.32 [0.21 , 0.42]	0.34 [0.25 , 0.45]	0.505	0.692	0.465
monocytes/Ly6C++CD11c-	18.6 [16.8 , 23.15]	19.4 [18.3 , 23.15]	23.15 [20.02 , 27]	23.5 [21.23 , 27.02]	0.690	0.848	0.680
monocytes/Ly6C(+)CD11c+	1.3 [0.98 , 1.6]	1.27 [0.96 , 1.64]	1.66 [1.36 , 1.75]	1.19 [1.05 , 1.64]	0.967	0.206	0.397
monocytes/Ly6C(+)CD11c-	22.2 [21.6 , 23.8]	20.4 [19.55 , 23.7]	21.55 [21.2 , 23.38]	20.75 [19.05 , 21.9]	0.134	0.060	0.013

[a]Number not based on the full number of animals (missing values)

Suppl. table S10. gene expression array			
Gene symbol	**Gene name**	**fold change KO/WT**	**St Err.**
Actb	actin, beta	2.128	0.447
Dbp	D-box binding PAR bZIP transcription factor	2.008	0.657
Cyp4a14	cytochrome P450, family 4, subfamily a, polypeptide 14	1.862	1.009
Bsdc1	BSD domain containing 1	1.774	0.080
Insig1	insulin induced gene 1	1.743	0.223
Gpn2	GPN-loop GTPase 2	1.739	0.181
Egfr	epidermal growth factor receptor	1.655	0.409
Uroc1	urocanate hydratase 1	1.564	0.121
Tuft1	tuftelin 1	1.552	0.262
Psmb5	Proteasome subunit beta type-5	1.521	0.051
Raet1b	Retinoic acid early-inducible protein 1-beta	1.511	0.051
C9	complement component 9	-1.581	0.233
Anpep	alanyl aminopeptidase, membrane	-1.505	0.040
Plk3	polo like kinase 3	-1.531	0.152
Hmgcl	3-hydroxymethyl-3-methylglutaryl-CoA lyase	-1.565	0.206
Extl1	exostosin-like glycosyltransferase 1	-1.570	0.118
TMEM234	transmembrane protein 234	-1.703	0.230
S100a1	S100 calcium binding protein A1	-1.971	0.551
Xdh	xanthine dehydrogenase	-2.136	0.575
Foxq1	forkhead box Q1	-2.386	0.482
Gadd45g	growth arrest and DNA damage inducible gamma	-2.376	0.413
Phlda1	pleckstrin homology like domain family A member 1	-2.304	0.171
Mt1	metallothionein 1	-3.321	0.748
Egr1	early growth response 1	-3.486	1.562

Suppl. table S11. Open field							
	female		male		Linear model		
	WT	KO	WT	KO	genotype	sex	genotype:sex
	n=15	n=15	n=14	n=15			
	mean ± sd	mean ± sd	mean ± sd	mean ± sd	p-value	p-value	p-value
Distance travelled - 5 min [cm]	7600.5 ± 1612.45	7297.63 ± 2221.88	8062.35 ± 1452.79	6716.52 ± 1481.84	0.072	0.895	0.251
Distance travelled - 10 min [cm]	6826.77 ± 1437.04	6397.69 ± 1969.75	6876.36 ± 1144.38	5850.34 ± 985.04	0.057	0.509	0.429
Distance travelled - 15 min [cm]	6399.13 ± 1076.35	5839.39 ± 1563.96	6377.23 ± 1747.53	5580.78 ± 1043.5	0.065	0.699	0.744
Distance travelled - 20 min [cm]	6460.64 ± 1371.1	5623.25 ± 1633.29	6131.07 ± 1165.12	5314.91 ± 772.99	0.016	0.342	0.975
Distance travelled - Total [cm]	27287.04 ± 4844.01	25157.95 ± 6751.18	27447.04 ± 4512.14	23462.55 ± 3399.27	0.023	0.561	0.482
Number of rears - 5 min	38.6 ± 9.55	31.2 ± 8.8	38.57 ± 10.99	34.27 ± 10.65	0.029	0.563	0.556
Number of rears - 10 min	43 ± 11.14	38.53 ± 8.43	44.43 ± 10.11	41.6 ± 12.69	0.197	0.424	0.770
Number of rears - 15 min	41.53 ± 10.87	39.07 ± 10.14	43.93 ± 13.27	42.33 ± 8.37	0.472	0.317	0.877
Number of rears - 20 min	42.87 ± 10.18	36.93 ± 9	44.29 ± 7.8	38.2 ± 7.31	0.010	0.554	0.973
Number of rears - Total	165.87 ± 37.54	145.47 ± 29.74	170.57 ± 36.76	155.87 ± 33.43	0.056	0.404	0.752
Percent distance in the center - 5 min	31.4 ± 7.75	23.8 ± 9.2	30.25 ± 7.58	27.16 ± 7.35	0.013	0.598	0.284
Percent distance in the center - 10 min	35.49 ± 7.18	29.71 ± 8.87	35.61 ± 11.56	36.16 ± 10.52	0.302	0.197	0.213
Percent distance in the center - 15 min	41.64 ± 8.14	28.23 ± 8.05	37.06 ± 13.27	38.8 ± 12.59	0.042	0.289	0.009
Percent distance in the center - 20 min	41.17 ± 8.13	31.19 ± 7.83	37.37 ± 11.3	40.67 ± 9.65	0.173	0.246	0.008
Percent distance in the center - Total	37.27 ± 5.09	28.13 ± 6.92	35.05 ± 9.46	35.46 ± 8.45	0.032	0.204	0.019
Percent Time Spent in the Center - 5 min	22.8 ± 7.41	17.37 ± 8.61	26.48 ± 8.77	21 ± 6.84	0.011	0.083	0.990
Percent Time Spent in the Center - 10 min	27.88 ± 8.49	21.41 ± 9.06	30.7 ± 13.76	29.3 ± 11.31	0.167	0.062	0.371
Percent Time Spent in the Center - 15 min	34.68 ± 7.71	21.72 ± 8.34	32.03 ± 13.84	31.55 ± 14.45	0.028	0.235	0.041
Percent Time Spent in the Center - 20 min	35.84 ± 9.24	25.57 ± 9.19	32.47 ± 10.61	35.66 ± 12.44	0.199	0.222	0.017
Percent Time Spent in the Center - Total	30.31 ± 4.81	21.52 ± 7.56	30.41 ± 9.78	29.38 ± 9.47	0.024	0.065	0.072
Whole Arena - resting time [s]	177.24 ± 40.91	150.25 ± 35.41	147.56 ± 54.85	160.06 ± 44.68	0.533	0.393	0.093
Whole Arena - Permanence time [s]	1200 ± 0	1200 ± 0	1200 ± 0	1200 ± 0	NA	NA	NA
Whole Arena - average speed [cm/s]	26.7 ± 4.63	24.11 ± 6.91	26.11 ± 4.14	22.64 ± 3.72	0.024	0.433	0.738
Periphery - distance [cm]	17183.87 ± 3558.35	17897.54 ± 4562.77	17722.79 ± 3698.85	15215.37 ± 3243.68	0.369	0.284	0.109
Periphery - resting time [s]	134.67 ± 30.46	126.64 ± 25.88	113.97 ± 41.18	127.25 ± 39.95	0.774	0.273	0.245
Periphery - Permanence time [s]	836.34 ± 57.67	941.85 ± 90.67	835.09 ± 117.38	847.49 ± 113.51	0.024	0.065	0.072
Periphery - average speed [cm/s]	24.45 ± 4.67	22.48 ± 6.86	24.76 ± 4.19	21.13 ± 3.7	0.036	0.691	0.527
center - distance [cm]	10103.17 ± 1913.14	7260.43 ± 2944.53	9724.22 ± 3574.31	8247.2 ± 1900.55	0.003	0.663	0.329
center - resting time [s]	42.57 ± 18.67	23.61 ± 18.63	33.59 ± 19.82	32.8 ± 14.67	0.040	0.982	0.058
center - Permanence time [s]	363.65 ± 57.68	258.15 ± 90.66	364.91 ± 117.38	352.51 ± 113.51	0.024	0.065	0.072
center - average speed [cm/s]	31.93 ± 5.43	30.5 ± 6.59	29.53 ± 4.92	26.85 ± 5.12	0.162	0.041	0.667
Latency to enter in the center [s]	7.37 ± 5.9	12.77 ± 17.02	6.49 ± 5.93	9.32 ± 10.12	0.150	0.447	0.650
Number of entries in the center	385.6 ± 88.35	295.53 ± 113.2	395.29 ± 112.75	324.73 ± 62.42	0.002	0.441	0.698
Whole Arena Distance [cm]	27287.04 ± 4844.01	25157.95 ± 6751.18	27447.04 ± 4512.14	23462.55 ± 3399.27	0.023	0.561	0.482

Suppl. table S12. Rotarod									
	Male		Female		Both				
	WT	KO	WT	KO	WT	KO	WT	KO	p value [1]
	n=42	n=45	n=45	n=45	n=87	n=90	49.20%	50.80%	
	Absolute	Absolute	Absolute	Absolute	Absolute	Absolute	Percent	Percent	
Passive rotation									0.02235
falling	25	36	19	25	44	61	50.60%	67.80%	
passive rotation	17	9	26	20	43	29	49.40%	32.20%	
jumping	0	0	0	0	0	0	0%	0%	
[1]Fisher's Exact test									

Suppl. table S13. Auditory brain stem response

	female		male		female	male	overall
	WT	KO	WT	KO	Wilcoxon rank-sum test		
	n=10	n=10	n=10	n=10			
	mean ± sd	mean ± sd	mean ± sd	mean ± sd	p-value	p-value	p-value
Click ABR [dB]	32 ± 6	38 ± 11	28 ± 4	32 ± 7	0.267	0.200	0.091
Threshold at 6 kHz [dB]	38 ± 5	46 ± 20	38 ± 5	38 ± 6	0.159	0.995	0.314
Threshold at 12 kHz [dB]	23 ± 3	28 ± 7	24 ± 4	24 ± 5	0.014	0.577	0.293
Threshold at 18 kHz [dB]	30 ± 10	38 ± 10	29 ± 7	42 ± 25	0.007	0.253	0.006
Threshold at 24 kHz [dB]	58 ± 29	72 ± 30	45 ± 20	62 ± 33	0.284	0.481	0.187
Threshold at 30 kHz [dB]	70 ± 26	89 ± 18	64 ± 25	76 ± 26	0.059	0.318	0.047
Body weight ABR [g]	23.8 ± 2.2	23.8 ± 3.3	32.1 ± 3.2	30 ± 2.1	0.956	0.128	0.569

Suppl. table S14. modified SHIRPA							
	Female		Male		Both		
	WT	KO	WT	KO	WT	KO	p value [1]
	n=15	n=15	n=15	n=15	50%	50%	
	Absolute		Absolute		Percent		
Body Position							NA
Inactive	0	0	0	0	0%	0%	
Active	15	15	14	15	100%	100%	
Excessive Activity	0	0	0	0	0%	0%	
Tremor							NA
Absent	15	15	14	15	100%	100%	
Present	0	0	0	0	0%	0%	
Palpebral Closure							NA
Eyes open	15	15	14	15	100%	100%	
Eyes closed	0	0	0	0	0%	0%	
Lacrimation							NA
Absent	15	15	14	15	100%	100%	
Present	0	0	0	0	0%	0%	
Defecation							0.77872
Present	10	9	10	13	69%	73.30%	
Absent	5	6	4	2	31%	26.70%	
Transfer Arousal							0.42198
Extended freeze	0	0	0	0	0%	0%	
Brief freeze	11	10	6	11	58.60%	70%	
Immediate movement	4	5	8	4	41.40%	30%	
Gait							NA
Fluid movement	15	15	14	15	100%	100%	
Lack Fluidity	0	0	0	0	0%	0%	
Pelvic Elevation							NA
less 5	0	0	0	0	0%	0%	
more 5	15	15	14	15	100%	100%	

Tail Elevation							NA
Dragging	0	0	0	0	0%	0%	
Horizontally extension	15	15	14	15	100%	100%	
Elevated/Straub tail	0	0	0	0	0%	0%	
Startle Response							NA
None	0	0	0	0	0%	0%	
Normal	15	15	14	15	100%	100%	
Jumping	0	0	0	0	0%	0%	
Touch Escape							NA
No response	0	0	0	0	0%	0%	
Response to touch	15	15	14	15	100%	100%	
Flees prior to touch	0	0	0	0	0%	0%	
Positional Passivity							NA
Struggles when held by the tail	15	15	14	15	100%	100%	
Struggles when held by the neck	0	0	0	0	0%	0%	
Struggles when laid supine	0	0	0	0	0%	0%	
No struggle	0	0	0	0	0%	0%	
Trunk Curl							NA
Absent	15	15	14	15	100%	100%	
Present	0	0	0	0	0%	0%	
Limb Grasping							NA
Absent	15	15	14	15	100%	100%	
Present	0	0	0	0	0%	0%	
Pinna Reflex							NA
Present	15	15	14	15	100%	100%	
Absent	0	0	0	0	0%	0%	
Corneal Reflex							NA
Present	15	15	14	15	100%	100%	
Absent	0	0	0	0	0%	0%	
Urination							0.14317

Present	3	5	2	6	17.20%	36.70%	
Absent	12	10	12	9	82.80%	63.30%	
Contact Righting Reflex							NA
Present	15	15	14	15	100%	100%	
Absent	0	0	0	0	0%	0%	
Evidence Of Biting							NA
None	15	15	14	15	100%	100%	
Biting	0	0	0	0	0%	0%	
Vocalisation							NA
No	15	15	14	15	100%	100%	
Yes	0	0	0	0	0%	0%	
	Female		**Male**		**Linear model**		
	WT	KO	WT	KO	genotype	sex	genotype:sex
	mean ± sd	mean ± sd	mean ± sd	mean ± sd	p-value	p-value	p-value
weight [g]	18.5 ± 1.57	18.54 ± 1.57	25.32 ± 2.79	23.58 ± 1.59	0.097	<0.001	0.082
Locomotor activity	26.13 ± 4.31	25 ± 6.52	27 ± 4.37	26.87 ± 5	0.638	0.312	0.71
[1]Fisher's Exact test							

Suppl. table S15. Electrocardiography							
	female		male		female	male	overall
	WT	KO	WT	KO	Wilcoxon rank-sum test		
	n=15	n=15	n=14	n=13			
	mean ± sd	mean ± sd	mean ± sd	mean ± sd	p-value	p-value	p-value
Heart Rate [bpm]	762 ± 26	759 ± 28	786 ± 42	776 ± 32	0.783	0.302	0.385
Heart Rate Variability [bpm]	12.3 ± 9.3	8.1 ± 8.9	15.5 ± 35.3	32.2 ± 45.7	0.091	0.308	0.626
RR [ms]	78.9 ± 2.8	79.2 ± 2.9	76.9 ± 5	77.9 ± 4	0.798	0.274	0.368
PQ [ms]	19.3 ± 3.1	17 ± 2.9	18.1 ± 3.7	17.7 ± 3.6	0.066	0.84	0.162
PR [ms]	25.3 ± 3.3	23.4 ± 3.2	24.5 ± 3.4	23.8 ± 3.5	0.060	0.694	0.113
QRS [ms]	9.6 ± 0.6	9.9 ± 0.7	10 ± 0.6	9.7 ± 0.9	0.328	0.509	0.73
QT [ms]	37.2 ± 2.8	38.7 ± 2.6	38.7 ± 3.5	38.2 ± 2.8	0.262	0.685	0.604
ST [ms]	28.2 ± 2.5	29.3 ± 2.2	29.2 ± 3.5	29 ± 2.5	0.221	0.952	0.444
QTc [ms]	41.9 ± 2.9	43.5 ± 2.5	44.2 ± 3.3	43.4 ± 3.5	0.184	0.607	0.649
QT dispersion [ms]	18.3 ± 3.3	17.3 ± 2.7	19 ± 12.4	19.6 ± 12.2	0.441	0.558	0.984
QTc dispersion [ms]	20.3 ± 3.4	19.3 ± 2.8	21.7 ± 14.2	23.1 ± 14.1	0.506	0.574	0.909
mean SR amplitude [mV]	0.6 ± 0.71	0.45 ± 0.46	0.6 ± 0.46	0.57 ± 0.34	0.783	0.971	0.724
mean R amplitude [mV]	0.39 ± 0.47	0.32 ± 0.33	0.36 ± 0.29	0.37 ± 0.23	0.830	0.821	0.991

Suppl. table S16. clinical chemistry (fasting values)							
	female		male		Linear model		
	WT	KO	WT	KO	genotype	sex	genotype:sex
	n=15	n=15	n=14	n=15			
	mean ± sd	mean ± sd	mean ± sd	mean ± sd	p-value	p-value	p-value
fasting Glucose [mg/dl]	154.59 ± 30.81[a]	147.93 ± 21.62[a]	146.67 ± 19.10	129.37 ± 20.54	0.081	0.054	0.433
fasting Cholesterol [mmol/l]	2.319 ± 0.212[a]	2.216 ± 0.316[a]	2.687 ± 0.361	2.614 ± 0.308	0.332	< 0.001	0.861
fasting HDL-cholesterol [mmol/l]	1.699 ± 0.147[a]	1.638 ± 0.276[a]	2.012 ± 0.228	1.986 ± 0.235	0.512	< 0.001	0.789
fasting non-HDL Cholesterol [mmol/l]	0.621 ± 0.092[a]	0.578 ± 0.06[a]	0.675 ± 0.156	0.628 ± 0.109	0.187	0.128	0.958
fasting Triglycerides [mmol/l]	0.633 ± 0.164[a]	0.78 ± 0.284[a]	1.293 ± 0.567	1.514 ± 0.745	0.242	< 0.001	0.813
fasting NEFA [mmol/l]	1.15 ± 0.3[a]	1.22 ± 0.32[a]	0.99 ± 0.18	0.98 ± 0.18	0.709	0.007	0.564
fasting Glycerol [mmol/l]	0.174 ± 0.032[a]	0.169 ± 0.029[a]	0.157 ± 0.022	0.168 ± 0.028	0.726	0.276	0.355
[a]Number not based on the full number of animals (missing values)							

Suppl. table S17. Hematology							
	female		male		Linear model		
	WT	KO	WT	KO	genotype	sex	genotype:sex
	n=15	n=15	n=14	n=14			
	mean ± sd	mean ± sd	mean ± sd	mean ± sd	p-value	p-value	p-value
RBC [10^6/mm^3]	10.99 ± 0.49	10.84 ± 0.58	11.03 ± 0.82	11.33 ± 0.74	0.683	0.139	0.201
HGB [g/dl]	16.85 ± 0.93	16.59 ± 0.99	16.89 ± 1.1	16.96 ± 0.92	0.727	0.439	0.516
HCT [percent]	54.02 ± 2.78	53.31 ± 2.46	55.09 ± 3.74	55.98 ± 2.6	0.911	0.018	0.303
MCV [fl]	49.27 ± 1.22	49.2 ± 1.61	49.93 ± 1.33	49.57 ± 1.87	0.599	0.203	0.719
MCH [pg]	15.33 ± 0.43	15.31 ± 0.52	15.32 ± 0.44	14.99 ± 0.51	0.161	0.180	0.212
MCHC [g/dl]	31.19 ± 1.03	31.12 ± 0.83	30.67 ± 0.69	30.31 ± 0.65	0.320	0.003	0.492
RDW [percent]	14.67 ± 0.53	14.62 ± 0.77	16.19 ± 1.35	15.27 ± 1.56	0.108	0.001	0.146
WBC [10^3/mm^3]	6.74 ± 2.44	6.13 ± 1.5	7.75 ± 2.43	8.99 ± 2.7	0.605	0.002	0.131
PLT [10^3/mm^3]	992.33 ± 227.86	980.27 ± 205.42	1052.5 ± 124.98	1008.43 ± 170.73	0.571	0.374	0.747
MPV [fl]	6.06 ± 0.11	6.03 ± 0.12	5.95 ± 0.19	5.86 ± 0.12	0.097	< 0.001	0.354

Suppl. table S18. Body composition (MRI, 12 weeks)								
	female		male		Linear model			
	WT	KO	WT	KO	sex	genotype	body mass	sex:genotype
	n=15	n=15	n=14	n=15				
	mean ± sd	mean ± sd	mean ± sd	mean ± sd	p-value	p-value	p-value	p-value
Body mass NMR [g]	20.5 ± 1.7	20.4 ± 2	27.9 ± 3.4	25.5 ± 2.4	< 0.001	0.051	NA	0.064
Fat mass NMR [g]	4.4 ± 0.6	4.4 ± 0.5	5.8 ± 1	5.3 ± 0.9	0.003	0.538	< 0.001	0.244
Lean mass NMR [g]	12.6 ± 0.9	12.7 ± 1.1	17.8 ± 2	16.3 ± 1.6	< 0.001	0.962	< 0.001	0.25

Suppl. table S19. Food efficiency								
	female		male		Linear model			
	WT	KO	WT	KO	sex	genotype	*body mass	sex:genotype
	n=15	n=15	n=9	n=10			** food intake	
	mean ± sd	mean ± sd	mean ± sd	mean ± sd	p-value	p-value	p-value	p-value
Body mass [g]	23.3 ± 1.5	22.3 ± 1.7	31.6 ± 2.9	30.9 ± 4.0	<0.001	0.244	n/a	0.833
Food uptake [g/d]	4.1 ± 0.4	3.9 ± 0.4	4.1 ± 0.4	3.8 ± 0.6	0.007	0.286	*0.002	0.712
Egested dried feces [g/d]	0.89 ± 0.10	0.84 ± 0.10	0.94 ± 0.11	0.85 ± 0.13	0.555	0.976	**<0.001	0.388
Energy content dried feces [kJ/g]	15.13 ± 0.10	15.18 ± 0.10	15.31 ± 0.11	15.31 ± 0.17	<0.001	0.491	n/a	0.417
Energy uptake [kJ/d]	69.54 ± 7.03	65.39 ± 7.03	69.55 ± 7.10	64.33 ± 9.59	0.007	0.286	*0.002	0.712
Assimilated Energy [kJ/d]	54.94 ± 6.00	51.55 ± 5.77	54.08 ± 5.42	50.35 ± 7.61	0.005	0.283	*0.002	0.835
Assimilation efficiency [%]	78.96 ± 1.76	78.80 ± 1.35	77.78 ± 0.62	78.27 ± 1.31	0.041	0.681	n/a	0.437

Suppl. table S20. Grip Strength							
	female		male		Linear model		
	WT	KO	WT	KO	genotype	sex	genotype:sex
	n=15	n=15	n=14	n=15			
	mean ± sd	mean ± sd	mean ± sd	mean ± sd	p-value	p-value	p-value
Force 2 paws (mean)	87.41 ± 6.5	83.71 ± 10.72	108.6 ± 8.57	109.95 ± 8.18	0.980	<0.001	0.090
Force 4 paws (mean)	173.78 ± 10.76	171.59 ± 11.28	206.34 ± 11.82	208.07 ± 7.22	0.770	<0.001	0.270

Suppl. table S21. Hot plate test									
	female		male		females	males			
	WT	KO	WT	KO	genotype		genotype	sex	sex:genotype
	N=15	N=15	N=14	N=15	adj. p-value	adj. p-value	p-value	p-value	p-value
	mean ± sd	mean ± sd	mean ± sd	mean ± sd	pairwise (Tukey)		ANOVA		
Body weight [g]	20.74 ± 1.56	20.89 ± 1.75	28.58 ± 3.83	26.15 ± 2.22	0.998	0.051	0.089	< 0.001	0.051
First response time	17.01 ± 5.35	16.19 ± 4.28	14.12 ± 2.96	13.62 ± 2.86	0.942	0.987	0.526	0.011	0.877
Second response time	21.53 ± 4.75	21.07 ± 6.25	20.91 ± 4.51	17.71 ± 2.64	0.993	0.273	0.147	0.101	0.271

Suppl. table S22. DNA primer		
name	**sequence**	**direction**
genotyping "1", 5' of floxed Fgfbp1	CCA ACA GGT GGT CAT TGG TAC CC	fw
genotyping "2", Fgfbp1 ORF	CAA GTG GTC CTG CGT ACT CTC	rev
genotyping "3", 3' UTR of Fgfbp1	GGT GTC ACA GGT GAT TAG AGA GAA GGC	fw
genotyping "4", neomycin	AGC GCA TCG CCT TCT ATC GCC TTC	fw
genotyping "5", GFP	CCT CGC CCT TGC TCA CCA T	rev
genotyping "6", 3' of FRT site	GCC CAC CTC CTG TTA CAG CTG	rev
genotyping "7", 3' outside target region	GTG CAC AGC ATG TCT GAG TAT CAC	rev
Fgfbp1	CCA GTA CAC CTG GAT CTG CAC ACT C	fw
Fgfbp1	TGA GAA CGC CTG AGT AGC CA	rev
GFP	CCG ACA ACC ACT ACC TGA GCA C	fw
GFP	CTT GTA CAG CTC GTC CAT GCC G	rev
FGFR1-B-ISH	CAT TCG GGA ATT AAT AGC TCG GAT GCG	fw
FGFR1-B-ISH	CTT TTG CCA CAG GTC TGG TGA CAG	rev
FGFR1-C-ISH	ACT GCT GGA GTT AAT ACC ACC GAC AAG	fw
FGFR1-C-ISH	CTT CCA GAA CGG TCA ACC ATG CAG	rev
Fgfr1-IIIb	CAACTTGCCGTATGTCCAGATC	fw
Fgfr1-IIIb	CTCCGCATCCGAGCTATTAA	rev
Fgfr1-IIIc	GCCAGACAACTTGCCGTATG	fw
Fgfr1-IIIc	ATTTCCTTGTCGGTGGTATTAACTC	rev
Fgfr2-IIIb	GGGCTGCCCTACCTCAAG	fw

Fgfr2-IIIb	CTTCTGCATTGGAGCTATTTATCC	rev
Fgfr2-IIIc	CCCGGCCCTCCTTCA	fw
Fgfr2-IIIc	GTTGGGAGATTTGGTATTTGGTT	rev
Fgfr3-IIIb	GCACGCCCTACGTCACTGTA	fw
Fgfr3-IIIb	GCGTCTGCCTCCACA TTCT	rev
Fgfr3-IIIc	ACGGCACGCCCTACGT	fw
Fgfr3-IIIc	CTCCTTGTCGGTGGTGTTAGC	rev
Fgfr4	CGCCAGCCTGTCACTATACAAA	fw
Fgfr4	CCAGAGGACCTCGACTCCAA	rev
Il17a	TTT TCA GCA AGG AAT GTG GA	fw
Il17a	TTC ATT GTG GAG GGC AGA C	rev
Il23	CAC CTC CCT ACT AGG ACT CAG C	fw
Il23	TGG GCA TCT GTT GGG TCT	rev
Il6	TAGTCCTTCCTACCCCAATTTCC	fw
Il6	TTGGTCCTTAGCCACTCCTTC	rev
Klk6	TGTGCTTGGTTCTTGCTAAATCA	fw
Klk6	AGTGACCTGAGGTGTAGAGGG	rev
Krt16	GGTGGCCTCTAACAGTGATCT	fw
Krt16	TGCATACAGTATCTGCCTTTGG	rev
Krt27	TATGGGCGGTGCTTCTTGTG	fw
Krt27	TCCAGTGCTTGCACGTTCTC	rev
S100a8	AAATCACCATGCCCTCTACAAG	fw
S100a8	CCCACTTTTATCACCATCGCAA	rev
Sprr2d	GAGAATCCAGCACTATGTCTTACC	fw
Sprr2d	GACAAGGCTCAGGACACTTTAG	rev